VST FAKULTÄT FÜR VERFAHRENS- UND SYSTEMTECHNIK

Lattice Boltzmann modeling of crystal growth in aqueous and gaseous media

Dissertation
for the award of the degree

Doktoringenieurin (Dr.-Ing.)

by M.Sc. Qianyan Tan
born 21.09.1991 in Jiangsu, China
accepted by the Faculty for Process and Systems Engineering
of the Otto-von-Guericke-University of Magdeburg

President:	Prof. Dr. rer. nat. Heike Lorenz
Reviewers:	Prof. Dr.-Ing. Dominique Thévenin
	Prof. Dr.-Ing. Andreas Seidel-Morgenstern
	Prof. Dr. Fathollah Varnik

submitted on: 04.10.2024
Graduation colloquium on: 10.09.2024

Abstract

Phase-field model is a powerful tool for simulating the evolution of crystal interfaces during solidification and crystallization. Its strength lies in its ability to bypass the explicit tracking of macroscopically sharp phase boundaries, rendering it especially suitable for addressing time-dependent free-boundary problems in three dimensions and complex geometries. Meanwhile, lattice Boltzmann method (LBM) has demonstrated proficiency in simulating fluid dynamics and has been successfully employed, with classical solid-phase solvers, for crystal growth simulations.

This thesis presents the development of lattice Boltzmann (LB) solver (ALBORZ) for the phase-field (PF) model, divided into eight main chapters. The first part highlight the advantages of the phase-field lattice Boltzmann (PF-LB) method for simulating the pure crystal growth, with a comprehensive overview of the dissertation's plan provided in the concluding part of this chapter. Subsequent chapters delve into the foundation of phase field models, the specifics of the single relaxation time (SRT) with the Bhatnagar, Gross, Krook (BGK) operator, and the application of LB schemes for the PF equation. Validations in 2D are detailed in Chapter 4, covering the benchmark for anisotropy advection-diffusion equation (ADE), the directional derivative method and the influence of physical parameters on crystal rate and morphologies.

Chapter 5 presents 3D simulations of crystals with various anisotropy functions, including multi-crystal simulations incorporating hydrodynamic effects, and the application of a baffle around the inlet to showcase its influence on crystal morphologies.

Shifting focus to modeling ice crystal growth in Chapter 6, the LBM is employed to tackle the intricate task of simulating snowflake crystals under diverse ambient conditions. The validated solver from Chapter 4 is modified to model snowflake growth, with resulting habits compared to numerical and experimental references in the literature.

In chapter 7, a numerical tool based on LB simulations is introduced to model the crystallization dynamics of (S)-mandelic acid and explore thermal effects during crystallization. The solver is validated against experimental data and used for parametric studies on critical factors like supersaturation and seed size's impact on growth rate. The possible impact of temperature differences during crystal growth is investigated based on a hybrid solver combining the LBM with finite difference (FD) method, extending to explore the impact of forced convection on crystal habits while considering temperature differences.

This comprehensive dissertation presents a multifaceted exploration, offering a robust LB solution for the PF model and its application to diverse crystallization phenomena, from pure crystal growth to the complexities of ice crystal and (S)-mandelic acid crystallization.

Keywords: Lattice Boltzmann method, Phase-field model, Crystallization, Hydrodynamic effect, Thermal effect.

Zusammenfassung

Das Phasenfeldmodell ist ein leistungsstarkes Werkzeug zur Simulation der Evolution von Kristallgrenzflächen während der Erstarrung und Kristallisation. Seine Stärke liegt in der Möglichkeit, die explizite Verfolgung makroskopisch scharfer Phasengrenzen zu umgehen, was es besonders geeignet macht, zeitabhängige Freigrenzprobleme in drei Dimensionen und komplexen Geometrien anzugehen. Gleichzeitig hat sich die Gitter-Boltzmann-Methode (LBM) profiliert in der Simulation von Fluiddynamik und wurde erfolgreich zusammen mit klassischen Festphasensolvern für die Simulation des Kristallwachstums eingesetzt.

Diese Schrift präsentiert die Entwicklung eines LB-Lösers (ALBORZ) für das Phasenfeld (PF)-Modell, aufgeteilt in acht Hauptkapitel. Der erste Teil hebt die Vorteile der Phasenfeld-Gitter-Boltzmann (PF-LB)-Methode für die Simulation des reinen Kristall-wachstums hervor, mit einem umfassenden Überblick über den Plan der Dissertation, der im abschließenden Teil dieses Kapitels gegeben wird. Die nachfolgenden Kapitel gehen auf die Grundlagen der Phasenfeldmodelle, die Besonderheiten der Einzelrelaxationszeit (SRT)-Methode mit dem Bhatnagar-Gross-Krook (BGK)-Operator und die Anwendung von Gitter-Boltzmann-Schemata für die Phasenfeldgleichung ein. Validierungen in 2D werden in Kapitel 4 detailliert behandelt, wobei der Benchmark für die Anisotropie-Advektions-Diffusionsgleichung (ADE), die Richtungsableitungsmethode und der Einfluss physikalischer Parameter auf die Kristallrate und -morphologien abgedeckt werden.

Kapitel 5 präsentiert 3D-Simulationen von Kristallen mit verschiedenen Anisotropie-funktionen, einschließlich Mehrkristallsimulationen, die hydrodynamische Effekte berücksichtigen, sowie die Anwendung eines Baffles um den Einlass, um dessen Einfluss auf Kristallmorphologien zu zeigen.

Mit der Verlagerung des Fokus auf die Modellierung des Eiswachstums in Kapitel 6 wird die Gitter-Boltzmann-Methode verwendet, um die komplexe Aufgabe der Simulation von Schneekristallen unter verschiedenen Umgebungsbedingungen anzugehen. Der validierte Solver aus Kapitel 4 wird modifiziert, um das Schneekristallwachstum zu modellieren, wobei die resultierenden Formen mit numerischen und experimentellen Referenzen in der Literatur verglichen werden.

Im Kapitel 7 wird ein numerisches Werkzeug auf Basis von Gitter-Boltzmann-Simulationen vorgestellt, um die Kristallisationsdynamik von (S)-Mandelsäure zu modellieren und thermische Effekte während der Kristallisation zu untersuchen. Der Solver wird anhand experimenteller Daten validiert und für parametrische Studien zu kritischen Faktoren wie Übersättigung und Auswirkungen der Korngröße auf die Wachstumsrate verwendet. Der mögliche Einfluss von Temperaturunterschieden während des Kristallwachstums wird mithilfe eines Hybridlösers, der die Gitter-Boltzmann-Methode mit Finite-Differenzen-Methoden kombiniert, untersucht, wobei auch der Einfluss erzwungener Konvektion auf die Kristallformen unter Berücksichtigung von Temperaturunterschieden erforscht wird.

Diese umfassende Dissertation präsentiert eine facettenreiche Exploration und bietet eine robuste Gitter-Boltzmann-Lösung für das Phasenfeldmodell und seine Anwendung auf verschiedene Kristallisationsphänomene, angefangen beim reinen Kristallwachstum bis hin zu den Komplexitäten des Eis- und (S)-Mandelsäurekristallwachstums.
Schlagwörter: Lattice-Boltzmann-Methode, Phasenfeldmodell, Kristallisation, hydrodynamischer Effekt, thermischer Effekt.

Contents

List of Figures

List of Tables

Nomenclature

Roman Symbols

c_∞	saturated concentration at the initial temperature	[mol/m^3]
D	solute diffusion coefficient	[m^2/s]
d_0	capillary length	[m]
F_d	interaction with the solid phase	[N]
f_i	distribution function in direction i	[-]
L	latent heat	[J/kg]
T_m	melting temperature of the solid	[K]
U	dimensionless supersaturation	[-]
u	fluid velocity	[m/s]
W_0	initial interface thickness	[m]

Greek Symbols

α	index of the coordinates x	[-]
β	index of the coordinates y	[-]
γ	index of the coordinates z	[-]
γ_0	average interface tension over all orientations	[N/m^2]
ε_s	strength of anisotropy	[-]
κ	thermal diffusivity	[m^2/s]

λ	coupling coefficient	[-]
μ_k	interface mobility coefficient	[-]
ν_f	fluid kinematic viscosity	[m^2/s]
ϕ	order parameter	[-]
ρ_f	density of the fluid	[kg/m^3]
τ_0	relaxation time	[s]
Θ	angle between xy-plane and the z-axis	[rad]
θ	dimensionless undercooling	[-]
φ	angle between x-axis and y-axis	[rad]

Abbreviations

A-C	Allen-Cahn
ADE	Advection-diffusion equation
BGK	Bhatnagar, Gross, Krook
C-H	Cahn-Hilliard
EDF	Equilibrium distribution function
FD	Finite difference
FHP	Frisch, d'Humières, Hasslacher
LB	Lattice Boltzmann
LBE	Lattice Boltzmann equation
LBM	Lattice Boltzmann method
LGA	Lattice gas automata
LHS	Left-hand side
MRT	Multi-relaxation Time

NS	Navier-Stokes
PDE	Partial differential equation
PF	Phase-field
PF-LB	Phase-field lattice Boltzmann
RHS	Right-hand side
SRT	Single relaxation time

Chapter 1

Introduction

Contents

1.1 Motivation and objective

In the intricate realm of materials science, the crystal growth process stands as a pivotal phenomenon with far-reaching implications for diverse applications, from advanced technologies to pharmaceuticals. This thesis embarks on an immersive exploration, delving into the dynamic intricacies of crystal growth within both aqueous and gaseous media through the utilization of the PF model. By employing the LBM, this research endeavors to investigate the growth habits that emerge within the concurrent interplay of fluid dynamics, mass transport, and thermodynamics, which collectively govern the processes of crystal nucleation and growth.

The LBM, renowned for its ease of implementation, straightforward parallelization, its computational efficacy, ability to handle complex geometries and versatile applicability in complex fluid dynamics, emerges as a potent tool for studying the growth habits of crystal growth. Within the aqueous/gaseous media, the investigation employs a PF model integrated into the modified LB framework. This integration allows for the systematic comprehension of the intricate dynamics dictating crystal growth within a two-phase flow field regime.

The PF theory, employed to model solidification and crystallization processes, considers the interface between the solid and liquid phases as diffuse. The order parameter ϕ within different phases remains nearly constant within their respective domains, varying smoothly at the interface. The PF models facilitate the introduction of interfacial anisotropy, enabling accurate simulations of dendritic growth. In these models, interfacial energy and mobility are decomposed into constant values multiplied by a locally dependent function on the unit normal vector of the interface, denoted as the anisotropy function $a_s(\mathbf{n})$. This function influences the characteristic shape of crystals and plays a pivotal role in the PF equation. To profit from the advantages of the LBM, such as ease of implementation and straightforward parallelization, Younsi and Cartalade [1] proposed a comprehensive implementation of the PF model within the LB framework. Their modifications to the standard LB equations and equilibrium distribution functions introduced anisotropic surface tension and growth rate effects, successfully simulating anisotropic and dendritic growth. Despite their applicability to generic systems, these models have been seldom utilized for simulating realistic systems.

The objective of this investigation is to investigate fundamental parameters regarding the crystal nucleation kinetics, growth rates, and the influence of fluid flow on the obtained crystal morphology. This comprehensive research delves into two distinct crystal categories: snowflakes and (S)-mandelic acid. Each category is computed within the realm of two dimensions, facilitating a profound comprehension of the intricate interplay between fluid dynamics and crystal growth within these specific systems.

1.2 Thesis outline

This thesis describes some contributions in the simulation of crystal growth employing the LBM within both aqueous and gaseous media. The entirety of these investigations is conducted utilizing an in-house LB solver, denominated ALBORZ, developed at the Laboratory of Fluid Dynamics and Technical Flows (LSS) at the University of Magdeburg. The computational endeavors are characterized by a high level of efficiency, both in terms of CPU time and memory consumption, demonstrating the adept capabilities of ALBORZ. This code exhibits versatility by accommodating simulations of both two-dimensional (2D) and three-dimensional (3D) configurations on a parallel computing architecture.

Following this introductory chapter, the thesis unfolds with a comprehensive exposition detailing the PF model of crystal growth utilizing the LBM.

Chapter 2 (PF model: Mathematical description) contains an introduction into the PF model. It encompasses the historical background of the model, its advantages and disadvantages and governing equations. A comprehensive depiction of crystal growth necessitates the integration of the growth model with a fluid flow solver.

Chapter 3 (LBM) serves as a short introduction to the theoretical underpinnings of the LBM. The LBM is developed for simulations with the PF model, introducing a new equilibrium distribution function for solving the PF equation with a modified method for ADE.

Chapter 4 (Validations in 2D) is dedicated to benchmarking studies validating the accuracy and reliability of the computational simulations employed in the thesis. The analysis encompasses the validation of the anisotropic ADE, anisotropy strength ε_s, isotropic order enhancement, validation of the tip velocity of a single crystal, exploration of the interface interaction between solid and liquid phases, and validation of flow/solid coupling, revealing the hydrodynamic effects on the growth rate of tips.

Chapter 5 (Crystal simulations in 3D) presents simulation results of crystal growth with different anisotropy functions in 3D, examining various shapes of 3D crystals, the impact of undercooling and Reynolds effects, simultaneous growth of multiple crystals, and ventilation effects on the crystal in 3D. We introduced a baffle to examine its impact on crystal habits.

Chapter 6 (Modeling ice crystal growth) covers the simulation of the snowflakes, introducing a LBM model for the simulation of ice in 2D with a modified phase field model to capture the different crystal habits in the plate growth regime.

Chapter 7 (Modeling Mandelic acid crystallization) delves into the crystallization dynamics of (S)-mandelic acid, validating against experimental data, analyzing critical factors like supersaturation and seed size's impact on growth rate, and studying the impact of temperature differences during crystal growth based on a hybrid solver combining the LBM with FD method. Also, the im-

pact of forced convection on the crystal habits is investigated while taking into account temperature differences.

Chapter 8 (Conclusions and Outlook) serves as the conclusion, offering a comprehensive summary and discussion of the research topics and findings. Future topics on the simulation of crystal growth are also considered.

Chapter 2

Phase-field Model : Mathematical description

Contents

2.1 Introduction

Crystal growth simulation [1,2] presents a challenging endeavor, given its intricate nature involving the phase transition from solid to liquid states, which is demarcated by a well-defined interface. In recent years, the PF method has emerged as one of the most prominent approaches for modeling interfacial pattern formation phenomena during solidification and crystallization. In order to follow the interface position, several modeling methods exist in the literature, mainly divided into two classes: the separation between each phase can be considered as a sharp interface or a diffuse one. In this work, we present an introduction of PF theory, a diffuse interface method that is consistent with the thermodynamics of the system. In the PF approach, nonlinear partial differential equation (PDE) can be obtained from the principles of out-of-equilibrium thermodynamics. Therefore, they also naturally incorporate thermodynamic boundary conditions at the interfaces, such as the Gibbs–Thomson condition and the equation of mass balance. The equation describes the evolution of an order parameter ϕ which varies smoothly from one value (-1) in the liquid to another value (+1) in the solid across a spatially diffuse interface region of thickness W in a hyperbolic tangent (see Fig. 2.1). The widely recognized appeal of this approach is to avoid the explicit tracking of macroscopically sharp phase boundaries [3–5]. This makes it more suitable than conventional front-tracking methods [4, 5] to simulate the time-dependent free-boundary problem (TDFBP) in three dimensions (3D) or when complex geometries are involved.

In PF models, the interfacial energy and the mobility are decomposed into a product of a constant value with a function depending locally on the normal vector of the interface. This function is responsible for the characteristic shape of the crystals, it is involved in the PF equation. Let us remind that in the sharp interface formulation, the anisotropy function appears in the Gibbs–Thomson condition which gives the interface temperature as a function of the melting temperature, corrected by the curvature and the kinetic mobility of the interface. In the literature, for most of 3D crystal growth simulations, the anisotropy function is chosen such as the branches of crystal grow along the main axes of the coordinate system, i.e. in the x-, y-and z-directions. This particular direction of growth is called the direction in 3D. Thus, the crystal presents generally a dendritic shape with six tips, two of them being directed along the x-axis, two other directed along the y-axis and two last ones directed along the z-axis.

The thermodynamic behavior of the binary fluid system is typically described by a free-energy function associated with the order parameter, i.e., Cahn-Hilliard (C-H) equation [6] and Allen-Cahn (A-C) equations [7]. The C-H equation incorporates the chemical potential in the diffusion term, which includes a fourth-order spatial derivative. However, the higher-order derivative in the diffusion term can numerically pose challenges, may lead to a reduction in both locality and accuracy [8]. As an alternative, the A-C equation only requires a second-order algorithm for the

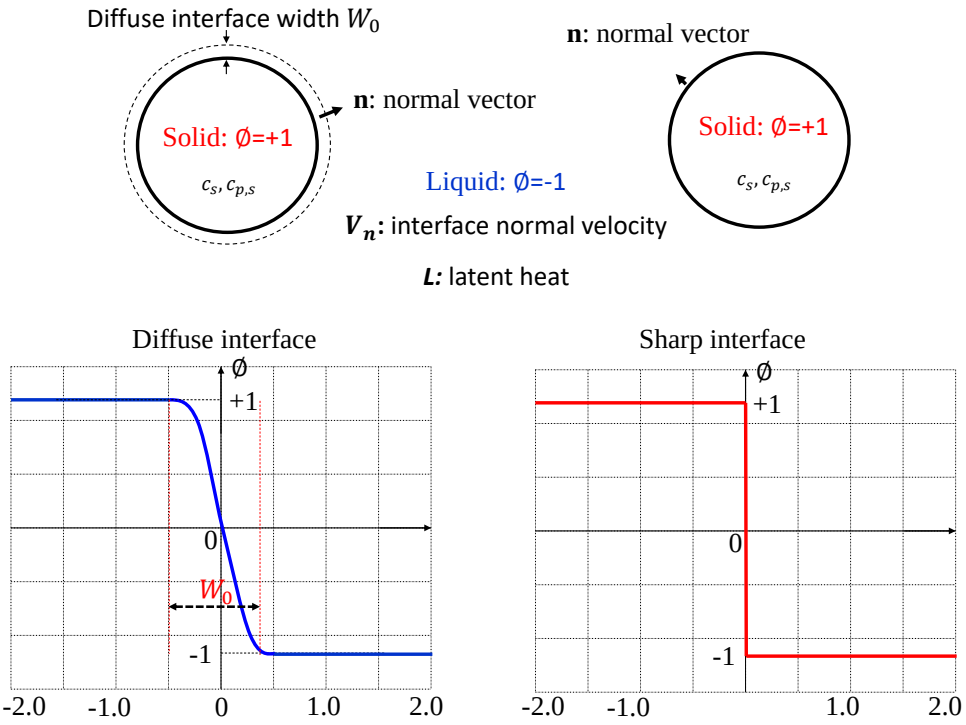

Figure 2.1: Description for phase field interface.

discretization of the diffusion term. Based on the dynamics of A-C equation, Karma and Rappel [9, 10] investigated a computationally efficient PF method for quantitive modeling of dendritic crystal growth with the limit of thin interface thickness. These thin interface analyses assume that the interfacial region is small compared to the scale of the microstructural pattern but much larger than the capillary length. It is possible to keep good accuracy at moderate computational cost. To further study the Karma-Rappel model, Ramirez et al. [11] employed the PF method for binary alloy solidification with coupled heat and solute diffusion. Cartalade and his group [1,2,12] implemented a phase field model for solification of a dilute binary mixture by using the lattice Boltzmann method, which encompassed comprehensive investigations into the effects of anisotropy function and convection on crystal shapes. Cartalade's research laid the groundwork for the subsequent investigation, in which Demange et al. [13–15] developed a new anisotropy function that effectively captures the distinctive 6-fold horizontal and 2-fold vertical symmetries observed in snowflakes. This application enhanced our understanding of snowflake characteristics, enabling more accurate modeling and analysis of snowflake behavior and formation.

It is known that fluid flow during crystallization significantly influences the crystal structures. By employing typical values for the local flow velocity, material properties and process parame-

ters, one can anticipate that the interdendritic flow is dominated by viscous forces. The mechanism through which this flow modifies the growth pattern involves the transfer of solute from the leading edge to the trailing edge of the dendrite. In order to study the hydrodynamic effect on the crystal growth, Beckermann et al. [16] developed a PF model that couples with the Navier-Stokes (NS) equation. In this model, the phase field equation remains unchanged, while an advective term is introduced to the heat/species equation, and a force term is incorporated into the momentum equation. The phase field ϕ is not directly featured in the heat equation and Navier-Stokes equations; instead, the advective terms within the solid region are canceled by using a new function $(1-\phi)/2$ which is equal to 0 in the solid and +1 in the liquid. Additionally, other investigations exploring convective effects with different numerical methods have been conducted in detail by [12, 17, 18].

This Chapter aims to describe the mathematical model for solidifying a single substance under supersaturated conditions induced by undercooling, as will be addressed in Chapter 3. Firstly, the sharp-interface model of crystallization is reviewed in Sec. 2.2. Then, we introduce the generality of the PF model in Sec. 2.3. The anisotropy function is detailed in Sec. 2.3. Finally, Sec. 2.5 is devoted to the coupling with the NS equation for the flow field and Sec. 2.6 gives some summarized remarks. In this chapter, we will provide a detailed introduction to all terms in the model equation and provide the physical meaning of each parameter.

2.2 Sharp-interface model

Phase-field formulations introduce novel parameters that must be linked to physically measurable properties. This linkage is often achieved through a "sharp-interface" analysis [11], which explores the asymptotic behavior of the model equations as the interface width approaches zero. The model description and its relationship with the "sharp-interface" model can be summarized as follows:

$$\partial_t c = D\nabla^2 c \qquad \text{(liquid)}, \tag{2.1}$$

$$\partial_t T = \kappa\nabla^2 T \qquad \text{(liquid and solid)}, \tag{2.2}$$

$$c_l V_n = -D\partial_n c_l \qquad \text{(mass conservation)}, \tag{2.3}$$

$$LV_n = c_p\kappa(\partial_n T|_s - \partial_n T|_l) \qquad \text{(heat conservation)}, \tag{2.4}$$

$$T_i = T_m - \Gamma\mathcal{K} - V_n/\mu_k \qquad \text{(Gibbs}-\text{Thomson)}, \tag{2.5}$$

This process is driven by heat conduction and solute diffusion, respectively. The first two equations describe solute and heat diffusion according to Fick's and Fourier's laws, incorporating the solute diffusivity D in the liquid and thermal diffusivity κ in both liquid and solid. The diffusivity of solute in the liquid state is significantly lower, usually by two to four orders of magnitude, than thermal diffusivity. As a result, solute diffusion frequently occurs over length scales comparable

to that of the microstructure. The next two equation expresses the mass and heat conservation at the moving boundary (Stefan condition), taking into account the normal velocity V_n of the interface. The latent heat L is released during the crystallization, leading to heat fluxes away from the interface. The specific heat capacity c_p is assumed to be consistent across both phases (symmetric model) and solute transport is limited to the liquid phase (one-sided model). Moreover, we limit our study to the symmetric model characterized by uniform density. The last equation represents the Gibbs-Thomson boundary condition, establishing a connection between the interface temperature and the composition of the pure solvent. $\Gamma_0 = \gamma_0 T_m / L$ is the Gibbs-Thomson constant, with γ_0 the average interface tension over all orientations and T_m the melting temperature of the solid. γ_0 is isotropic to construct the PF model and the related anisotropy tension is introduced in the next section. $\mathcal{K}$ is the interface radius of curvature and μ_k is the interface mobility.

To better establish a connection between the sharp interface and the PF model, the dimensionless variables are defined as following:

$$U = \frac{c - c_\infty}{c_\infty} \tag{2.6}$$

$$\theta = \frac{T - T_m}{L/c_p} \tag{2.7}$$

where c_∞ is the saturated concentration at the initial temperature. U and θ are dimensionless definition of supersaturation and undercooling, respectively. In terms of these variables, the equations 2.1 to 2.5 become:

$$\partial_t U = D\nabla^2 U, \tag{2.8}$$

$$\partial_t \theta = \kappa \nabla^2 \theta, \tag{2.9}$$

$$(1 + U_i) V_n = -D \partial_n U|_l, \tag{2.10}$$

$$V_n = \kappa(\partial_n \theta|_s - \partial_n \theta|_l) \tag{2.11}$$

$$\theta_i = -d(\vartheta)\mathcal{K} - \beta V_n \tag{2.12}$$

where ϑ is the angle between the interface normal and the x axis direction of the coordinate system. The subscript i is used when evaluating θ and U at the interface, specially on the liquid side for U. And the capillary length $d(\vartheta)$ is defined as:

$$d(\vartheta) = \frac{d_0 \left(\gamma(\vartheta) + \gamma''(\vartheta)\right)}{\gamma_0} \tag{2.13}$$

where $\gamma(\vartheta)$ denotes the anisotropy interface tension and $d_0 = \Gamma_0 c_p / L = \gamma_0 T_m c_p / L^2$ is the averaged capillary length. $\beta = c_p / L\mu_k$ is the kinetic coefficient. In principle, β is orientation-dependent too.

However, we consider the case characterized by rapid attachment kinetics, leading to a negligible influence of β. This implies certain constraints on the choice of parameters of the PF model, as detailed in the subsequent section.

2.3 Phase-field model

The objective is to construct a phase-field model that reduces to the above set of sharp interface in a computationally tractable thin interface limit where (i) the width W of the diffuse interface is mesoscopic. W is about one order of magnitude smaller than the radius of curvature of the interface but much larger than the real microscopic width of a solid-liquid interface; (ii) kinetic effects are negligible ($\beta = 0$) as for crystal solidification at small undercooling/supersaturation. We first motivate the PF equations from a thermodynamic viewpoint and then analyze the thin-interface limit of these equations by a direct extension of recent results for the solidification of a single crystal.

The starting point of the model is an expression for the total free energy of the system that can be written in the form [11]:

$$F(\phi,U,\theta) = \int dV \left[\frac{W^2(\mathbf{n})}{2} |\nabla\phi|^2 + f_{dw}(\phi) + (\lambda_1\theta + \lambda_2 U) g(\phi) \right], \tag{2.14}$$

where $W(\mathbf{n})$ is the interface thickness depending on the normal vector $\mathbf{n} = -\frac{\nabla\phi}{|\nabla\phi|}$, pointing from solid to liquid. The function $f_{dw}(\phi)$ is the standard double-well potential,$f_{dw} = -\phi^2/2 + \phi^4/4$, defined in this model such as two minima appear at $\phi = \pm 1$. The coupling with the undercooling θ and supersaturation U are given by the last term $(\lambda_1\theta + \lambda_2 U)g(\phi)$, where λ_1 and λ_2 are the coupling coefficient for undercooling and supersaturation, respectively. $g(\phi) = (15/8)(\phi - 2\phi^3/3 + \phi^5/5)$ is a monotonous interpolation function of the internal energy inside the diffuse zone. The specific form of the coupling term is obtained by performing the difference between the free energy densities of solid and liquid. This term represents the driving force of the solidification process. Once the total free energy of the system $F(\phi,\theta,U)$ is defined, the interface motion equation can be written as:

$$\tau(\mathbf{n})\frac{\partial\phi}{\partial t} = -\frac{\partial F}{\partial\phi} \tag{2.15}$$

where $\tau(\mathbf{n})$ is the function describing the interface dynamics. Eq. (2.15) is the A-C equation that describes the dynamics of the non-conserved variables, where the order parameter ϕ is referred as a function. Our demonstration is based on an analysis of the sharp-interface limit of the PF model which includes spatial variations of θ and U in the interface region. We consider the PF model by

equations:

$$a_s(\mathbf{n})\frac{\partial \phi}{\partial t} = \frac{W_0^2}{\tau_0}\nabla\cdot[a_s(\mathbf{n})^2\nabla\phi] + \frac{W_0^2}{\tau_0}\nabla\cdot\mathscr{N} + \frac{(\phi-\phi^3)-(\lambda_1\theta+\lambda_2 U)(1-\phi^2)^2}{\tau_0}, \tag{2.16}$$

$$\frac{\partial \theta}{\partial t} + \left(\frac{1-\phi}{2}\right)\boldsymbol{u}\cdot\nabla\theta = \kappa\nabla^2\theta + \frac{1}{2}\frac{\partial \phi}{\partial t} \tag{2.17}$$

$$\frac{\partial U}{\partial t} + \left(\frac{1-\phi}{2}\right)\boldsymbol{u}\cdot\nabla U = D\nabla\cdot(q(\phi)\nabla U) - \frac{1}{2}\frac{\partial \phi}{\partial t} \tag{2.18}$$

In Eq. (2.16), the first term of the right-hand side is a diffusive term, the second one is responsible for anisotropic growth where $\mathscr{N}$ is defined by:

$$\mathscr{N}(\boldsymbol{x},t) = |\nabla\phi|^2 a_s(\boldsymbol{n})\left(\frac{\partial a_s(\boldsymbol{n})}{\partial(\partial_x\phi)}, \frac{\partial a_s(\boldsymbol{n})}{\partial(\partial_y\phi)}, \frac{\partial a_s(\boldsymbol{n})}{\partial(\partial_z\phi)}\right)^T, \tag{2.19}$$

The last one is the derivative of the double-well potential with respect to ϕ and the derivative with respect to ϕ of the coupling term with undercooling and supersaturation. Anisotropy in the surface energy and in the kinetics is incorporated as in [19,20] via the dependence of $W(\mathbf{n})$ and $\tau(\mathbf{n})$. This dependence is taken into account by a unique anisotropy function $a_s(\mathbf{n})$ with $\tau(\mathbf{n}) = \tau_0 a_s(\mathbf{n})$ and $W(\mathbf{n}) = W_0 a_s(\mathbf{n})$ where τ_0 and W_0 are two constants. W_0 is the diffuse interface width and τ_0 is the kinetic characteristic time. λ is the strength of coupling with temperature θ or supersaturation U. The anisotropy function $a_s(\mathbf{n})$ will be explicitly introduced in the next section. Eq. (2.17) is the standard equation of heat diffusion for dimensionless temperature with an additional source term $(1/2)\partial_t\phi$. The physical meaning of this term is the release of latent heat at interface. Eq. (2.18) describes the spatiotemporal distribution of the normalized supersaturation field. $q(\phi) = (1-\phi)$ is a function canceling out diffusion within the solid. The physical meaning of the source term $-(1/2)\partial_t\phi$ is the absorption of the solute at the interface. The physical dimensions of W_0, τ_0, λ, κ and D are respectively $[W_0] \equiv [\mathscr{L}]$, $[\tau_0] \equiv [\mathscr{T}]$, $[\lambda] \equiv [-]$, $[\kappa] \equiv [\mathscr{L}]^2/[\mathscr{T}]$, and $[D] \equiv [\mathscr{L}^2/\mathscr{T}]$, where $[\mathscr{L}]$ indicates the length dimension and $[\mathscr{T}]$ indicates the time dimension.

Via a suitable asymptotic expansion, the equation of the sharp-interface model (from Eq. (2.8) to Eq. (2.12) can be derived [10], with the following expression for the capillary length d_0

$$d_0 = a_1\frac{W_0}{\lambda} \tag{2.20}$$

where the coupling constant λ is defined as [11]

$$\lambda = \frac{15L^2}{16Hc_pT_m} \tag{2.21}$$

For the model, $a_1 \approx 0.8839$ [10]. H is the barrier height of a double-well potential. $1/\lambda$ is a dimensionless measure of the barrier height H. Based on an analysis of the thin-interface limit, the kinetic coefficient β can be made to vanish [9] while:

$$\tilde{D} = \lambda a_2. \tag{2.22}$$

Measuring length and time in units of W_0 and τ_0, respectively, scales out these parameters from the PF equations, in which case the only parameters left are $\tilde{D}$, λ and Le$= \kappa/D$, the Lewis number, with $a_2 \approx 0.6267$ [10]. In all simulations presented here, the computational domain is a square geometry in two dimensions or a cubic configuration in three dimensions. Furthermore, zero-flux boundary conditions are rigorously enforced for all equations outlined above. For PF equation, the initialization of a nucleus takes the form of a diffusely defined sphere:

$$\phi(\boldsymbol{x},0) = \tanh\left[\frac{R_s - d_s}{\sqrt{2}W_0}\right], \tag{2.23}$$

where R_s is the radius of the initial crystal seed, d_s represents the distance characterized by $d_s = \left[(x-x_s)^2 + (y-y_s)^2 + (z-z_s)^2\right]^{1/2}$ and $\boldsymbol{x_s} = (x_s, y_s, z_s)^T$ denotes the center's position. Under this prescribed initial condition, the PF variable ϕ is defined as follows: $\phi = +1$ within the sphere (representing the solid phase), and $\phi = -1$ outside the sphere (representing the liquid phase). Moreover, the initial temperature is assumed to be a uniform constant across the entire computational domain and is maintained below the melting temperature. The initial condition of the normalized temperature is specified as:

$$\theta(\boldsymbol{x},0) = \theta_0 < 0. \tag{2.24}$$

In the following chapters, the undercooling defined by $\delta = -\theta_0$ will be specified.

Phase-field model for snowflakes The governing equations required later for simulating snowflake dynamics deviate slightly from Eq. (2.16). They encompass the mass conservation (or continuity) equation, momentum equation, phase-field equation, and supersaturation equation. The kinetics of the phase field are delineated by a parameter ϕ, signifying the solid and fluid phases upon reaching +1 (ice) and -1 (vapor), respectively. The reduced supersaturation of water vapor, defined as $U = (c - c^S_{sat})/c^S_{sat}$, introduces the saturation number density of vapor over ice at temperature T, denoted as $c^S_{sat}(T)$. The spatiotemporal evolution equations are expressed as per established

literature [1, 14, 16, 17]:

$$\tau_0 a_s^2(\mathbf{n})\frac{\partial \phi}{\partial t} = W_0^2 \boldsymbol{\nabla}_\Gamma \cdot \left(a_s^2(\mathbf{n})\right) \boldsymbol{\nabla}_\Gamma \phi + W_0^2 \boldsymbol{\nabla}_\Gamma \cdot \left(|\boldsymbol{\nabla}_\Gamma \phi|^2 a(\mathbf{n}) \frac{\partial a(\mathbf{n})}{\partial \boldsymbol{\nabla} \phi} \right) + (\phi - \phi^3) + \lambda B(\boldsymbol{n}) U (1-\phi^2)^2, \tag{2.25}$$

$$\frac{\partial U}{\partial t} + \left(\frac{1-\phi}{2}\right) \boldsymbol{u} \cdot \boldsymbol{\nabla}_\Gamma U = D \boldsymbol{\nabla}_\Gamma \cdot (q(\phi) \boldsymbol{\nabla}_\Gamma U) - \frac{L_{sat}}{2} B(\boldsymbol{n}) \frac{\partial \phi}{\partial t}, \tag{2.26}$$

where $\boldsymbol{n} = -\nabla\phi/|\nabla\phi|$ is the unit normal vector of ϕ. Considering the horizontal and vertical scaling of the interface for the snowflakes, the anisotropic space derivative is introduced via $\nabla_\Gamma = (\Gamma_x \partial_x, \Gamma_y \partial_y, \Gamma_z \partial_z)$. $B(\boldsymbol{n}) = (\Gamma_x^2 n_x^2 + \Gamma_y^2 n_y^2 + \Gamma_z^2 n_z^2)^{1/2}$ is the kinetic anisotropy function accounting for different water molecule attachment rates on the basal and prismatic faces of snowflakes. The parameter $\Gamma > 0$ governs the preference between horizontal ($\Gamma < 1$) and vertical ($\Gamma > 1$) growth. L_{sat} is the depletion rate of water molecules in vapor, due to ice phase growth.

2.4 Anisotropy function

This section focuses on the anisotropy function denoted as $a_s(\boldsymbol{n})$, which plays a pivotal role in determining the distinctive geometries of crystals. In the PF model, the $a_s(\boldsymbol{n})$ function only appears in the PF equation (see Eq. (2.16). We focus on the anisotropy function, which guides the growth of branches not solely along the main axes of the coordinate system but also exhibits a preferential growth pattern other than the main axes. To commence, we recapitulate the fundamental formulations of the $a_s(\boldsymbol{n})$ functions.

In 2D, the standard formulations are based on the angle φ between the normal vector of the interface and the x-axis. In PF models, the definition of the normal vector is given by $\boldsymbol{n} = -\nabla\phi/|\nabla\phi|$ and its components are $n_x = -\partial_x\phi/|\nabla\phi|$ and $n_y = -\partial_y\phi/|\nabla\phi|$. The angle is defined by: $\varphi = \arctan(n_y/n_x)$. Therefore, the angle φ is calculated from the order parameter ϕ. The standard anisotropy function $a_s(\varphi)$ in 2D is:

$$a_s(\varphi) = 1 + \varepsilon_s \cos\left[q\left(\varphi(\boldsymbol{x},t) - \varphi_0\right)\right] \tag{2.27}$$

where φ_0 represents a reference angle, ε_s denotes the strength of anisotropy, and q stands for the number of crystal tips. For instance, selecting $q = 4$ and $\varphi_0 = 0$ results in the formation of a crystal with four tips aligned along the main axes x and y. It is important to note that maximum growth occurs then when $\cos(4\varphi)$ equals one, which corresponds to multiple integer values of $\varphi = \pi/2$. Additionally, it is worth mentioning that modifications to the function $a_s(\varphi)$ are made when simulating faceted crystals [21, 22]. However, it is important to clarify that the present study

does not delve into the investigation of such crystal shapes.

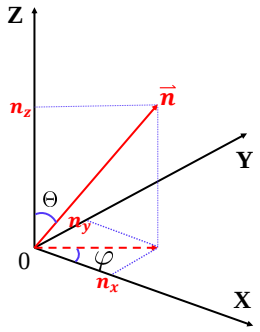

Figure 2.2: Description for the normal vector of the interface in 3D Cartesian axes.

In 3D, any scalar function can be decomposed on a basis of spherical functions depending on two angular parameters, namely, φ and Θ, defined on a spherical surface. Θ denotes the angle between XY-plane and the Z-axis, while φ represents the angle between X-axis and Y-axis (refer to Fig. 2.2). This mathematical framework is commonly referred to as spherical harmonics. For instance, $\cos(4\varphi)$ corresponds to the real part of the spherical harmonic $Y_{4,4}(\Theta,\varphi)$ in the XY-plane when $\Theta = \pi/2$. However, the expression of the function $a_s(\Theta,\varphi)$ in polar coordinate can be transferred into the forms of the function $a_s(\boldsymbol{n})$ in Cartesian coordinates. Consequently, the function $a_s(\pi/2,\varphi) = 1+\varepsilon_s\cos(6\varphi)$ can be expressed equivalently as $a_s(\boldsymbol{n})$, which is formulated as:

$$a_s(\mathbf{n}) = 1+\varepsilon_s(n_x^6 - 15n_x^4n_y^2 + 15n_x^2n_y^4 - n_y^6), \tag{2.28}$$

where $n_x = \sin\Theta\cos\varphi$, $n_y = \sin\Theta\sin\varphi$ and $n_z = \cos\Theta$. In Eq. (2.28), it represents the six main growing direction in the XY-plane when $\Theta = \pi/2$. $\mathscr{N} = (\mathscr{N}_x, \mathscr{N}_y, \mathscr{N}_z)$ in the advection term in Eq. (2.16) for six main growing directions in the XY-plane are written:

$$\begin{aligned}\mathscr{N}_x &= |\nabla\phi|a_s(\mathbf{n})12\varepsilon_s n_x\left(-3n_x^4n_y^2 + 10n_x^2n_y^4 - 3n_y^6\right),\\ \mathscr{N}_y &= |\nabla\phi|a_s(\mathbf{n})12\varepsilon_s n_y\left(3n_x^2n_y^4 - 10n_x^4n_y^2 + 3n_x^6\right),\end{aligned} \tag{2.29}$$

The anisotropy function for a growing direction <100> is:

$$a_s(\boldsymbol{n}) = 1 - 3\varepsilon_s + 4\varepsilon_s\sum_{\alpha=x,y,z} n_\alpha^4, \tag{2.30}$$

where α represents the x-, y-and z-axis in the cartesian coordinates and $\mathscr{N} = (\mathscr{N}_x, \mathscr{N}_y, \mathscr{N}_z)$ with a

growing direction <100> is:

$$\begin{aligned}
\mathscr{N}_x &= 16|\nabla\phi|a_s(\mathbf{n})\varepsilon_s n_x\left[n_y^4+n_z^4-n_x^2(n_y^2+n_z^2)\right],\\
\mathscr{N}_y &= 16|\nabla\phi|a_s(\mathbf{n})\varepsilon_s n_y\left[n_x^4+n_z^4-n_y^2(n_x^2+n_z^2)\right],\\
\mathscr{N}_z &= 16|\nabla\phi|a_s(\mathbf{n})\varepsilon_s n_z\left[n_x^4+n_y^4-n_z^2(n_x^2+n_y^2)\right],
\end{aligned} \tag{2.31}$$

Cubic harmonics are a set of functions that can be expressed as linear combinations of real spherical harmonics in a specific cubic coordinate system, as introduced by Puff et al. [23]. The function $Q(\boldsymbol{n}) = n_x^4+n_y^4+n_z^4$, as used in Eq. (2.30), can be derived from the cubic harmonic $K_{4,1}(\Theta,\varphi)$, which is proportional to the expression $\left[5\cos^4\Theta-3+5\sin^4\Theta(\cos^4\varphi+\sin^4\varphi)\right]$. The symbol $\propto$ indicates that the cubic harmonic $K_{4,1}$ is directly proportional to the provided function, with an associated normalization factor: Upon a change of variables into Cartesian coordinates, this function transforms into $K_{4,1}(\Theta,\varphi)\propto\left[5(n_x^4+n_y^4+n_z^4)-3\right]$.

By incorporating an additional cubic harmonic, such as $K_{6,1}$, the anisotropy function $a_s(\boldsymbol{n})$ can be generalized to account for various crystal growth directions. For example, to simulate the <110>-growth direction, one can utilize the formulation proposed by Hoyt et al. [24], as follows:

$$a_s(\boldsymbol{n}) = 1+\varepsilon_s\left(\sum_{\alpha=x,y,z}n_\alpha^4-\frac{3}{5}\right)+\gamma\left(3\sum_{\alpha=x,y,z}n_\alpha^4+66n_x^2n_y^2n_z^2-\frac{17}{7}\right), \tag{2.32}$$

where ε_s represents the anisotropy strength in the <100>-growth direction, and γ denotes the anisotropy strength in the <110>-growth direction. The expression on the right-hand side of the equation consists of three terms: the first term corresponds to the cubic harmonic $K_{0,0}=1$, the second term is associated with $K_{4,1}$ and is proportional to $[5Q(\boldsymbol{n})-3]$, and the final term relates to the cubic harmonic $K_{6,1}$, which is proportional to $[462S(\boldsymbol{n})+21Q(\boldsymbol{n})-17]$, where $S(n_x^2n_y^2n_z^2)$ represents a function defined in terms of products of the components of $\boldsymbol{n}$.

The $\mathscr{N}=(\mathscr{N}_x,\mathscr{N}_y,\mathscr{N}_z)$ for Eq. (2.32) are written:

$$\begin{aligned}
\mathscr{N}_x &= |\nabla\phi|a_s(\mathbf{n})n_x\left(4(\varepsilon_s+3\gamma)\left[n_y^4+n_z^4-n_x^2(n_y^2+n_z^2)\right]+132\gamma\left[2n_x^2n_y^2n_z^2-n_y^2n_z^2(n_y^2+n_z^2)\right]\right),\\
\mathscr{N}_y &= |\nabla\phi|a_s(\mathbf{n})n_y\left(4(\varepsilon_s+3\gamma)\left[n_x^4+n_z^4-n_y^2(n_x^2+n_z^2)\right]+132\gamma\left[2n_x^2n_y^2n_z^2-n_x^2n_z^2(n_x^2+n_z^2)\right]\right),\\
\mathscr{N}_z &= |\nabla\phi|a_s(\mathbf{n})n_z\left(4(\varepsilon_s+3\gamma)\left[n_x^4+n_y^4-n_z^2(n_x^2+n_y^2)\right]+132\gamma\left[2n_x^2n_y^2n_z^2-n_x^2n_y^2(n_x^2+n_y^2)\right]\right).
\end{aligned} \tag{2.33}$$

For a more comprehensive treatment of higher-order cubic harmonics defined in relation to functions $Q(\boldsymbol{n})$ and $S(\boldsymbol{n})$, we refer to Podmaniczky et al. [25]. The functions above will be used in the following chapters for benchmarks, which will be carried out for numerical implementation of the LBM.

Anisotropy function for snowflakes The anisotropy function for the growth of the snowflakes is given by:

$$a_s(\varphi,\Theta) = 1 + \varepsilon_{xy}\sin^6\Theta\cos 6\varphi + \varepsilon_z\cos 2\Theta. \tag{2.34}$$

It could be transferred to cartesian coordinate :

$$a_s(\boldsymbol{n}) = 1 + \varepsilon_{xy}(n_x^6 - 15n_x^4n_y^2 + 15n_x^2n_y^4 - n_y^6) + \varepsilon_z(2n_z^2 - 1), \tag{2.35}$$

where $n_x = \sin\Theta\cos\varphi$, $n_y = \sin\Theta\sin\varphi$ and $n_z = \cos\Theta$. ε_{xy} signifies the anisotropy strength in the xy-plane, while ε_z denotes the anisotropy strength in the z-direction. The anisotropy function $a_s(\boldsymbol{n})$ describes the formation of six-tip dendrites in the xy-plane, where the horizontal scaling of the interface is manifested, and two-tip dendrites in the z-direction, characterized by vertical scaling. This is achieved through an anisotropic space derivative denoted as $\nabla_\Gamma = (\Gamma_x\partial_x, \Gamma_y\partial_y, \Gamma_z\partial_z)$, which effectively reduces the interface width in the direction of slow growth.

The $\mathscr{N} = (\mathscr{N}_x, \mathscr{N}_y, \mathscr{N}_z)$ for Eq. (2.35) are written:

$$\mathscr{N}_x = |\nabla\phi|a_s(\mathbf{n})\left[-6\varepsilon_{xy}n_x\left(6n_y^6 + 6n_x^4n_y^2 + n_x^4n_z^2 + 5n_y^4n_z^2 - 20n_x^2n_y^4 - 10n_x^2n_y^2n_z^2\right) + 4\varepsilon_z n_y n_z^2\right], \tag{2.36}$$

$$\mathscr{N}_y = |\nabla\phi|a_s(\mathbf{n})\left[6\varepsilon_{xy}n_y\left(6n_x^6 + 6n_y^4n_x^2 + n_y^4n_z^2 + 5n_x^4n_z^2 - 20n_y^2n_x^4 - 10n_x^2n_y^2n_z^2\right) + 4\varepsilon_z n_x n_z^2\right], \tag{2.37}$$

$$\mathscr{N}_z = |\nabla\phi|a_s(\mathbf{n})\left[6\varepsilon_{xy}n_z\left(n_x^6 - 15n_x^4n_y^2 + 15n_x^2n_y^4 - n_y^6\right) - 4\varepsilon_z n_z\left(n_x^2 + n_y^2\right)\right]. \tag{2.38}$$

2.5 Coupling of solidification with flows

In this section, the model related to the coupling between solidification and flow models is introduced. It is assumed that solids are fixed and immobile in the flow and the density changes that occur during solidification are ignored. In addition, the fluid is considered incompressible. It describes a mathematical model for studying the effect of flow on the crystal growth, which is taken from [16–18, 26]. As equations of motion for the fluid velocity $\boldsymbol{u}$, we take the Navier-Stokes equations and the continuity equation for an incompressible viscous flow field as:

$$\frac{\partial}{\partial t}\left[\left(\frac{1-\phi}{2}\right)\boldsymbol{u}\right] + \boldsymbol{u}\cdot\nabla\left[\left(\frac{1-\phi}{2}\right)\boldsymbol{u}\right] = -\left(\frac{1-\phi}{2}\right)\frac{\nabla\boldsymbol{P}}{\rho_f} + \nu_f\nabla^2\left[\left(\frac{1-\phi}{2}\right)\boldsymbol{u}\right] + \boldsymbol{F_d}, \tag{2.39}$$

where $(1-\phi)\boldsymbol{u}/2$ cancels the velocity in the solid while $\phi = 1$. P represents the pressure of the flow and ρ_f denotes the fluid density. $\boldsymbol{F_d}$ is the force used to simulate the dissipation at the interface in the liquid momentum equation. In this model, it is assumed that the force is proportional to fluid kinematic viscosity ν_f and velocity $\boldsymbol{u}$. The force $\boldsymbol{F_d}$ modeling interaction with the solid phase is given as [16–18, 26]:

$$\boldsymbol{F_d} = -\nu_f \frac{h(1+\phi)^2(1-\phi)}{4W_0^2}\boldsymbol{u}, \tag{2.40}$$

where h is a dimensionless constant (h = 2.757), which ensures that the interface shear stress is correct for a simple shear flow [16]. W_0 is the interface width.

The continuity equation is:

$$\nabla \cdot \left[\left(\frac{1-\phi}{2}\right)\boldsymbol{u}\right] = 0, \tag{2.41}$$

We consider the influence of hydrodynamics on the solidification process by incorporating fluid velocity into the heat and species diffusion equations within the PF model. The PF equation, represented as Eq. (2.16), remains unaltered, while a convective term, $(1-\phi)\boldsymbol{u}/2$, is introduced into both the heat and species diffusion equations, as shown previously:

$$\frac{\partial \theta}{\partial t} + \left(\frac{1-\phi}{2}\right)\boldsymbol{u}\cdot\nabla\theta = \kappa\nabla^2\theta + \frac{1}{2}\frac{\partial \phi}{\partial t} \tag{2.42}$$

$$\frac{\partial U}{\partial t} + \left(\frac{1-\phi}{2}\right)\boldsymbol{u}\cdot\nabla U = D\nabla\cdot(q(\phi)\nabla U) - \frac{1}{2}\frac{\partial \phi}{\partial t} \tag{2.43}$$

2.6 Summary

In this chapter, a diffuse interface or PF model was introduced. An evolution equation for the phase field is obtained through a simplified derivation starting from the classical velocity dependent Gibbs–Thomson equation for a sharp solid–liquid interface.

The PF model is based on three coupled PDEs, the first one for modeling an order parameter ϕ in the PF, the second one for modeling the supersaturation U and the third one for modeling the dimensionless temperature θ. The correlation between this model and the sharp interface model is established through a mathematical analysis termed 'matched asymptotic expansion.' This analytical approach reveals connections between the parameters of the PF equation ($W(\boldsymbol{n})$, $\tau(\boldsymbol{n})$, and λ) and fundamental physical parameters, including the capillary length d_0 and the kinetic coefficient β. Then, the anisotropy function $a_s(\boldsymbol{n})$, which only exists in the PF equation, is introduced by using the normal vector n for the setting of crystal growth directions in 2D and 3D.

In the context of crystal growth problems, fluid flow often assumes a predominant role. A

comprehensive depiction of crystal growth necessitates the integration of the growth model with a fluid flow solver. In this particular model, the PF equation remains unaltered; however, an advective term is introduced in the heat equation, and a force term is appended in the momentum equation. Notably, the order parameter ϕ does not directly influence the heat equation and NS equations. To nullify the advective terms within the solid phase, a novel function $(1-\phi)/2$ is employed. This function equates to 0 in the solid phase and 1 in the liquid phase, effectively canceling out the advective effects within the solid component.

In the limit of a thin interface, this model offers several advantages: (a) it converges to the classical equations and boundary conditions applicable to a macroscopically sharp interface, rendering it computationally practical irrespective of its derivation; (b) The PF equation, as well as the conservation equations, completely avoid the explicit tracking of the interface, the explicit satisfaction of interfacial conditions, and the computation of interface normals and curvatures; (c) computations can be conducted in the limit where interface kinetic effects approach zero.

In the next chapter, a LBM will be developed for the simulation of the PF model and a new equilibrium distribution function established for solving the PF equation with a modified method for ADE.

Chapter 3

Lattice Boltzmann Method

Contents

This chapter is devoted to the application of the LBM to the PF model outlined in Chapter 2. The LBM is recognized as a powerful tool for simulating fluid dynamics problems. In this study, the standard lattice Boltzmann equation (LBE) with classical equilibrium distribution function was modified to simulate solid-liquid phase change in crystal growth phenomena.

The principle of the LBM can be found in many classic references in the literature, e.g. [27]. The LBM scheme for phase, supersaturation, and temperature field equations developed in this paper is based on the BGK approximation of the collision term we will review. In order to simulate the anisotropic term in the phase field equation, the equilibrium distribution function (EDF) is modified compared with the standard method of ADE [28]. The equilibrium distribution function is based on the asymptotic development shown in the appendix A (Chapman Enskog expansion).

3.1 Introduction

Significant efforts have been directed towards the development of mathematical models and numerical tools. These mathematical models can be categorized based on the available time and length scales of the physical problem, encompassing continuum, microscopic, and mesoscopic approaches. Microscopic models and simulations, such as Molecular Dynamic simulations [29–33], have been employed to analyze fundamental processes such as surface adsorption and diffusion. Although these simulations are physically sound, they have limitations in terms of both time and space, making them inefficient for simulating the complete evolution of a crystal (especially at later stages when instabilities appear and the crystal grow in size). So-called mesoscopic formulations are an interesting alternative. In recent years, there has been a notable increase in the utilization of LBM for investigating multiphase flows and phase transitions. The LBM locates at the middle of continuum and microscopic methods. It integrates microscopic physics with computationally affordable methods, acting as a bridge between molecular dynamics simulations on the microscopic scale and simulations grounded in macroscopic conservation laws. Particularly beneficial for intricate systems where macroscopic governing equations remain undetermined, yet microscopic physics is well-defined, the lattice Boltzmann method has emerged as a valuable tool in academic research.

Historically, it originated from the lattice gas automata (LGA), specifically focusing on the Frisch, d'Humières, Hasslacher (FHP) model [34, 35]. However, the FHP model presented several challenges, including statistical noise, a lack of Galilean invariance, low Reynolds number, and exponential complexity [36]. To address these issues, McNamara and Zanetti [37] adopted the lattice Boltzmann equation concept from Frisch et al. [34, 38]. Koelman [39] and Chen et al. [40] further simplified the collision operator by using a constant value known as relaxation parameter. The LB-BGK model emerged with the linearization and simplification of the collision operator in the

LBE [41, 42]. This model marked a significant milestone, offering increased flexibility, Galilean invariance, higher Reynolds number, and significantly reduced complexity for lattice gas automata. Subsequently, the LB-BGK model established its independence through the direct phase space discretization of the continuous Boltzmann-BGK equation [38] and thrived with the introduction of multi-relaxation time (MRT) models [43, 44], demonstrating enhanced stability and accuracy. But in this paper, we only focus on the well-known SRT-LBM with BGK operator [42] and the application for the ADE and the PF equation.

The LBM, developed over the past decades, has now become a popular alternative to classical solvers for the NS equations [45]. It has since been extended to a variety of applications and flow regimes such as multi-phase flows [46], flows in porous media, turbulence and multi-component flows [47–49]. It has also been used, in combination with classical solvers for the solid phase, to simulate crystal growth [18, 50–56]. In these models, the LBM was adopted as a solver of NS equations, and the PF equation was used to model crystal growth and morphological transitions. While initially developed as a discrete solver for the Boltzmann equation in the hydrodynamic regime, it has also widely been used as a solver for different types of parabolic PDE via appropriate parametrization of the equilibrium state and the collision-streaming operators. In that same spirit a number of work have proposed LBM-based formulations to solve the PF evolution equation, utilizing the advantages of LBM, such as easy implementation and straightforward parallelization. Younsi and Cartalade [1] proposed a full implementation of the PF model in the LB framework. They modified the standard LB equations and equilibrium distribution function to introduce anisotropic surface tension and growth rate effects. The proposed model was successfully used to simulate anisotropic and dendritic growth. While readily applied to generic systems, these models have rarely been used to simulate realistic systems.

For the PF-LB model in the following chapters, time, space, and particle velocity are discrete. While a number of different publications have looked into LBM-based models for crystal growth simulation they have been usually limited to simple and generic systems. Here, we use a pure LBM solver for the PF coupled to flow and species/temperature solvers to model, for the first time, a physically-relevant system with complex habit. Furthermore the coupling between the flow field and species/temperature/phase fields allows us to model for the first time, to the authors' knowledge, flow-induced non-symmetrical growth effects with LBM.

In this chapter, we first detail each stage of the method: the SRT-LBM model is presented and the equilibrium distribution functions is defined as well as the relaxation rates. Then, D2Q9 and D3Q19 lattices models are introduced and some details given about the algorithm implementation. In Sec. 3.2, we start the description with the LB scheme for the temperature and supersaturation equation, because it is the simplest equation of the model for which the standard LB method was applied. For the phase-field equation, the collision step and the equilibrium distribution function

are modified. Derivation of equilibrium distribution functions, which couples the physical variables and the lattice dependent quantities, is the most delicate part of the numerical scheme. The derivations of such function necessitate to carry out asymptotic calculations (Chapman–Enskog expansion) that can be found in Appendix A for Eq. (2.16).

3.1.1 SRT-BGK model

As we have seen, the Boltzmann equation is the starting point of the LBM. Considering a discretization of the Boltzmann equation in time and space, the distribution function $f_i(\boldsymbol{x},t)$ is based on the discrete-velocity $\boldsymbol{c_i} = (c_{ix}, c_{iy}, c_{iz})$ at position $\boldsymbol{x}$ and time t. The index i identifies the moving direction on a lattice: $i = 0, 1, ..., q-1$ where q is the total number of directions. The lattice choice depends on the physical problem to be simulated. The lattice used in this work are presented in Fig. 3.1. Here, the standard LBE with the BGK approximation for the collision term can be regarded as:

$$f_i(\boldsymbol{x}+\boldsymbol{c_i}\delta t, t+\delta t) - f_i(\boldsymbol{x},t) = -\frac{1}{\tau}[f_i(\boldsymbol{x},t) - f_i^{eq}(\boldsymbol{x},t)]\delta t, \tag{3.1}$$

where $f_i(\boldsymbol{x}+\boldsymbol{c_i}\delta t, t+\delta t)$, $f_i(\boldsymbol{x},t)$ are the discrete distribution functions. τ is the single relaxation time. And the lattice is constructed such that the two adjacent nodes in the lattice are connected by the spatial discrete velocity $\boldsymbol{c}_i$. $f_i^{eq}(\boldsymbol{x},t)$ represents the local equilibrium distribution function.

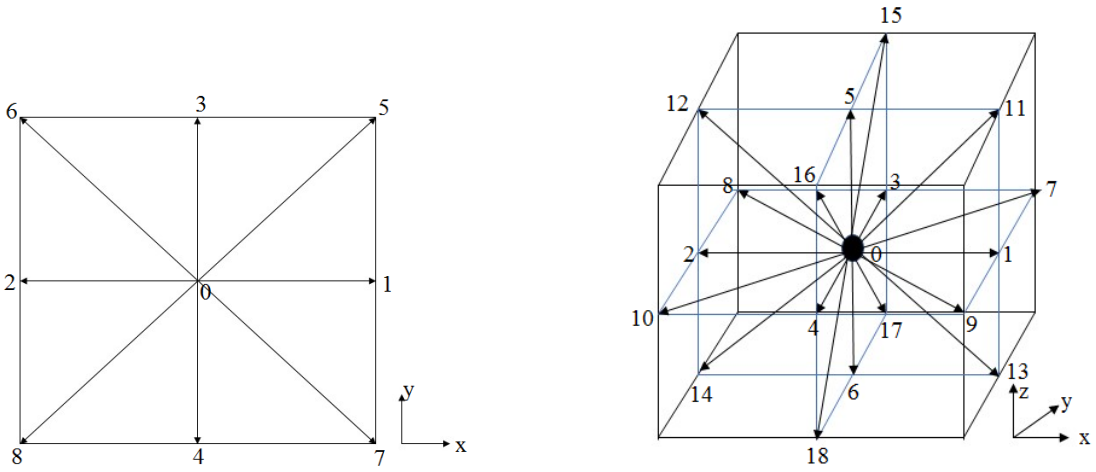

(a) (b)

Figure 3.1: Velocity direction vectors of (a) D2Q9; (b) D3Q19 structure

The Eq. (3.1) fully describes the two stages of particle distribution evolution at each time

step. First, it captures the collision of particles, governing their relaxation towards equilibrium. Subsequently, it accounts for the streaming of particles, involving the shift of distribution functions along lattice directions to neighboring lattice cells. Fig. 3.2 shows graphically the D2Q9 model and how the streaming step takes place for the interior nodes.

$$\text{Collision}: \quad f_i'(\boldsymbol{x},t) = f_i(\boldsymbol{x},t) - \frac{1}{\tau}[f_i(\boldsymbol{x},t) - f_i^{eq}]\delta t, \tag{3.2}$$

$$\text{Streaming}: \quad f_i(\boldsymbol{x}+\boldsymbol{c}_i\delta t, t+\delta t) = f_i'(\boldsymbol{x},t). \tag{3.3}$$

The derived evolution equation is formed through the equilibrium torque of the function. The

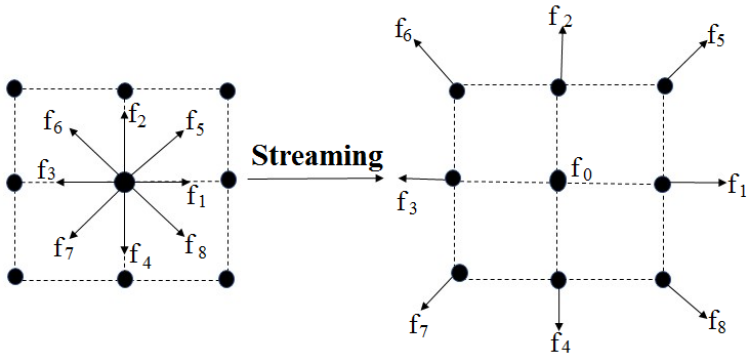

Figure 3.2: Illustration of the streaming process of a lattice node.

initial three moments of the equilibrium distribution function are defined as:

$$\text{Zeroth}-\text{order moment}: \quad \sum_{i=0}^{q-1} f_i^{eq}, \tag{3.4}$$

$$\text{First}-\text{order moment}: \quad \sum_{i=0}^{q-1} \boldsymbol{c}_i f_i^{eq}, \tag{3.5}$$

$$\text{Second}-\text{order moment}: \quad \sum_{i=0}^{q-1} \boldsymbol{c}_i \boldsymbol{c}_i f_i^{eq}. \tag{3.6}$$

where q is the number of discretization directions. The zeroth-order moment is a scalar, the first-order moment is essentially a vector, and the second-order moment is a second-order tensor.

3.1.2 Two- and three dimensional stencils

Sec. 3.1.1 represented a continuous equilibrium distribution function by a discrete form, requiring the selection of weight coefficients. The determination of these weight factors is related to a third-order Hermite formula [38, 57].

In the discretized form of the LBE above, regular lattices in the physical space are populated with discrete particles. Particles traverse from one lattice node to another, guided by discrete particle velocities c_i, and suffer collisions at these nodes.The discrete velocities, denoted by DdQq, corresponds to the spatial dimension (d) and the total number of lattice velocities (q). In this study, we specifically utilize two discrete velocity models: the 9-velocity model on a 2D square lattice, referred to as the D2Q9 model, and the 19-velocity model on a 3D cubic lattice, denoted as the D3Q19 model. Illustrations of these two discrete velocity models are provided in Fig. 3.1.

For a two dimensional D2Q9 model (see Fig. 3.1(a)), a particle is restricted to stream in a possible set of 9 directions which involves 9 velocity vectors, including the one staying at rest. Then the weight coefficients ω_i, for D2Q9 model are given by:

$$\omega_i = \begin{cases} \frac{4}{9}, & i = 0 \\ \frac{1}{9}, & i = 1,...,4 \\ \frac{1}{36}. & i = 5,...,8 \end{cases} \tag{3.7}$$

The corresponding lattice velocity $c_i = [c_{ix}, c_{iy}]$ for D2Q9 are

$$c_i = \begin{cases} (0,0), & i = 0 \\ (\pm 1,0),(0,\pm 1), & i = 1,...,4 \\ (\pm 1,\pm 1). & i = 5,...,8 \end{cases} \tag{3.8}$$

And for the D3Q19 model, the weights coefficients ω_i are:

$$\omega_i = \begin{cases} \frac{1}{3}, & i = 0 \\ \frac{1}{18}, & i = 1,...,6 \\ \frac{1}{36}. & i = 7,...,18 \end{cases} \tag{3.9}$$

The velocity vectors $c_i = [c_{ix}, c_{iy}, c_{iz}]$ in D3Q19 model are:

$$c_i = \begin{cases} (0,0,0), & i = 0 \\ (\pm 1,0,0),(0,\pm 1,0),(0,0,\pm 1), & i = 1,...,6 \\ (\pm 1,\pm 1,0),(\pm 1,0,\pm 1),(0,\pm 1,\pm 1). & i = 7,...,18 \end{cases} \tag{3.10}$$

3.1.3 The classical LB scheme for the ADE

The ADE finds widespread application in engineering physics problems, particularly in simulating solute transport in porous media [58] and the evolution of temperature (or supersaturation) fields in interface-tracking problems [59]. In the exploration of the solidification challenge presented by

dilute binary mixtures [60], specifically within the domain of interface tracking, the ADE exhibits sensitivity to the PF value ϕ. The value of the phase field (PF) varies across grid positions within the computational domain, necessitating attentions of spatial variations in ADE parameters. The inherent structural heterogeneity of porous media amplifies the imperative to treat ADE parameters as position-dependent functions.

In this section, we present the LBM for solving the PF model introduced in Chapter 2. In order to establish the equilibrium distribution function relative to the PF equation, the description is based on an analogy with the classical LB scheme for solving the following ADE:

$$\frac{\partial C}{\partial t} = \nabla \cdot (D\nabla C) - \nabla \cdot (\boldsymbol{u}C) + Q, \tag{3.11}$$

where D is the diffusion coefficient, $\boldsymbol{u}$ is the velocity and Q is the source term. We apply the following LB scheme [61]:

$$f_i(\boldsymbol{x} + \boldsymbol{c}_i\delta t, t + \delta t) - f_i(\boldsymbol{x}, t) = -\frac{1}{\eta_C}[f_i(\boldsymbol{x}, t) - f_i^{eq}(\boldsymbol{x}, t)]\delta t + \omega_i Q(\boldsymbol{x}, t)\delta t, \tag{3.12}$$

where η_C is the relaxation time. ω_i is given by Eq. (3.7) and Eq. (3.9) and the lattice velocity is given in Eq. (3.8) and Eq. (3.10). The equilibrium distribution function $f_i^{eq}(\boldsymbol{x}, t)$ is defined as:

$$f_i^{eq}(\boldsymbol{x}, t) = \omega_i C(\boldsymbol{x}, t)\left(1 + \frac{1}{c_s^2}\boldsymbol{c}_i \cdot \boldsymbol{u}(\boldsymbol{x}, t)\right). \tag{3.13}$$

The sound speed c_s is a lattice-dependent coefficient which arises from the calculation of the second-order moment. For both D2Q9 and D3Q19 model, $c_s = \delta x/(\sqrt{3}\delta t)$.

The initial three moments of the equilibrium distribution function are:

$$\text{Zeroth} - \text{order moment}: \quad \sum_{i=0}^{q-1} f_i^{eq} = C, \tag{3.14}$$

$$\text{First} - \text{order moment}: \quad \sum_{i=0}^{q-1} \boldsymbol{c}_i f_i^{eq} = \boldsymbol{u}C\frac{\delta t}{\delta x}, \tag{3.15}$$

$$\text{Second} - \text{order moment}: \quad \sum_{i=0}^{q-1} \boldsymbol{c}_i \boldsymbol{c}_i f_i^{eq} = c_s^2 C\boldsymbol{I}, \tag{3.16}$$

where q is the number of discretization directions. Here, the zeroth-order moment represents the scalar C, the first-order moment denotes the vector $\boldsymbol{u}C$, and $\boldsymbol{I}$ is the identity tensor of rank 2.

The diffusion coefficient D is linked to the relaxation time η_C and it defined by:

$$\eta_C = \frac{1}{c_s^2} D + \frac{\delta t}{2}. \tag{3.17}$$

In this scheme, the ADE diffusive term, $\Delta \cdot (D\Delta C)$ is accounted for by the first term enclosed in brackets on the right-hand side of the Eq. (3.13) while the advective term, -$\Delta \cdot (\boldsymbol{u}C)$ is accounted for by the second term. The presence of the function C in the diffusive and advective terms explains its presence in factor of Eq. (3.13).

Eq. (2.16)-(2.18) in chapter 2 represent the mathematical model considered in this work.In this section, the numerical method based on the LBM was described for each equation of the model. The LBM is an evolution equation in time and space of a discrete function, the distribution function of particles, which is defined over a lattice. The choice of the lattice determines the number of streaming directions of the distribution function. Once the LBM is defined, the algorithm can be summarized in three main operations applied on this distribution function: the first one is a moving step on the lattice; the second one is a collision step that relaxes the distribution function towards an equilibrium distribution function, with a relaxation rate. Finally, the last stage is to update the physical variable, such as the dimensionless temperature, or the phase field in Sec. 3.2, by computing its moment of order zero.

Anisotropy ADE The standard ADE involves a scalar diffusion coefficient D, but in an inhomogeneous system, the diffusion coefficient is anisotropic in solute transport process. It may be necessary to replace it by a diffusion tensor $\mathbf{D}$. This makes anisotropic and cross-diffusion possible: the former is caused by different diagonal elements of $\mathbf{D}$, the latter by non-zero off-diagonal elements of $\mathbf{D}$. Advection-diffusion describes the diffusion of a quantity ϕ subject to an external drift u. It can be expressed by the differential equation:

$$\partial_t \phi + \nabla \cdot (\phi \mathbf{u}) = \nabla \cdot (\mathbf{D} \nabla \phi), \tag{3.18}$$

where $\boldsymbol{u}$ is a velocity and $\mathbf{D}$ the diffusion tensor, it can be written by the scaling parameter Γ:

$$\mathbf{D} = \begin{bmatrix} \Gamma_{xx} & \Gamma_{xy} \\ \Gamma_{yx} & \Gamma_{xy} \end{bmatrix} D, \tag{3.19}$$

LBM provides a mesoscopic description of a physical system in terms of density distribution

function $f_i(r,t)$. The single-time relaxation LB model reads

$$f_i(x+c_i\delta t, t+\delta t) = \left(1-\frac{1}{\tau}\right) f_i + \frac{1}{\tau} f_i^{eq}. \tag{3.20}$$

where f_i^{eq} is an equilibrium function. In this section a new equilibrium function is derived by Chapman-Enskog using second order of moment [62]:

$$f_i^{eq} = \omega_i \rho \left(1 + \frac{c_i u}{c_s^2} + \frac{1}{2c_s^4}\left[(c_{ix}^2 - c_s^2)(\Gamma_x x - 1) + (c_{iy}^2 - c_s^2)(\Gamma_y y - 1) + \Gamma_{xy} c_{ix}\cdot c_{iy} + \Gamma_{yx} c_{ix}\cdot c_{iy}\right]\right). \tag{3.21}$$

where the sound speed $c_s = \delta x/\sqrt{3}\delta t$ in D2Q9 model. c_i is the lattice velocity; c_{ix} and c_{iy} are the lattice velocity in x-axis and y-axis directions, respectively.

In FD method, Eq. (3.18) could be described by:

$$\begin{aligned}
\frac{\phi^{n+1}(x,y) - \phi^n(x,y)}{\delta t} = &-\frac{u_x(\phi^n(x+\delta x,y) - \phi^n(x-\delta x,y))}{2} \\
&-\frac{u_y(\phi^n(x,y+\delta y) - \phi^n(x,y-\delta y))}{2} \\
&+\Gamma_{xx} D\left(\frac{\phi^n(x+\delta x,y) - 2\phi^n(x,y) + \phi^n(x-\delta x,y)}{\delta^2 x}\right) \\
&+\Gamma_{yy} D\left(\frac{\phi^n(x,y+\delta y) - 2\phi^n(x,y) + \phi^n(x,y-\delta y)}{\delta^2 y}\right) \\
+\Gamma_{xy} D\left(\frac{\phi^n(x+\delta x,y+\delta y) - \phi^n(x+\delta x,y-\delta y) - \phi^n(x-\delta x,y+\delta y) + \phi^n(x-\delta x,y-\delta y)}{4\delta y \delta x}\right) \\
+\Gamma_{yx} D\left(\frac{\phi^n(x+\delta x,y+\delta y) - \phi^n(x-\delta x,y+\delta y) - \phi^n(x+\delta x,y-\delta y) + \phi^n(x-\delta x,y-\delta y)}{4\delta x \delta y}\right).
\end{aligned} \tag{3.22}$$

The initial ϕ is set from a Gaussian hill [63]:

$$\phi(\mathbf{x}, t=0) = \frac{\phi_0}{2\pi\sigma_0^2} \exp\left(-\frac{\mathbf{x}^2}{2\sigma_0^2}\right). \tag{3.23}$$

where σ_0^2 is the initial variance and ϕ_0 is the total concentration. In the presence of an advection velocity u, the time evolution has an analytical solution [64, 65]:

$$\phi(\mathbf{x}, t) = \frac{\phi_0}{2\pi\sqrt{|\boldsymbol{\sigma}_t|}} \exp\left(-\frac{1}{2}\boldsymbol{\sigma}_t^{-1} : (\mathbf{x}-\mathbf{u}t)(\mathbf{x}-\mathbf{u}t)^{\mathbf{T}}\right). \tag{3.24}$$

where $\boldsymbol{\sigma}_t = \sigma_0^2\mathbf{I} + 2t\mathbf{D}$, $|\boldsymbol{\sigma}_t|$ the determinant value of $\boldsymbol{\sigma}_t$, respectively. The total concentration is $\phi_0 = 2\pi\sigma_0^2$ with $\sigma_0 = 0.01$ (here, σ_0 is small enough to adopt later a periodic boundary condition).

The diffusion tensor in 2D is:

$$\mathbf{D} = \begin{bmatrix} D_{xx} & D_{xy} \\ D_{yx} & D_{yy} \end{bmatrix} \tag{3.25}$$

Therefore, $\boldsymbol{\sigma_t}$ is:

$$\boldsymbol{\sigma_t} = \begin{bmatrix} \sigma_0^2 + 2tD_{yy} & 2tD_{yx} \\ 2tD_{xy} & \sigma_0^2 + 2tD_{xx} \end{bmatrix} \tag{3.26}$$

$|\boldsymbol{\sigma_t}|$ is:

$$|\boldsymbol{\sigma_t}| = (\sigma_0^2 + 2tD_{xx})(\sigma_0^2 + 2tD_{yy}) - 4t^2 D_{xy}D_{yx} \tag{3.27}$$

$\boldsymbol{\sigma_t}^{-1}$ is:

$$\boldsymbol{\sigma_t}^{-1} = \frac{1}{|\boldsymbol{\sigma_t}|}\sigma_t^* \tag{3.28}$$

$$\boldsymbol{\sigma_t^*} = \begin{bmatrix} \sigma_0^2 + 2tD_{yy} & 2tD_{yx} \\ 2tD_{xy} & \sigma_0^2 + 2tD_{xx} \end{bmatrix} \tag{3.29}$$

And $\boldsymbol{\sigma_t^*} : (\mathbf{x} - \mathbf{u}t)(\mathbf{x} - \mathbf{u}t)^{\mathbf{T}}$ is:

$$\begin{aligned} \boldsymbol{\sigma_t^*} : (\mathbf{x} - \mathbf{u}t)(\mathbf{x} - \mathbf{u}t)^{\mathbf{T}} = {} & (\sigma_0^2 + 2tD_{yy})(x - u_x t)^2 + 2t(x - u_x t)(y - u_y t)D_{xy} \\ & + 2t(x - u_x t)(y - u_y t)D_{yx} + (\sigma_0^2 + 2tD_{xx})(y - u_y t)^2 \end{aligned} \tag{3.30}$$

Eq. (3.24) could be also written in 2D:

$$\begin{aligned} \phi(\mathbf{x}, t) = {} & \frac{\phi_0}{2\pi\sqrt{(\sigma_0^2 + 2tD_{xx})(\sigma_0^2 + 2tD_{yy}) - 4t^2 D_{xy}D_{yx}}} \cdot \\ & \exp\left(-\frac{1}{2|\boldsymbol{\sigma_t}|}\left[(\sigma_0^2 + 2tD_{yy})(x - u_x t)^2 + (\sigma_0^2 + 2tD_{xx})(y - u_y t)^2 - 2t(x - u_x t)(y - u_y t)(D_{xy} + D_{yx})\right]\right) \end{aligned} \tag{3.31}$$

The error concerning the diffusion term compared to the analytical solution is recovered with L^2-global distribution errors [64]:

$$E_{l^2} = \sqrt{\frac{\sum_i (C_i - C_i^{th})^2}{\sum_i (C_i^{th})^2}}. \tag{3.32}$$

where the summation is taken over all lattice points.

3.2 LBM-BGK method for crystal growth models

The PF model is solved by the transport diffusion equation. The D2Q9 and D3Q19 stencils are adopted for 2D and 3D, respectively. Temperature and supersaturation equations are based on the analogy with the classical LB scheme used to solve ADE in the previous section. Three new distribution function g_i, p_i and h_i are accounting for the temperature, supersaturation and phase-field, respectively. For flow field, the distribution function f_i represents the density and fluid moment.

3.2.1 Temperature equation

The LB scheme for solving temperature equation Eq. (2.17) is the standard one for solving the diffusion equation. The space/time evolution equation of the thermal field is modeled using an advection-diffusion-reaction LB-based discrete kinetic formulation defined as [61, 66]:

$$g_i(\boldsymbol{x}+\boldsymbol{c}_i\delta t, t+\delta t) - g_i(\boldsymbol{x},t) = \delta t\Omega_i(\boldsymbol{x},t) + \omega_i Q_\theta(\boldsymbol{x},t)\delta t, \tag{3.33}$$

where Q_θ is the source term defined as:

$$Q_\theta(\boldsymbol{x},t) = -\frac{1}{2}\frac{\partial\phi}{\partial t}(\boldsymbol{x},t). \tag{3.34}$$

The collision operator $\Omega_i(\boldsymbol{x},t)$ for the thermal field is:

$$\Omega_i(\boldsymbol{x},t) = \frac{1}{\tau_\theta}\left[g_i^{(eq)}(\boldsymbol{x},t) - g_i(\boldsymbol{x},t)\right]. \tag{3.35}$$

where $g_i^{(eq)}(\boldsymbol{x},t)$ is the EDF defined as:

$$g_i^{(eq)}(\boldsymbol{x},t) = \omega_i\theta(\boldsymbol{x},t)\left[1+\frac{\boldsymbol{c}_i\cdot\boldsymbol{u}}{c_s^2}\right]. \tag{3.36}$$

where $\boldsymbol{u}$ is the velocity of the flow. The temperature $\theta(\boldsymbol{x},t)$ is computed locally as the zeroth-order moment of g_i:

$$\theta(\boldsymbol{x},t) = \sum_i g_i(\boldsymbol{x},t), \tag{3.37}$$

and the relaxation coefficient τ_θ is tied to the thermal diffusion coefficient κ in the fluid:

$$\tau_\theta = \frac{\kappa}{c_s^2} + \frac{\delta t}{2}. \tag{3.38}$$

The sound velocity c_s^2 depends on the stencil structure and is derived from the second-order moment of equilibrium distribution function $g_i^{eq}(\boldsymbol{x},t)$. For D2Q9 and D3Q19 model, $c_s^2 = 1/3$ in unit of $\delta x/\delta t$. The thermal diffusivity κ is a function of space and time and the relaxation time must be updated at each time step. It should be noted that the source term $Q_\theta(\boldsymbol{x},t)$ represents the time derivative of the PF equation. Therefore, the thermal equation should be resolved after the calculation of the PF equation. At last, the advection term can be easily resolved by modifying the equilibrium distribution function g_i^{eq} considering the coupling with flow.

3.2.2 Supersaturation equation

The LB scheme for solving supersaturation equation Eq. (2.18) is introduced in this section. The space/time evolution equation of the supersaturation field is modeled using an ADE LB-based discrete kinetic formulation defined as [61, 66]:

$$p_i(\boldsymbol{x}+\boldsymbol{c}_i\delta t, t+\delta t) - p_i(\boldsymbol{x},t) = \delta t\Omega_i(\boldsymbol{x},t) + \omega_i Q_U(\boldsymbol{x},t)\delta t, \tag{3.39}$$

where Q_U is the source term defined as:

$$Q_U(\boldsymbol{x},t) = \frac{1}{2}\frac{\partial\phi}{\partial t}(\boldsymbol{x},t). \tag{3.40}$$

The collision operator $\Omega_i(\boldsymbol{x},t)$ for the thermal field is:

$$\Omega_i(\boldsymbol{x},t) = \frac{1}{\tau_U}\left[p_i^{(eq)}(\boldsymbol{x},t) - p_i(\boldsymbol{x},t)\right]. \tag{3.41}$$

where $p_i^{(eq)}(\boldsymbol{x},t)$ is the EDF defined as:

$$p_i^{(eq)}(\boldsymbol{x},t) = \omega_i U(\boldsymbol{x},t)\left[1 + \frac{\boldsymbol{c}_i\cdot\boldsymbol{u}}{c_s^2}\right]. \tag{3.42}$$

where $\boldsymbol{u}$ is the velocity of the flow. The supersaturation $U(\boldsymbol{x},t)$ is computed locally as the zeroth-order moment of p_i:

$$U(\boldsymbol{x},t) = \sum_i p_i(\boldsymbol{x},t), \tag{3.43}$$

In the generitic lattice BGK scheme for ADE, the diffusion term $Dq(\phi)$ would be related to the relaxation time η_U with the relationship $Dq(\phi) = c_s^2(\eta_U - 1/2)\delta x^2/\delta t$. In Eq. (2.18), the interpolation function $q(\phi)$ cancels the diffusion coefficient in the solid phase. The relaxation

coefficient τ_U is then tied to the diffusion coefficient D in the fluid:

$$\tau_U = \frac{D(\phi)}{c_s^2} + \frac{\delta t}{2}. \tag{3.44}$$

The algorithm follows a sequential process: upon solving the phase field equation, ϕ is employed to calculate the temporal variations in supersaturation U and temperature θ. For each equation, the standard procedures of the LBM are applied.

3.2.3 Phase-field equation

The PF Eq. (2.16) is modeled using a modified LB scheme defined as [61, 67]:

$$\begin{aligned} a_s^2(\boldsymbol{n}) h_i(\boldsymbol{x}+\boldsymbol{c}_i\delta t, t+\delta t) \;=\; & h_i(\boldsymbol{x},t) - \left(1-a_s^2(\boldsymbol{n})\right) h_i(\boldsymbol{x}+\boldsymbol{c}_i\delta t, t) - \\ & \frac{1}{\eta_\phi(\boldsymbol{x},t)}\left[h_i(\boldsymbol{x},t) - h_i^{eq}(\boldsymbol{x},t)\right] + \\ & \omega_i Q_\phi(\boldsymbol{x},t)\frac{\delta t}{\tau_0}, \end{aligned} \tag{3.45}$$

where the scalar function Q_ϕ is the source term of the PF. As coupling with supersaturation field, it is defined by:

$$Q_\phi = (\phi - \phi^3) + \lambda_2 U (1-\phi^2)^2. \tag{3.46}$$

As coupling with temperature field, it is defined by:

$$Q_\phi = (\phi - \phi^3) - \lambda_1 \theta (1-\phi^2)^2. \tag{3.47}$$

Considering the coupling with both temperature and supersaturation field in Eq. (2.16), the source term Q_ϕ is given by:

$$Q_\phi = (\phi - \phi^3) + (\lambda_2 U - \lambda_1 \theta)(1-\phi^2)^2, \tag{3.48}$$

while the EDF h_i^{eq} is defined as:

$$h_i^{eq} = \omega_i \left(\phi - \frac{1}{2c_s^2}\boldsymbol{c}_i \cdot \frac{W_0^2}{\tau_0} |\boldsymbol{\nabla}\phi|^2 \frac{\partial (a_s^2(\boldsymbol{n}))}{\partial \boldsymbol{\nabla}\phi} \frac{\delta t}{\delta x} \right). \tag{3.49}$$

The local value of the order parameter ϕ is calculated as:

$$\phi = \sum_i h_i, \tag{3.50}$$

The relaxation time η_ϕ is a function of position and time and must be updated at each time-step as:

$$\eta_\phi = \frac{1}{c_s^2} a_s^2(\boldsymbol{n}) \frac{W_0^2}{\tau_0} + \frac{\delta t}{2}. \tag{3.51}$$

LBM scheme for snowflakes The lattice Boltzmann scheme applied to simulate the phase-field is based on BGK collision as:

$$\begin{aligned} a_s^2(\mathbf{n}) g_i(x+\mathbf{e}_i \mathrm{d}x, t+\mathrm{d}t) = g_i(x,t) - (1-a_s^2(\mathbf{n})) g_i(x+\mathbf{e}_i \mathrm{d}x, t) \\ - \frac{1}{\eta_\phi(x,t)} \left[g_i(x,t) - g_i^{(0)}(x,t) \right] + \omega_i Q_\phi(x,t) \frac{\mathrm{d}t}{\tau_0}, \end{aligned} \tag{3.52}$$

with the equilibrium function $g_i(x,t)$ defined by:

$$g_i^{(0)}(x,t) = \omega_i \left(\phi(x,t) - \frac{1}{c_s^2} e_i \cdot \mathscr{N} + \frac{\phi(x,t)}{2c_s^2} \sum_{\alpha=x,y,z} \left(e_{i\alpha}^2 - c_s^2 \right) \left(\Gamma_\alpha^2 - 1 \right) \right), \tag{3.53}$$

where $\mathscr{N}(\mathscr{N}_x, \mathscr{N}_y, \mathscr{N}_z)$ is defined as:

$$\mathscr{N} = |\nabla_\Gamma \phi|^2 a_s(\boldsymbol{n}) \left(\Gamma_x \frac{\partial a_s(\boldsymbol{n})}{\partial(\partial_x \phi)}, \Gamma_y \frac{\partial a_s(\boldsymbol{n})}{\partial(\partial_y \phi)}, \Gamma_z \frac{\partial a_s(\boldsymbol{n})}{\partial(\partial_z \phi)} \right)^T. \tag{3.54}$$

The function Q_ϕ is the source term which is defined as follows:

$$Q_\phi = \omega_i \left(\frac{(\phi - \phi^3) + \lambda B(\mathbf{n}) U (1-\phi^2)^2}{\tau_0} \right), \tag{3.55}$$

where $B(\mathbf{n})$ is the same as in Eq. (2.25). The relaxation coefficient $\eta_\phi(x,t)$ is defined as:

$$\eta_\phi(x,t) = \frac{1}{c_s^2} \frac{W_0^2}{\tau_0} \frac{\delta t}{\delta x^2} a_s^2(\mathbf{n}) + \frac{1}{2}, \tag{3.56}$$

3.2.4 LB method for Navier-Stokes equations

This chapter focuses on the numerical resolution of the Boltzmann method on the lattice stencil model described in Sec. 3.1.2. LBM is a very attractive method to simulate fluid dynamics problems. The target system of equations describing the flow field behavior (i.e. incompressible NS-continuity equations) are modeled using the classical isothermal LB formulation consisting of

the now-famous stream-collide operators:

$$f_i(\boldsymbol{x}+\boldsymbol{c}_i\delta t, t+\delta t) - f_i(\boldsymbol{x},t) = \delta t\Omega_i(\boldsymbol{x},t) + \delta t F_i, \tag{3.57}$$

where F_i is the external force contribution following Guo's scheme [68]:

$$F_i = \left(1-\frac{\delta t}{2\tau}\right) w_i \left(\frac{\boldsymbol{c}_i-\boldsymbol{u}}{c_s^2} + \frac{\boldsymbol{c}_i\cdot\boldsymbol{u}}{c_s^4}\boldsymbol{c}_i\right)\cdot \boldsymbol{F}_d \delta t. \tag{3.58}$$

Here, the external force $\boldsymbol{F}_d$ modeling interaction with the solid phase is given as [16, 26]:

$$\boldsymbol{F}_d = -\frac{h\eta_f(1+\phi)^2(1-\phi)\boldsymbol{u}}{4W_0^2} \tag{3.59}$$

where h is a dimensionless constant, here $h = 2.757$. Due to the absence of fluid velocity in the crystal growth, the fluid velocity $\boldsymbol{u}$ is updated as [17]:

$$\boldsymbol{u}^* = \frac{(1-\phi)}{2}\boldsymbol{u}, \tag{3.60}$$

where the updated fluid velocity $\boldsymbol{u}^*$ is taken into the momentum equation. The above friction term acts as a distributed momentum sink that gradually forces the liquid velocity to zero as $\phi \to 1$. The collision operator Ω_i follows the linear Bhatnagar-Gross-Krook approximation:

$$\Omega_i = \frac{1}{\tau_f}\left[f_i^{(eq)} - f_i\right], \tag{3.61}$$

where $f_i^{(eq)}$ is the discrete isothermal EDF defined as:

$$f_i^{(eq)} = \omega_i\rho\left[1+\frac{\boldsymbol{c}_i\cdot\boldsymbol{u}}{c_s^2} + \frac{(\boldsymbol{c}_i\cdot\boldsymbol{u})^2}{2c_s^4} - \frac{|\boldsymbol{u}|^2}{2c_s^2}\right], \tag{3.62}$$

where ρ represents the density of the fluid and c_s denotes the lattice sound speed corresponding to the speed of sound at the stencil reference temperature [69]. The relaxation time τ_f is tied to the fluid kinematic viscosity as:

$$\tau_f = \frac{\nu}{c_s^2} + \frac{\delta t}{2}. \tag{3.63}$$

It must be noted that conserved variables, i.e. density and momentum are defined as moments of the discrete distribution function:

$$\rho = \sum_i f_i, \tag{3.64}$$

$$\rho \boldsymbol{u} = \frac{\delta t}{2} \boldsymbol{F}_i + \sum_i \boldsymbol{c}_i f_i. \tag{3.65}$$

In order to implement the numerical schemes discussed above, the computational algorithm shown in Fig. 3.3 is used.

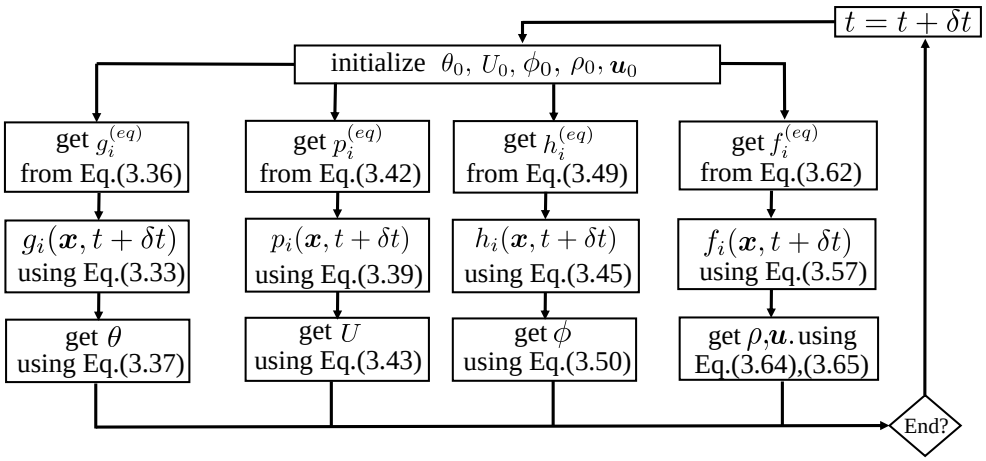

Figure 3.3: Overall structure of the proposed simulation scheme.

Eqs. (2.16)-(2.18) represent the mathematical model and the numerical method based on the LBM was described for each equation of the model in this chapter. The LBE serves as a spatiotemporal evolution equation for a discrete function—the distribution function of particles—defined over a lattice. The choice of the lattice structure dictates the number of streaming directions for the distribution function. Once the LBE was defined, the algorithm was summarized in three main operations applied on this distribution function: (1) a lattice-moving step; (2) a collision step facilitating relaxation towards equilibrium with a designated relaxation rate; (3) the last stage involves updating the physical variable—such as the dimensionless temperature or the phase field—by computing its zeroth-order moment.

3.3 Summary

In this chapter, the LBM was introduced, including its history, formulation, advantages. Moreover, the SRT-LBM model with different lattice stencil structures was explained. Then, the classical LB scheme for the ADE, which is applied in the PF model, was fully developed for the crystal growth. To do so, LBM was used for temperature, supersaturation and PF equations, respectively, due to its numerous advantages. In particular, linear convective term, locality of calculations and high parallel efficiency are fascinating. In our simulations, we only deal with incompressible regimes

of low Mach number and small temperature variations. Thus, standard SRT-LBM is satisfactory and is utilized. Next chapter will go deeper into the introduction of the validation of the PF model combined with LBM.

Chapter 4

Validations in 2D

Contents

This chapter will introduce the validation of PF model, which were conducted during the method development process. The process of validation is important and is divided into several parts here. Firstly, the benchmark cases are made for anisotropy ADE. Then, we check the influence of the grid anisotropy on simulated crystal shapes; the directional derivatives method in LB scheme can compute accurately the space gradient of the order parameter ϕ. Following a comprehensive evaluation of different isotropic orders to analyze grid anisotropy, the selection of the fourth isotropic order has been uniformly implemented for all simulations presented in this thesis. In Sec. 4.3, the tip velocity of an octahedron shape crystal is compared to the numerical results from Cartalade et al. [67]. Then, the influences of the physical parameters, for example, capillary length d_0, diffusion coefficient D on the tip velocity and tip radius are analyzed in detail. The no-slip approaches for calculating the fluid/solid interface forces are illustrated in Sec. 4.5. The tip velocity of the crystal in each direction is presented. At last, in Sec. 4.6, the hydrodynamic effect on a single crystal is considered. In addition, it is important to mention that the lattice structure model employed for all simulations in this paper adheres to D2Q9 in two dimensions and D3Q19 in three dimensions.

4.1 Benchmark cases for anisotropy ADE

The algorithm for anisotropy ADE was introduced in Sec. 3.1.3. The objective of this section is to compare the ϕ distribution of different diffusion coefficients in x-axis and y-axis coordinates with FD method in Eq. (3.22).

In order to avoid the treatment of special boundary conditions, we choose periodic boundaries in 2D domain within $[-1,1]\times[-1,1]$ [m] and the results are compared at time $t = 10$ s. The initial width of the Gaussian hill is $\sigma_0 = 0.01$[m]. For the diffusion-dominated regimes (Pe=0), we choose the velocity $u = 0$. Three diffusion tensors are tested, from left to right:

$$\mathbf{D} = \left(\begin{bmatrix} 1 & 0 \\ 0 & 1 \end{bmatrix}, \begin{bmatrix} 1 & 0 \\ 0 & 2 \end{bmatrix}, \begin{bmatrix} 1 & 1 \\ 1 & 2 \end{bmatrix} \right) \times 10^{-3}\mathrm{m}^2/\mathrm{s} \tag{4.1}$$

The values are given for $\delta x = 0.01$m corresponding to the number of nodes $N = 201 \times 201$.

Pure difussion The simulation in LBM as the D2Q9 model with $\tau = 1$ and the velocity vector $\boldsymbol{u} = 0$. In Fig. 4.1, the results derived from the implementation of pure anisotropy diffusion using the LBM (in blue) exhibit a commendable agreement with the findings obtained through FD (in black) and the analytical solution (in red) presented in Eq. (3.31): the colors are overlaid:

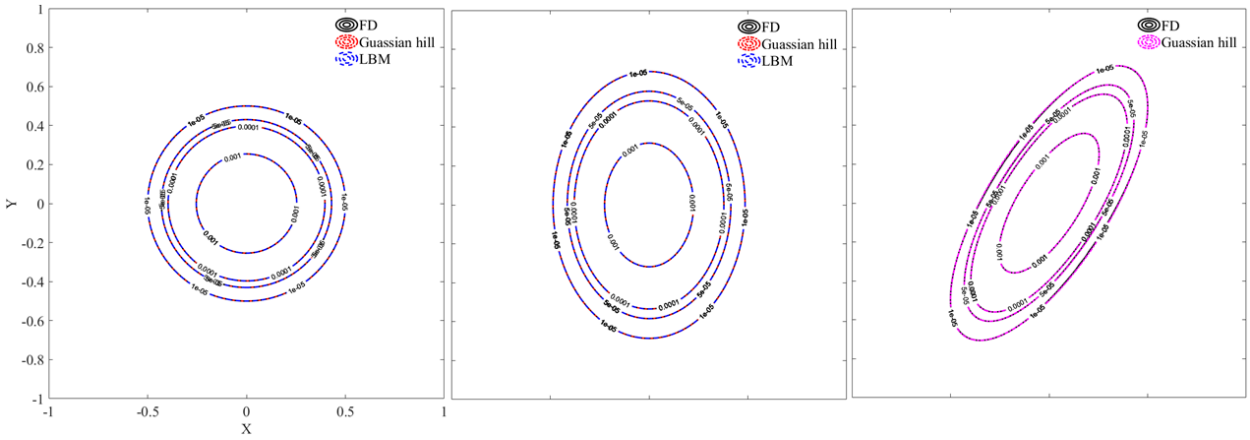

Figure 4.1: Contours of the FD, Gaussian hill (analytical solution) and LBM results at time 10 s without velocity for the three diffusion tensors. Values of contours of the scalar variable are 10^{-5}, 5×10^{-5}, 10^{-4} and 10^{-3} (from outside to inside).

Advection and difussion The simulation in LBM as the D2Q9 model with $\tau = 1$ and the velocity vector $\mathbf{u} = (0.01, 0.01)\mathrm{m/s}$. In Fig. 4.2, anisotropy diffusion incorporating the advection term shows perfect agreement for LBM, FD, and analytical solution from Gaussian hill.

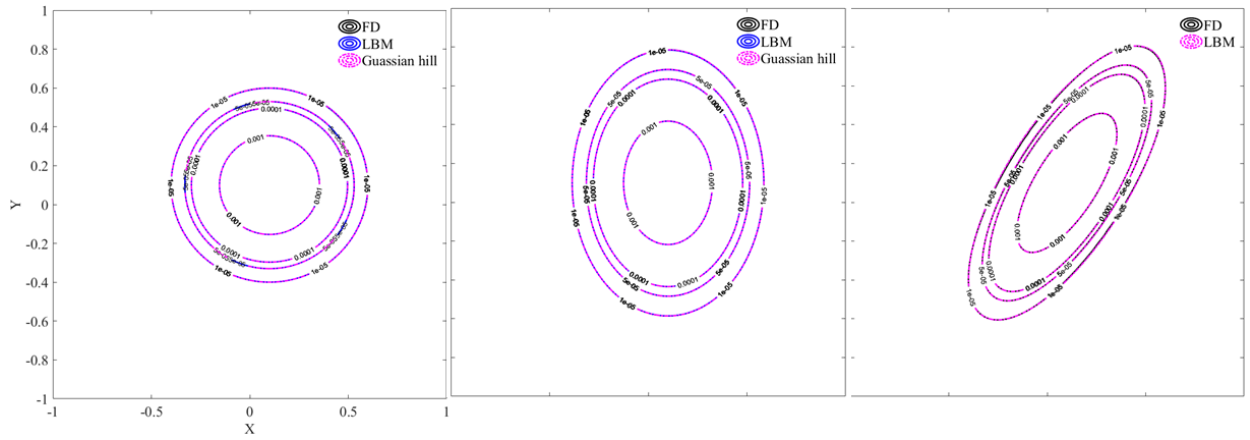

Figure 4.2: Contours of the FD, Gaussian hill (analytical solution) and LBM results at time 10 s with velocity $\mathbf{u} = (0.01, 0.01)\mathrm{m/s}$ for the three diffusion tensors. Values of contours of the scalar variable are 10^{-5}, 5×10^{-5}, 10^{-4} and 10^{-3} (from outside to inside).

Table 4.1 presents various resolutions employed for the convergence analysis of the anisotropic ADE. In Fig. 4.3, the slope of the dashed line is calculated to be -1.9383. Consequently, for the LBM, the observed convergence order is approximately second order, as expected from theory.

Table 4.1: Physical parameters of simulations

Resolution	σ_0	time step	Error
32×32	0.625	5×10^2	3×10^{-2}
64×64	1.25	2×10^3	7×10^{-3}
128×128	2.5	5.8×10^3	1.5×10^{-3}
256×256	5	2.28×10^4	4.7×10^{-4}
512×512	10	7.1×10^4	1.4×10^{-4}

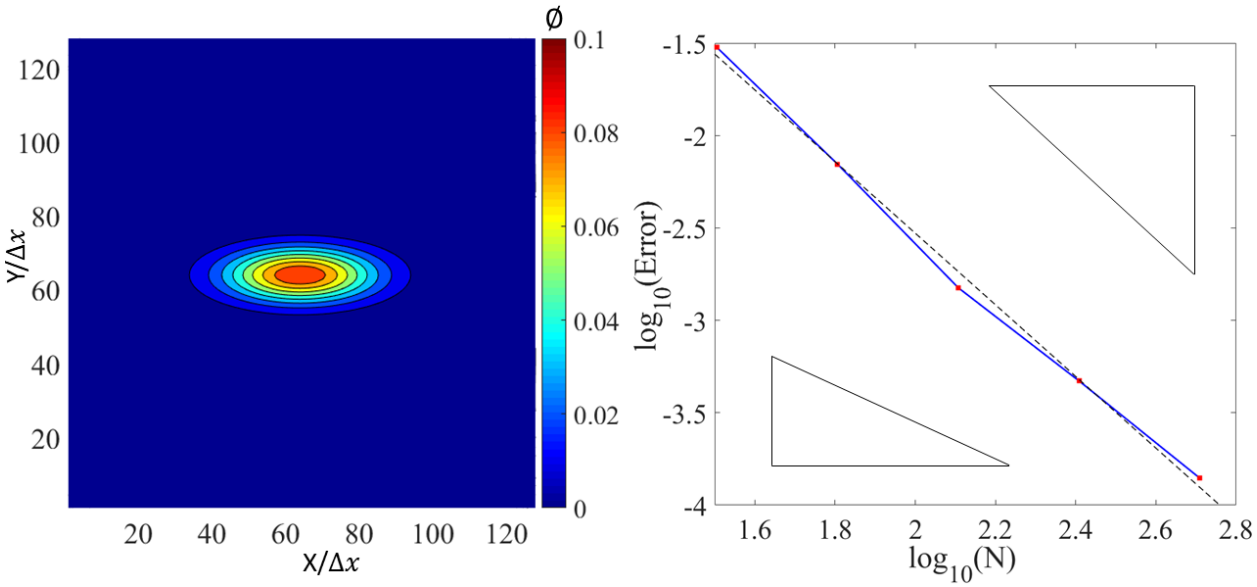

Figure 4.3: Exemplary concentration contour plot with LBM in 128×128 grids at $t = 2000\delta t$ (left). Right: spatial order of convergence for ϕ using LBM compared to exact solution from Eq. (3.32) for different resolutions $N = 32$, 64, 128, 256 and 512, respectively; The slope of the dash line is -1.9383.

4.2 Effect of directional derivatives of gradients in LB scheme

In order to calculate the derivatives of $a_s(\boldsymbol{n})$ with respect to $\partial_x\phi$, $\partial_y\phi$ and $\partial_z\phi$ involved in the second term in Eq. (2.16), different choices are available. Overall, one can either evaluate the gradient using classical finite-difference approximations, e.g. the central difference second-order formulation: $\partial_x\phi \simeq (\phi_{\alpha+1,\beta,\gamma} - \phi_{\alpha-1,\beta,\gamma})/2\delta x$, $\partial_y\phi \simeq (\phi_{\alpha,\beta+1,\gamma} - \phi_{\alpha,\beta-1,\gamma})/2\delta x$ and $\partial_z\phi \simeq (\phi_{\alpha,\beta,\gamma+1} - \phi_{\alpha,\beta,\gamma-1})/2\delta x$, where α, β and γ are the indices of the coordinates x, y and z, or the method

based on the directional derivatives with higher-order isotropy [70]. The isotropic finite-difference approximations to the first-order derivative can be computed as:

$$\nabla\phi = \frac{1}{c_s^2}\sum_{i=0}^{q-1} w_i\left(|c_i|^2\right)\phi\left(x+c_i\right)c_i \tag{4.2}$$

where $w_i\left(|c_i|^2\right)$ are the weights associated to each layer of neighboring nodes maximizing isotropy [71]. These weights are summarized in Table 4.2. The normal vector is $\boldsymbol{n} = \nabla\phi/|\nabla\phi|$. Given the importance of this directional derivative in the growth dynamics of the solid phase, the choice of the approximation will be briefly discussed here.

Table 4.2: Weights for 4th, 6th and 8th order isotropic tensors in two dimensions [71, 72]

Tensor	$w(1)$	$w(2)$	$w(3)$	$w(4)$	$w(5)$	$w(6)$	$w(7)$	$w(8)$
E4	1/3	1/12	-	-	-	-	-	-
E6	4/15	1/10	-	1/120	-	-	-	-
E8	4/21	4/45	-	1/60	2/315	-	-	1/5040

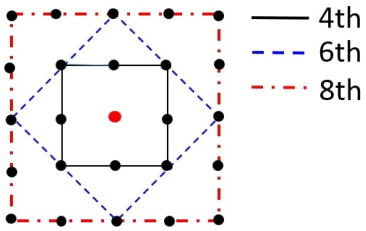

Figure 4.4: Grid points used to identify the set of velocity fields for a 2D case [71, 72]. In combination with the weights reported in Table 4.2, different orders of approximation can be achieved regarding the degree of isotropy: fourth order [up to $\omega(2)$], sixth order [up to $\omega(4)$], eighth order [up to $\omega(8)$].

To that end we consider a generic growing crystal with hexagonal symmetry driven by the temperature field. In non-dimensional unit, the domain is a box of [8, 8], $\delta x = \delta y = 0.01$ and $\delta t = 1.5\times10^{-5}$. $\tau_0 = 1.5625\times10^{-4}$, $W_0 = 0.0125$, $\kappa = 1$, the undercooling is $\Delta = 0.3$, $\lambda = 10$, $\varepsilon_s = 0.05$. The circular seed is initialized at the center of the domain (4, 4) with a radius of $R_s = 0.1$.

Grid resolution analysis At first, grid resolutions between 800×800, 1200×1200 and 1600×1600 are employed. Furthermore, the grid anisotropy is analyzed based on the isotropy order of

the derivatives.

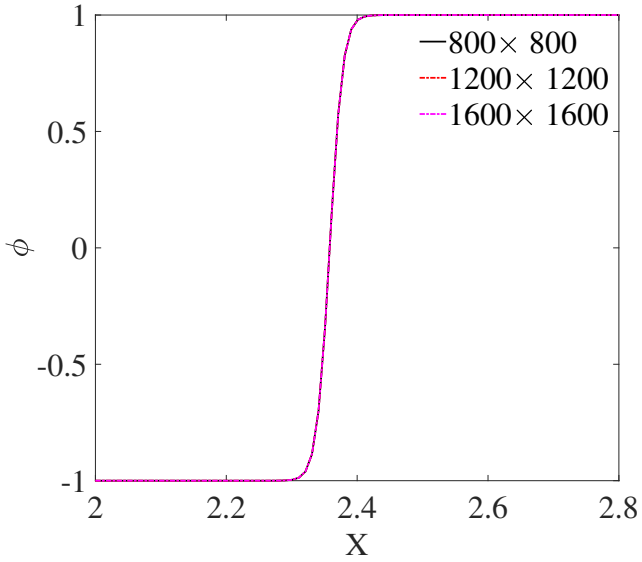

Figure 4.5: Profiles of variable ϕ along direction $\mathbf{n} = (-1,0)$ (horizontal cut from the center of the domain towards the left) obtained with different mesh resolutions of 800×800, 1200×1200 and 1600×1600, respectively.

The l^2 relative error norm is calculated for the ϕ-profiles plotted along the direction $\mathbf{n} = (-1,0)$, as shown in Fig. 4.5. The l^2 norm is defined by:

$$\mathrm{E}_{l^2} = \sqrt{\frac{\sum_i \left(\phi_{low,i} - \phi_{high,i}\right)^2}{\sum_i \phi_{high,i}^2}} \tag{4.3}$$

where ϕ_{low} represents the lower resolution and ϕ_{high} denotes the highest resolution considered during grid error analysis (1600×1600), selected as reference.

Table 4.3: Influence of grid resolution on the error for PF simulations

Resolutions	800×800	1200×1200
E_{l^2}	1.12e-8	7.79e-9

The results shown in Fig. 4.5 and Table 4.3 show that the lowest resolution of 800×800 is already sufficient, all curves in Fig. 4.5 falling on top of each other, with an error of the order of 10^{-8}.

Grid anisotropy analysis To further study the grid anisotropy with different orders of approximation regarding the degree of isotropy, the 4th, 6th and 8th orders in Table 4.2 are used to calculate the hexagonal crystal growth, respectively. All further simulations in this section employ a domain of size 800×800 due to the grid resolution analysis above. The solid boundaries, corresponding to $\phi = 0$, are shown in Fig. 4.6 using different approximations at $t = 10^5 \delta t$. It can be seen on the zoom that the results obtained with a second-order finite difference method (E2, in green) do not match well with the reference. As a function of their orientation relative to the main axes, the dendrites are slightly different from each other. When the gradients are calculated with higher order isotropic formulations these non-physical anisotropic effects are considerably reduced.

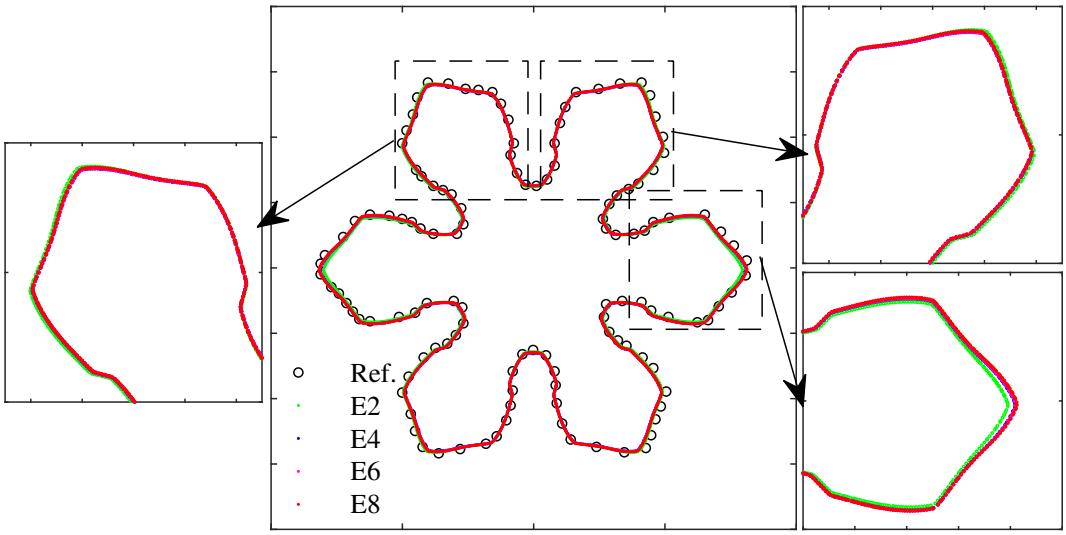

Figure 4.6: Iso-contours of $\phi = 0$ at time $t = 1 \times 10^5 \delta t$. Black circles are reference results from [1].

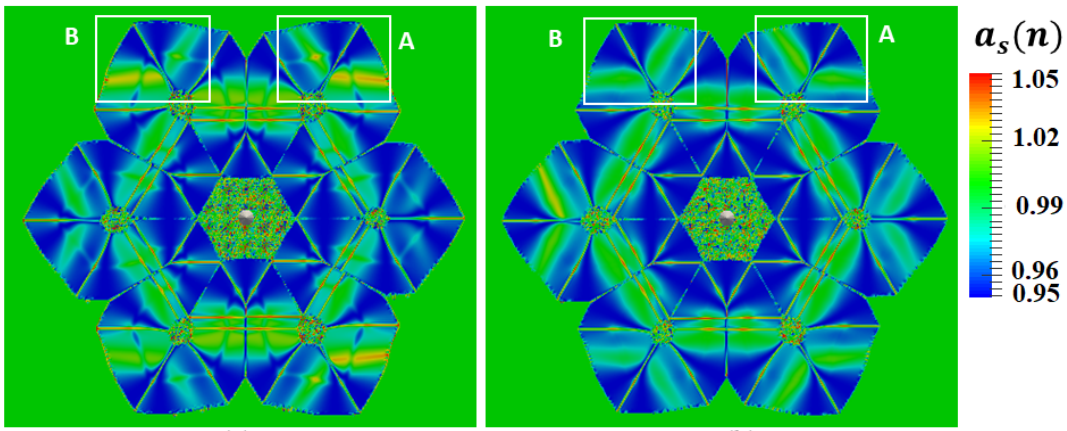

Figure 4.7: Anisotropy function $a_s(\boldsymbol{n})$ at time $t = 1 \times 10^5 \delta t$. (a) With isotropic order E2; (b) with isotropic order E4;

In Fig. 4.7, the anisotropy function $a_s(\boldsymbol{n})$ is plotted as a function of position with two different isotropic orders, E2 and E4. The origin of the differences for iso-contour values of $\phi = 0$ can be understood. On the left hand side (LHS) in the box A and B, the patterns are not symmetric with the isotropic order E2. But on the right hand side (RHS), the patterns in boxes A and B are identical with isotropic order E4. By accounting for the diagonals of the lattice in the gradient calculation, $a_s(\boldsymbol{n})$ achieves greater accuracy and complete symmetry, showing the symmetry of order E4.

In order to quantify the grid anisotropy errors, the l^2 relative error norm is calculated with two ϕ-profiles plotted along two directions $\mathbf{n}_a = (1,0)$ and $\mathbf{n}_b = (1/2, -\sqrt{3}/2)$. The l^2 norm is again defined by:

$$\mathrm{E}_{l^2} = \sqrt{\frac{\sum_j^{N_j} \left(\phi_{a,j} - \phi_{b,j}\right)^2}{\sum_j^{N_j} \phi_{a,j}^2}} \tag{4.4}$$

where ϕ_a and ϕ_b are the PFs collected along the directions $\mathbf{n}_a$ and $\mathbf{n}_b$ respectively.

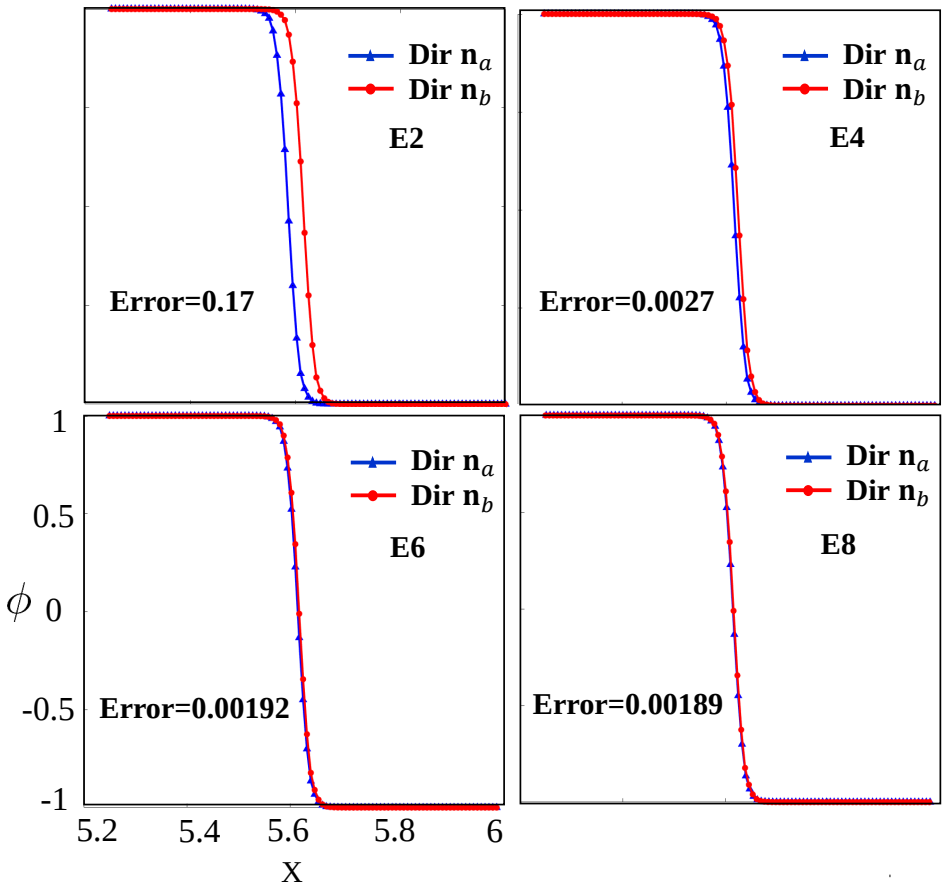

Figure 4.8: Comparing ϕ profiles along directions $n_0 = (1,0)$ and $n_b = (1/2, -\sqrt{3}/2)$. (a) With isotropy order E2 the relative error (l^2-norm) is 0.17; (b) with E4 it is 0.0027; (c) with E6 it is 0.00192; (d) with E8 it is 0.00189.

The l^2 relative error for the central finite difference method (E2) is $E_{l^2}^{E2} = 1.7 \times 10^{-1}$, while the relative error for the directional derivatives method is only $E_{l^2}^{E4} = 2.7 \times 10^{-3}$ (see also Fig. 4.8). This shows that the error is decreased by two orders of magnitude when using the E4 method in Eq. (4.2). Considering these results a minimum isotropy of order 4, i.e., the E4 stencil, appears necessary for the proper simulation of a six-tip crystal.

Following a comprehensive evaluation of different isotropic orders to analyze grid anisotropy, the selection of the fourth isotropic order E4 is implemented for all further simulations presented in this thesis.

4.3 Validation for the tip velocity

To validate the model and subsequent implementation, we use the generic system with four-fold symmetry studied in [1, 67]. To provide both qualitative and quantitative proof, we compare the shape of the dendrites and the evolution of the tip velocity.

Initially, a circular seed of radius $R_s = 10\delta x$ is placed at the centre of the square domain. In non-dimensional units, the interface thickness W_0 and the characteristic time τ_0 are $W_0 = \tau_0 = 1$. The grid-size is set to $\delta x/W_0 = 0.4$ [10] while the time-step size is $\delta t = 0.008$. The capillary length d_0 and the kinetic coefficient β are given by [10]: $d_0 = a_1 W_0/\lambda$ and $\beta = a_1(\tau_0/\lambda W_0 - a_2 W_0/\kappa)$ where $a_1 = 0.8839$ and $a_2 = 0.6267$. In this benchmark, we choose the parameters $\kappa = 4$, $\lambda = \frac{\tau_0 \kappa}{a_2 W_0^2} = 6.3826$ with $\beta = 0$. The anisotropic strength is $\varepsilon_s = 0.05$. The initial supersaturations are $U_0 = 0.3$ and 0.55. For $U_0 = 0.3$, we use a grid of size 1000^2 nodes while for the latter the domain size is reduced to 500^2 nodes. The growth velocity of the crystal tips is made dimensionless as $\tilde{\boldsymbol{V}}_{\boldsymbol{p}} = \boldsymbol{V}_{\boldsymbol{p}} d_0/D$. The non-dimensional position $\tilde{\boldsymbol{x}}$ is defined as $\tilde{\boldsymbol{x}} = \boldsymbol{x}/\delta x$ and the reduced time T as $T = t/\tau_0$.

The obtained results are shown in Fig. 4.9. As shown there, the data obtained from the present work closely follows those reported in [67]. On the left, the tetrahedral crystal occurs as the number of the crystal tips in the anisotropy function is set as $q = 4$. The iso-contour of phase value $\phi = 0$ (red) matches well with the reference [67] (black dash line). On the right, the velocity of growing tips starts to decrease until reaching a minimum value before approaching a steady value. Initially, when the crystal growth process begins, the concentration gradient between the solidifying crystal and the surrounding fluid can be significant. As the crystal forms, it absorbs the molecular from the surroundings, causing a local decrease in concentration near the solid/liquid interface.

We have demonstrated in this comparison the applicability of our results in two dimensions by performing quantitative tests evaluating dendrite velocity and shape selection. Simulations yield tip velocities which are very accurate. This insight into the phase-field method should find a wide range of applications in solidification as well as other related interfacial pattern formation

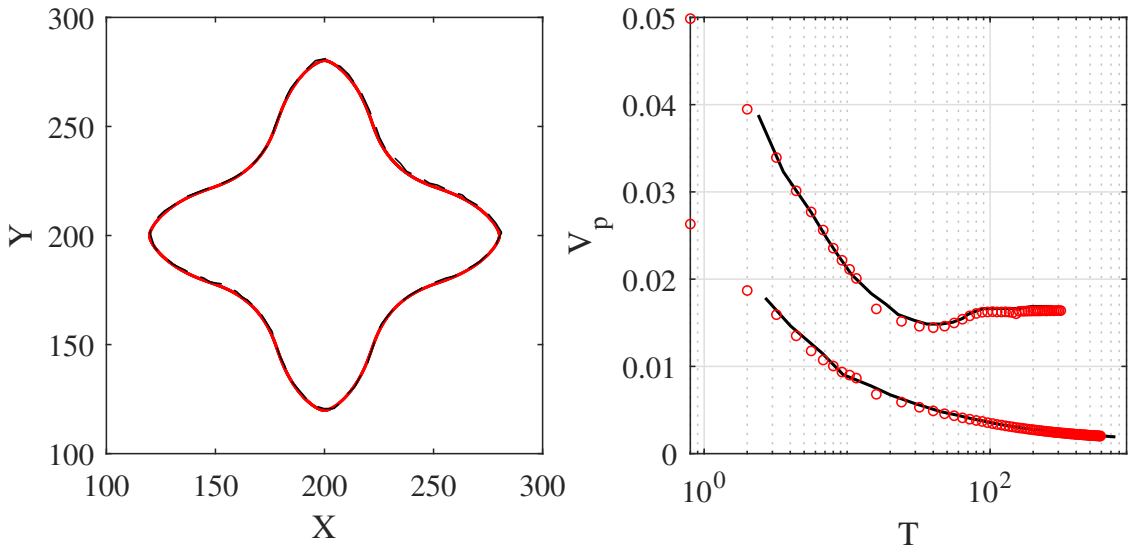

Figure 4.9: (left) $\phi = 0$ iso-contours for $U_0 = 0.3$ at $t = 1.3 \times 10^5 \delta t$. Red lines and dots are from the present study while black lines are from [67]. (right) Dimensionless tip velocity V_p as a function of time (in units of τ_0) for (lower curve/symbols) $U_0 = 0.3$ and (upper curve/symbols) $U_0 = 0.55$. The red circles are from the present study, while plain black lines are extracted from [67].

phenomena, particularly those governed by analogous free-boundary problems.

4.4 Analysis of the physical parameters

After the validation case of the four-fold crystal, here the physical parameters such as anisotropy strength ε_s in the anisotropy function $a_s(\boldsymbol{n})$, capillary length d_0, diffusion coefficient D, initial supersaturation U_0 and the tip radius ρ_{tip} are analyzed in detail.

4.4.1 Anisotropy strength

In this section, we conduct an analysis of the anisotropy strength ε_s. The parameters are set as follows: $W_0 = 0.5$, $\tau_0 = 0.25$, $R_s = 4$, $\lambda = 3$, $D = 1.8801$ and $U_0 = 0.7$. The spatial unit is $\delta x = 0.4$ and the temporal unit is $\delta t = 0.05$. The anisotropy strength ε_s within anisotropy function is varied, with values set at 0.05, 0.1 and 0.2, respectively.

Fig. 4.10 illustrates the contour of the phase value $\phi = 0$ for the crystal, for different values of the anisotropy strength ε_s from 0.05 to 0.2. As the anisotropy strength ε_s, increases, the dendrites exhibit greater instability, particularly evident in the primary branches.

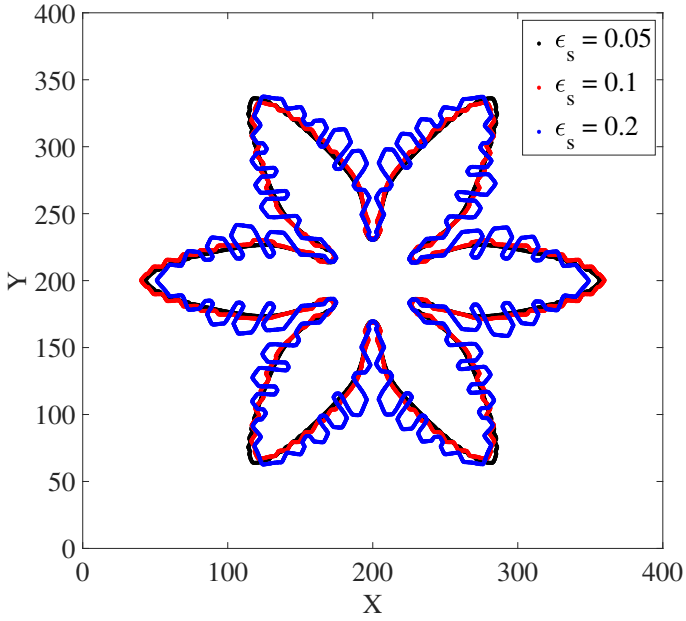

Figure 4.10: The contour of the phase value $\phi = 0$ with $\varepsilon_s = 0.05$ (blue line); $\varepsilon_s = 0.1$ (red line) and $\varepsilon_s = 0.2$ (black line) at time t=250.

Regularized anisotropy function Crystalline structures often manifest as faceted geometries characterized by rounded faces exhibiting a significant radius of curvature. This distinctive morphology can be attributed to the influence of surface tension anisotropy, encapsulated within the function $a_s(\boldsymbol{n})$, particularly pronounced along energy-rich directions that induce instability in the equilibrium shape of the crystal [73]. The degree of the anisotropy is set by the constant ε_s on the interval [0,1). For relatively small anisotropy the equilibrium shape is smooth, while heightened ε_s values lead to the emergence of corners and edges, causing the exclusion of certain high tension orientations from the crystal configuration. Consequently, under a sufficiently strong anisotropy strength ε_s, specific orientations are notably absent from equilibrium shapes, resulting in a discontinuous variation in the surface normal along the interface. The absence of these orientations becomes evident as the reciprocal $a_s(\theta)$-plot shows a pronounced concavity [74].

In the realm of two-dimensional crystal dynamics, the identification of an unstable crystal orientation is contingent upon the manifestation of a negative stiffness, where the criterion is expressed as $a_s(\theta) + \partial^2_{\theta\theta} a_s(\theta) < 0$. The surface tension anisotropy function, delineated in Sec. 2.4, is denoted by $a_s(\theta)$, with the selected form being $a_s(\theta) = 1 + \varepsilon_s \cos(6\theta)$, featuring a distinctive six-fold symmetry. Notably, for values exceeding $\varepsilon_s^m > 1/35$, the spectrum of absent crystal orientations undergoes amplification. Delving into the geometric intricacies associated with the concave segment of the reciprocal $a_s(\theta)$-plot, the corner angle of equilibrium shapes adheres to

the following conditions: $\partial_\theta[\cos(\theta)/a_s(\theta)]|_{\theta=\theta^m} = 0$.

We propose a regularized anisotropy function, $\tilde{a}_s(\theta)$, formulated through the utilization of a common tangent to render convexity to the $1/a_s(\theta)$ plot. Leveraging the rotational periodicity inherent in $a_s(\theta)$, we restrict the procedure to $\theta \in [-\pi/6, \pi/6]$.

$$\tilde{a}_s(\theta) = \begin{cases} a_s(\theta), & \theta^m \leq |\theta| < \pi/6, \\ \frac{a_s(\theta_m)\cos\theta}{\cos(\theta_m)}, & |\theta| < \theta^m. \end{cases} \tag{4.5}$$

Given the aforementioned equation, aimed at regularization of absent orientations in two dimensions, we present the reciprocal $a_s(\theta)$-plot for $\varepsilon_s = 0.2$ in Fig. 4.11. The application of the regularized anisotropy function is specifically employed within the concave angle range. Notably, the resultant 2D polar plot exhibits a regularized form that aligns seamlessly with the original 2D polar plot, where positive curvature was inherent prior to the regularization procedure.

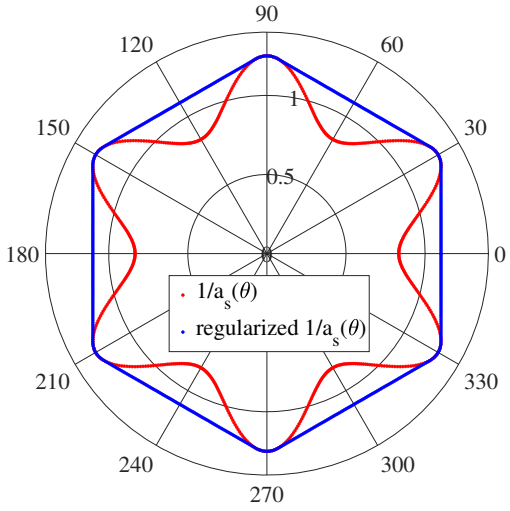

Figure 4.11: Inverse plot of the anisotropy function $a_s(\theta) = 1 + \varepsilon_s \cos(6\theta)$ for $\varepsilon_s = 0.2$. The red line represents the $1/a_s(\theta)$ and the blue line is the tangent construction to the $1/a_s(\theta)$.

The simulation results for a hexagonal crystal in two dimensions, both with and without the incorporation of a regularized anisotropy function for anisotropy strength $\varepsilon_s = 0.2$, are depicted in Fig. 4.12. Notably, under conditions of sufficiently large anisotropy ($\varepsilon_s = 0.2 > \varepsilon_s^m = 1/35$), the manifestation of missing orientations is evident in the simulation employing the regularized anisotropy function, denoted by the blue lines.

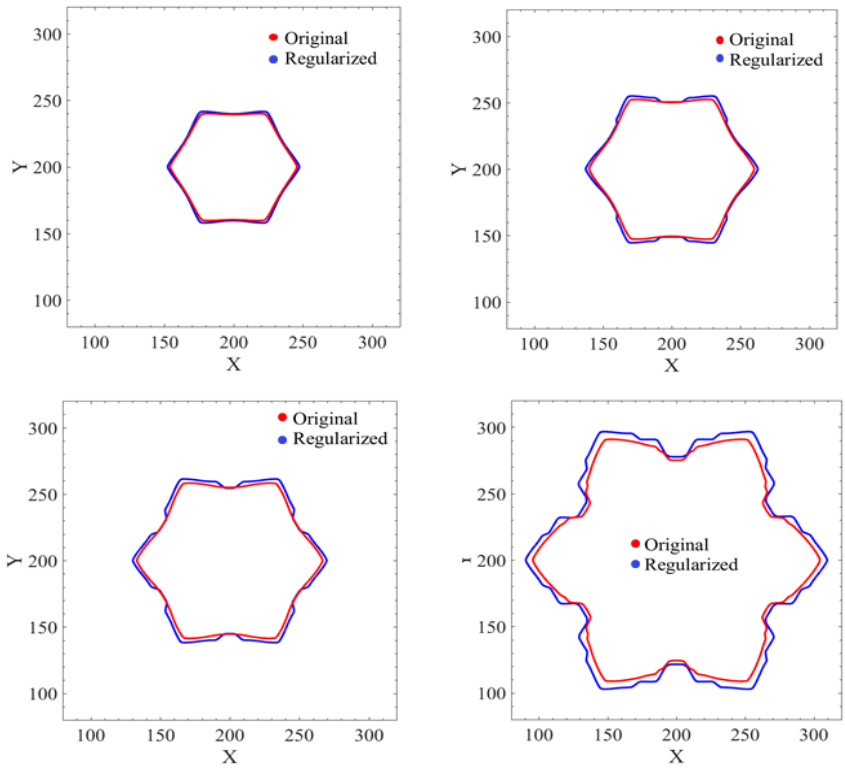

Figure 4.12: The iso-value of phase field $\phi = 0$ at anisotropy strength $\varepsilon_s = 0.2$ for the original $a_s(\theta)$ and regularized anisotropy function $\tilde{a_s}(\theta)$ at different times.

4.4.2 Capillary length

The domain is a square discretized with meshes of size δx. The initial seed is a diffuse circle of radius $R_s = 8\delta x$. The nucleus is initialized as a diffuse sphere: $\phi(\boldsymbol{x},0) = \tanh\left[(R_s - d_s)/\sqrt{2}W_0\right]$, with d_s the distance defined by $d_s = [(x-x_s)^2 + (y-y_s)^2 + (z-z_s)^2]^{1/2}$ and $\boldsymbol{x}_s = (x_s, y_s, z_s)^T$ is the position of its center. With this intial condition, $\phi = +1$ inside the sphere (solid) and $\phi = -1$ outside (liquid). All cases in Table 4.4 are performed for fixed values of $\varepsilon_s = 0.05$, $W_0 = 1$, $\tau_0 = 1$ and $U_0 = 0.55$. Three cases are performed for different values of capillary length d_0 by varying diffusion coefficient D. Hence the coupling strength λ is obtained by the relationship: $D = a_2\lambda W_0^2/\tau_0$ and $d_0 = a_1 W_0/\lambda$ as the interface kinetic coefficient $\beta = 0$, with constant coefficient $a_1 \approx 0.8839$ and $a_2 \approx 0.6267$ (see chapter 2 for details). In order to achieve fully developed tips of the crystal, the grid is set to 2000×2000. The results are shown in Table 4.4.

To gain further insights into the data presented in Table 4.4, three values of the capillary length d_0 have been employed to elucidate the variations in the dimensionless tip velocity and tip radius. The dimensionless tip velocity, denoted as $\tilde{V}_{tip}$, has been appropriately rescaled by $\tilde{V}_{tip} = d_0\tilde{V}_{tip}/D$, and its behavior has been compared against the analytical solution derived from the Green's func-

Table 4.4: Comparison of steady-state tip velocities calculated by PF simulations ($\tilde{V}_{tip} = d_0 V_{tip}/D$) and calculated by Green's function method [9] ($\tilde{V}_{tip}^{GF} = d_0 V_{tip}^{GF}/\kappa$).

Cases	d_0/W_0	λ	D	$\tilde{V}_{tip}$	$\tilde{V}_{tip}^{GF}$	Error	$\tilde{\rho}_{tip}$
1	0.277	3.191	2.0	0.0168	0.017	1%	14.8
2	0.185	4.778	3.0	0.0167	0.017	1.7%	17.3
3	0.139	6.359	4.0	0.0165	0.017	3%	20.14

tion (0.017) [9]. Remarkably, the error associated with the dimensionless velocity, $\tilde{V}_{tip}$, remains below 3.1%, indicating the fidelity of the present simulation results. It is noteworthy that the simulation outcomes align closely with the results from Karma and Rappel [9].

The constancy of the dimensionless tip velocity, $\tilde{V}_{tip}$, is evident under the condition where the interface thickness W_0, relaxation time τ_0, anisotropy strength ε_s (maintained at 0.05), and kinetic coefficient β (set to 0) remain unchanged. It highlights the robustness of the model under specific parameter configurations.

However, an intriguing observation arises when examining the tip velocity V_{tip} in units of W_0/τ_0: it demonstrates an upward trend in correlation with the reduction of the capillary length d_0, as illustrated in Fig. 4.13. This phenomenon merits further attention and investigation, as it suggests a nuanced relationship between the capillary length and the tip velocity, potentially shedding light on important physical insights.

On the left of Fig. 4.14, the dendrite tip's growth is illustrated under varying capillary lengths (d_0). Specifically, the dendrite tip marked with the green dot ($d_0/W_0 = 0.139$) is the thinnest, while the dendrite tip with the blue dot ($d_0/W_0 = 0.277$) appears thicker. Notably, as the capillary length d_0 increases, the diffusion coefficient D decreases. This relationship indicates that a smaller value of the diffusion coefficient D corresponds to a thicker dendrite tip.

On the right, the three small boxes provide a detailed view of the process for calculating the tip radius ρ_{tip} (black circle). Initially, the region corresponding to the dendrite tip is identified. Subsequently, a circle with radius ρ_{tip} is drawn, and the value of the circle radius is adjusted until it is tangent to the maximum curvature of the dendrite tip. The results illustrate that the tip radius ρ_{tip} decreases as the capillary length d_0 decreases. In other words, the diffusion coefficient D is inversely proportional to the tip radius ρ_{tip} and directly proportional to the tip velocity V_{tip} in units of W_0^2/τ_0. The simulation results with the blue are from case 1, the red from case 2 and the green from case 3 in Table 4.4, respectively.

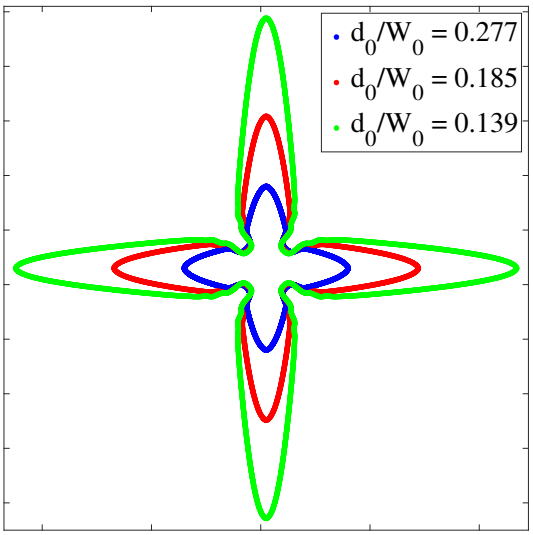

Figure 4.13: Tip shapes of the iso-contour of the phase value $\phi = 0$ corresponding to the following: $d_0/W_0 = 0.277$ (blue), $d_0/W_0 = 0.185$ (red) and $d_0/W_0 = 0.139$ (green) for $t = 1.2 \times 10^5 \delta t$.

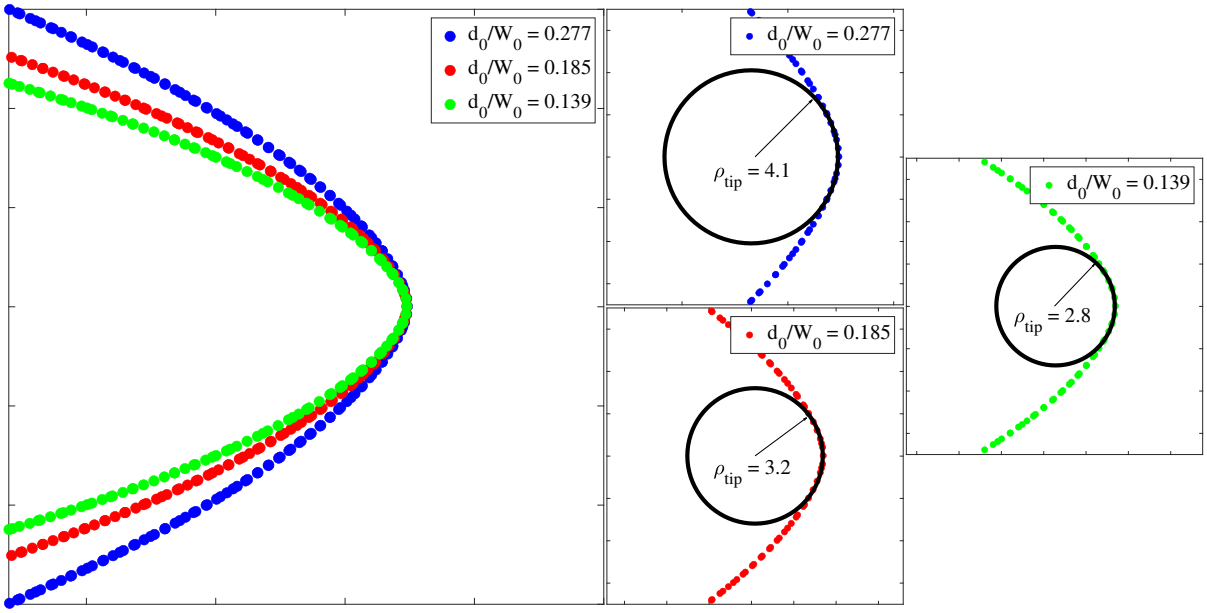

Figure 4.14: Comparison of steady-state tip radius calculated by PF simulations. The three interfaces correspond to the following: $d_0/W_0 = 0.277$ (blue dot point), $d_0/W_0 = 0.185$ (red dot point) and $d_0/W_0 = 0.139$ (green dot point) for $U_0 = 0.55$.

4.4.3 Supersaturation

The supersaturation field was compared with the phase field model given in Sec. 2.3. The space unit is $\delta x = 0.4$, time unit $\delta t = 0.008$, with interface thickness $W_0 = 1$, $\tau_0 = 1$, $\varepsilon_s = 0.05$ and $\lambda = 6.3826$. The mesh is 3000×3000. Here, different initial supersaturation $U_0 = 0.45$, $U_0 = 0.5$ and $U_0 = 0.55$ are set, respectively. The physical parameters are similar to those of Sec. 4.4, except the setting of the initial supersaturation.

For different initial supersaturation values, denoted as U_0 ($U_0 = 0.45$ in black, $U_0 = 0.5$ in red and $U_0 = 0.55$ in blue), the temporal evolution of iso-contour for phase field $\phi = 0$ is depicted in Fig. 4.15.

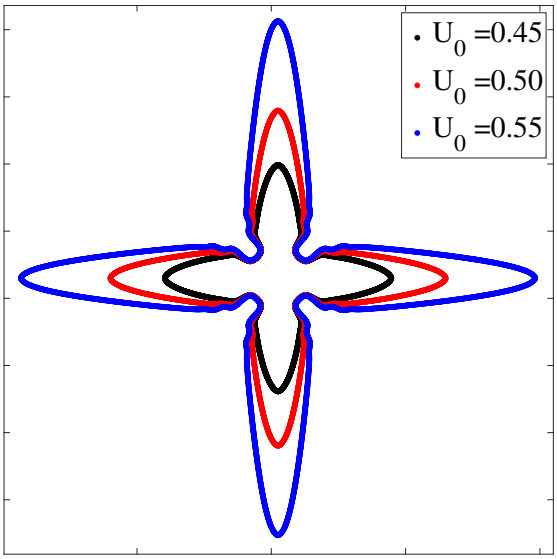

Figure 4.15: Comparison of steady-state tip shapes calculated by PF simulations. The three interfaces correspond to the following: $U_0 = 0.45$ (black), $U_0 = 0.50$ (red) and $U_0 = 0.55$ (blue) for $d_0/W_0 = 0.139$ at $t = 1 \times 10^5 \delta t$.

In Table 4.5, it is evident that, regardless of the chosen definition, whether it is the dimensionless tip velocity $\tilde{V}_{tip}$ given by $\tilde{V}_{tip} = d_0 V_{tip}/D$, or the tip velocity scaled by W_0/τ_0, both exhibit an increasing trend with the elevation of the initial supersaturation U_0, while the tip radius ρ_{tip} is decreasing with increasing supersaturation. The relative error of the tip velocity is calculated, and the analytical solution from the Green's function method is used as a reference.

Table 4.5: Test-cases for PF simulations of dendritic growth with different supersaturation ($\tilde{V}_{tip} = d_0 V_{tip}/D$) and calculated by Green's function method [9] ($\tilde{V}_{tip}^{GF} = d_0 V_{tip}^{GF}/D$).

Cases	U_0	$\tilde{V}_{tip}$	$\tilde{V}_{tip}^{GF}$	Error	$\tilde{\rho}_{tip}$
1	0.45	0.0055	0.00545	0.92%	3.6
2	0.50	0.0099	-	-	2.9
3	0.55	0.0164	0.0170	1%	2.5

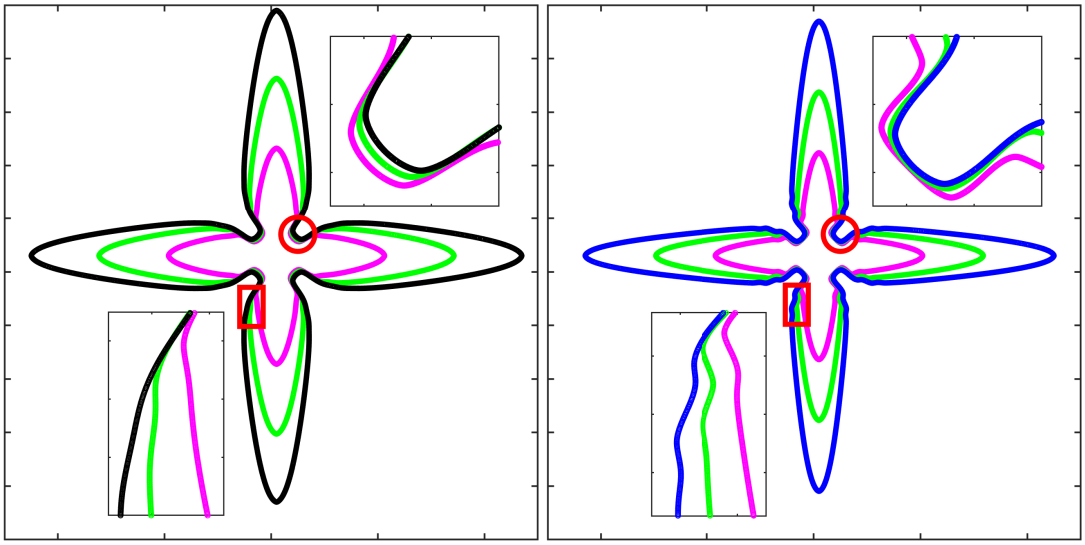

(a) $U_0 = 0.45$ (b) $U_0 = 0.55$

Figure 4.16: The iso-contour of the phase-field $\phi = 0$ with two different initial supersaturation: (a) for $U_0 = 0.45$ at different time $t = 1.25 \times 10^5 \delta t$ (purple), $t = 2.25 \times 10^5 \delta t$ (green), $t = 3.25 \times 10^5 \delta t$ (black); (b) For $U_0 = 0.55$ at different time $t = 0.5 \times 10^5 \delta t$ (purple), $t = 0.8 \times 10^5 \delta t$ (green), $t = 1.15 \times 10^5 \delta t$ (blue);

Fig. 4.16 illustrates the iso-contour of the phase $\phi = 0$ with supersaturation levels $U_0 = 0.45$ (left) and $U_0 = 0.55$ (right) across an increasing time span. In both Fig. 4.16(a) and (b), crystals exhibit growth over time. On the LHS, it is evident from the magnified top-right corner box that the root of the crystal experiences only a slight increase as it progresses towards a steady state. The corresponding root areas on the right show even smaller alterations. This observation provides evidence that the growth rate of the crystal's root is slower with increasing supersaturation. In the bottom-left corner box, which is also magnified in both figures, the dendritic branch appears smooth on the left but becomes more unstable on the right as the crystal progresses toward steady state. This observation leads to the conclusion that dendritic branches become more sensitive with

an increase in supersaturation, and there exists the potential for the development of sub-branches as the supersaturation reaches a certain value.

On the left of Fig. 4.17, the evolution of dendrite tips is shown for varying supersaturation levels, namely $U_0 = 0.45$, $U_0 = 0.5$, and $U_0 = 0.55$, respectively. Notably, the dendrite tip with the green dots ($U_0 = 0.55$) appears the thinnest, while the dendrite tip with the blue dots ($U_0 = 0.45$) is comparatively thicker. This observation suggests that a smaller value of supersaturation U_0 corresponds to a thicker dendrite tip.

On the right, the three small boxes provide a closer look at the measurement of the tip radius ρ_{tip} denoted by the black circle. The procedural details for the tip radius calculation have been derived before. This figure reveals that the tip radius ρ_{tip} is becoming smaller as supersaturation U_0 increases. In other words, the value of the supersaturation U_0 exhibits an inverse relationship with the tip radius ρ_{tip}. It is noteworthy that the simulation results associated with the blue dot correspond to case 1, the red dot to case 2, and the green dot to case 3 in Table 4.5.

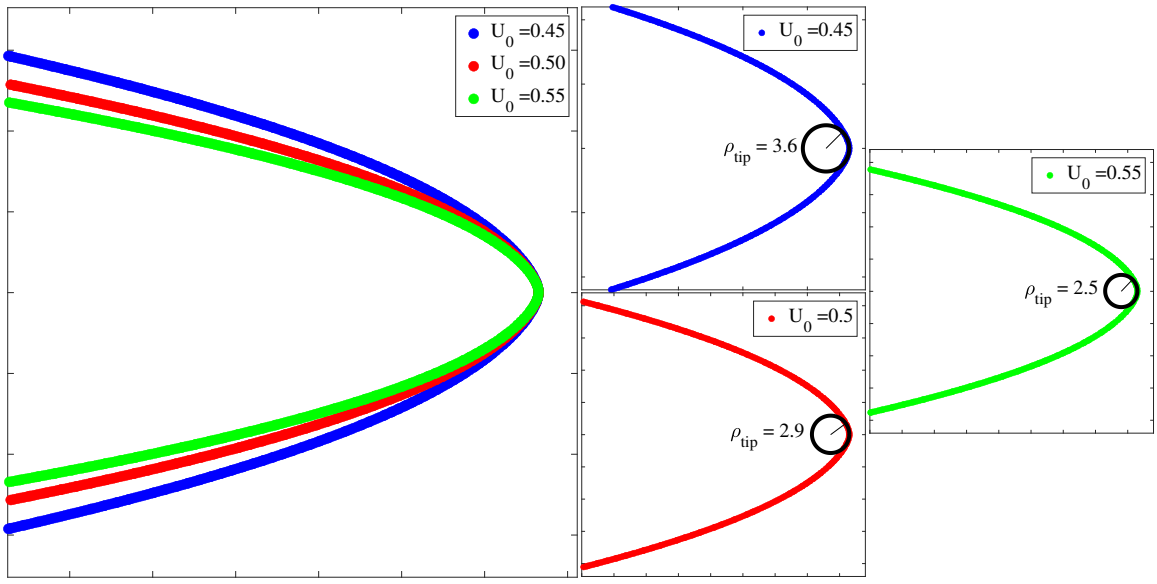

Figure 4.17: Comparison of steady-state tip shapes calculated by PF simulations. The three interfaces correspond to the following: $U_0 = 0.45$ (blue), $U_0 = 0.5$ (red) and $U_0 = 0.55$ (green) for $d_0/W_0 = 0.139$.

4.5 Validation of no-slip approaches

This section delves into the exploration of the no-slip approach within the PF model using the LBM. The no-slip approach for the PF model has been previously investigated by Beckermann

et al. [16]. In their study, Beckermann et al. established the no-slip condition at the fluid-solid interface by introducing drag resistivity within the diffuse interface region. They modeled the interaction between the solid and liquid phases through a distributed momentum sink term within this diffuse interface region. Notably, this drag term was designed to vary linearly in proportion to the relative velocity of the two phases. The calibration of the interfacial drag model focused on scenarios involving plane flow over a stationary solid–liquid interface. Notably, the model demonstrated consistent accuracy, independent of variations in the diffuse interface thickness denoted as W_0. To assess the model's performance, comprehensive testing was conducted against analytical results, particularly within the context of two-dimensional Stokes flow through regularly arranged cylinders. The outcomes of these tests revealed the model's exceptional convergence properties, particularly when dealing with large ratios of diffuse interface thickness W_0 to flow passage width. This suggests the model's robust reliability in situations where the transition region between phases is more pronounced than the dimensions of the flow path.

Building upon the insights provided by Beckermann et al. [16], this section extends the examination of the fluid/solid interface drag model, particularly in the context of test-cases involving steady viscous flow past a circular cylinder. The subsequent analysis involves a comparison with reference methods outlined in Table 4.6, which delineate various approaches for calibrating the no-slip condition at the fluid-solid interface using the LBM.

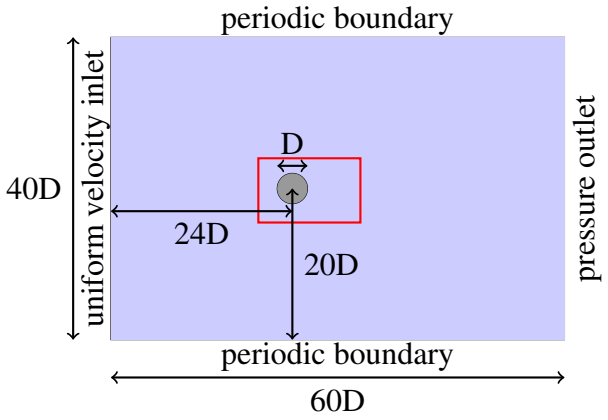

Figure 4.18: Geometry of the flow around a cylinder

The numerical simulation of steady flow around a circular cylinder is carried out with initial fluid density set as $\rho = 1000$ kg/m^3, and initial velocity equal to free stream velocity $\boldsymbol{u}_{in} = 0.05$ m/s. The kinematic viscosity is $\nu_f = 2.5 \times 10^{-4}$ m^2/s. Fig. 4.18 shows a schematic of the considered geometry. As shown in Fig. 4.18, a periodic boundary condition is employed at up and down boundaries, and inlet uniform velocity and outlet pressure boundary condition employed at left and right boundaries. The computational domain is 60D $\times$ 40D; the cylinder is located at (24D,

20D) with diameter D=0.1m; the interface thickness $W_0 = 0.015$m. In this section, we consider a fluid flow with a Reynolds number of 20, defined as Re = $\boldsymbol{u}_\infty D/\nu_f$, with $\boldsymbol{u}_\infty$ the free stream velocity.

Table 4.6: Comparison of recirculation length and drag coefficient for steady flow over a circular cylinder at Re = 20 using different methods.

References	L/D	C_d
Dennis and Chang [75]	1.88	2.045
Fornberg [76]	1.82	2.000
He and Doolen [77]	1.842	2.152
Wang [78]	1.86	2.072
Nieuwstadt [79] (Semi-analytical)	1.786	2.053
Average	1.838	2.064

Table 4.7 shows the mesh sizes, time-step, and corresponding diffusive scaling number CFL and resolutions considered in this simulation. When the flow reaches steady state, there will be a pair of stationary recirculating eddies behind the cylinder for this Reynold number.

Table 4.7: Summary of numerical simulation parameters for Re = 20.

Cases	Resolution	δx [m]	δt [s]	CFL
R1	406×267	0.015	0.0225	0.075
R2	486×320	0.0125	0.015625	0.0625
R3	606×400	0.01	0.01	0.0500
R4	692×457	0.00875	0.00765625	0.0437
R5	806×534	0.0075	0.005625	0.0375
R6	1206×800	0.005	0.0025	0.0258

In Fig. 4.19, the x-direction velocity field and streamlines at the steady state for Re = 20 are depicted. It can be seen in the zoom from the red rectangle in Fig. 4.18 that the velocity behind the cylinder adopts negative values due to the presence of a pair of stationary recirculating eddies positioned in the wake of the cylinder. The application of the present method ensures a distinct

separation between the streamlines and the surface of the cylinder, as depicted in the figure. The encapsulation of streamlines within the boundary of the cylinder is a direct consequence of the rigorous enforcement of the no-slip boundary condition in the present method. This observation underscores the effectiveness of the method in preventing the penetration of streamlines into the cylinder surface.

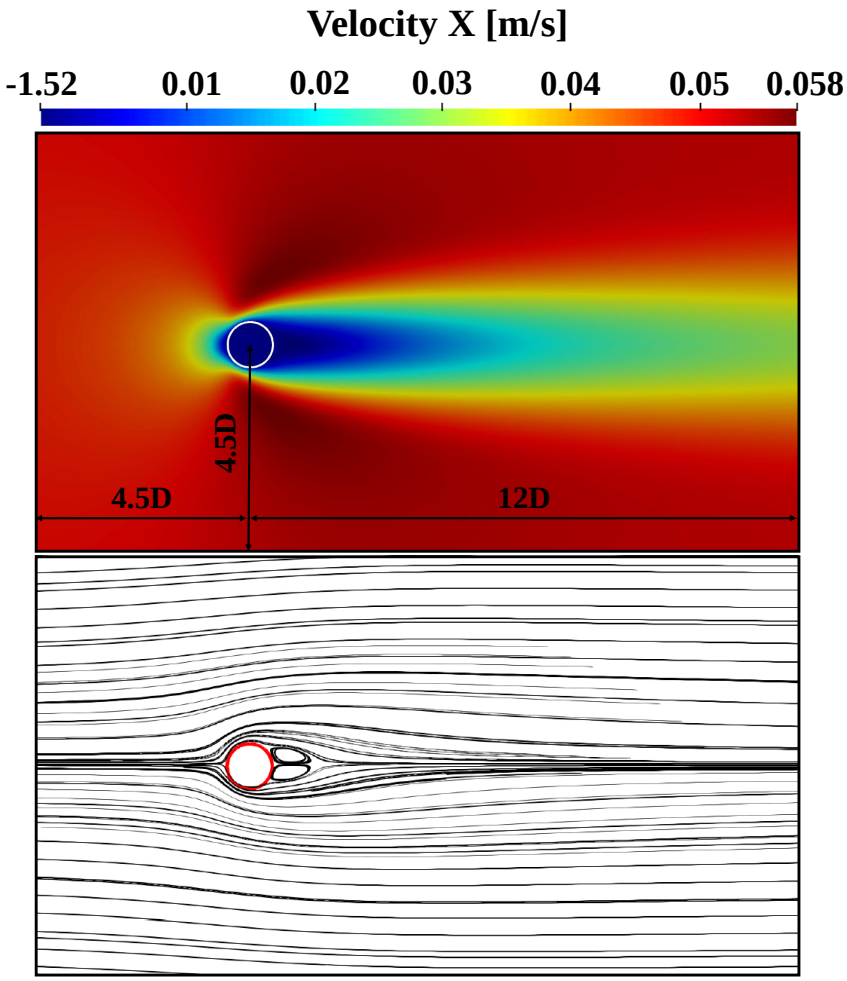

Figure 4.19: Velocity and streamlines for the flow over a circular cylinder in x-axis direction for case R6 in Table 4.7 (It is zoomed from the red rectangle in Fig. 4.18).

The velocity profile along the middle horizontal line is further visualized in Fig. 4.20. This representation serves to illustrate the quantification of the recirculating region's length, denoted as L, within the current simulation results.

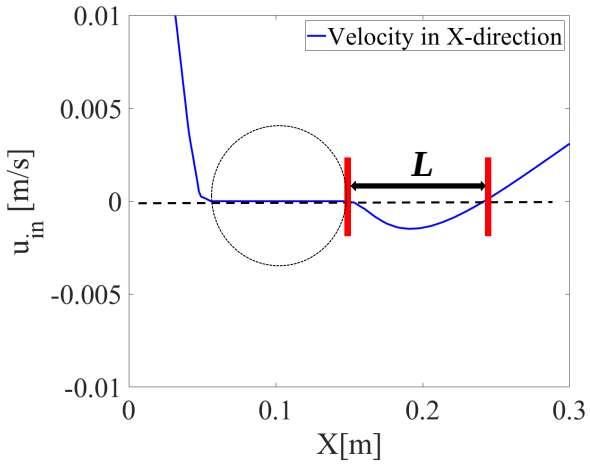

Figure 4.20: Calculation of the recirculation length L corresponding to the velocity in the middle line in Fig. 4.19.

Upon reaching a steady state, a pair of stationary recirculating eddies manifests behind the cylinder. The length of the recirculating region, denoted as L and measured from the furthest point of the cylinder to the end of the eddy, exhibits an increasing trend with the Reynolds number. In Table 4.6, we present a comparative analysis of the drag coefficient, $C_d = 2\boldsymbol{F}_d/(\rho_f \boldsymbol{u}_\infty^2 D)$, and length of recirculating region with previous findings [75–79]. Here, $\boldsymbol{F}_d$ represents the drag force obtained from Eq. (2.40) and ρ_f corresponds to the fluid density.

Table 4.8 presents simulation results for the normalized recirculation length L/D obtained at various resolutions. The relative error is computed based on the average length from Table 4.6. Simultaneously, the drag coefficient is determined and documented in Table 4.9. The corresponding relative errors for both the normalized recirculation length L/D and drag coefficient C_d are graphically represented in Fig. 4.21. Notably, the error slopes for the normalized recirculation length L/D and drag coefficient C_d behave approximately second order and first order, respectively . The results in the table reveal a close agreement between our numerical results and those documented in the literature.

Table 4.8: Comparison of recirculation length for steady flow over a circular cylinder as function of resolution.

Resolution	R1	R2	R3	R4	R5	R6
L/D	1.646	1.746	1.784	1.861	1.833	1.835
Error (%)	10.45	5.0	2.92	1.27	0.26	0.14

Table 4.9: Comparison of drag coefficient C_d for steady flow over a circular cylinder as function of resolution.

Resolution	R1	R2	R3	R4	R5	R6
C_d	2.173	2.149	2.133	2.114	2.081	2.074
Error (%)	5.28	4.12	3.34	2.42	0.82	0.48

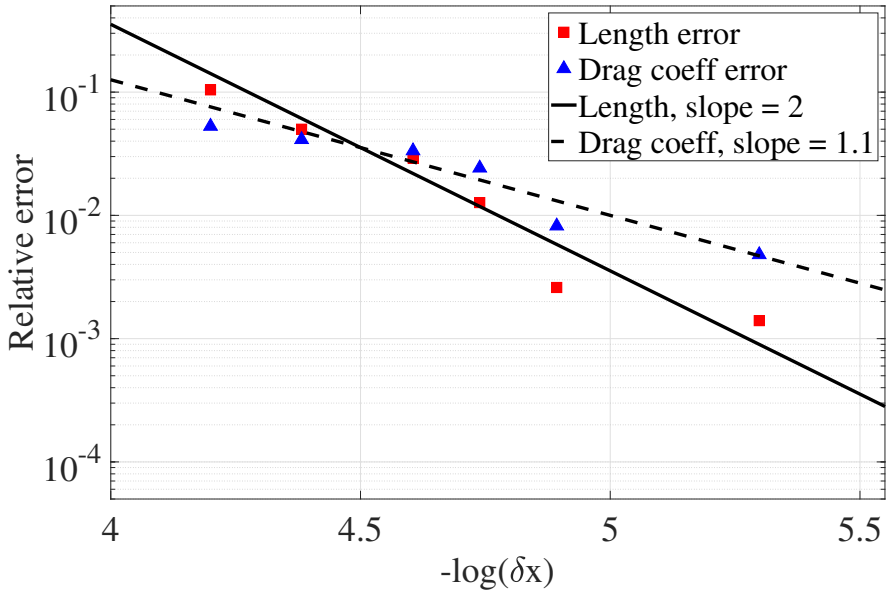

Figure 4.21: Relative error for recirculation length L/D and drag coefficient C_d with different resolutions listed in Table 4.8 and Table 4.9.

4.6 Validation of flow/solid coupling

In order to validate the coupling between the flow field and other solvers, we model the 2-D case presented in [16,17,80], and solved there via an adaptive finite-elements solver. The computational domain is a box of length $L = 204.8$, the grid-size $\delta x = 0.4$ and the time-step $\delta t = 0.008$, all in non-dimensional units. We also set the interface thickness to $W_0 = 1$, the characteristic time to $\tau_0 = 1$, the coupling strength to $\lambda = 6.383$ and the anisotropy strength to $\varepsilon_s = 0.05$. The kinematic viscosity of the flow field is $\nu_f = 92.4$. The flow enters from the left side of the box with a fixed inlet velocity $u_x = 1.0$. The right boundary is set to zero-gradient Neumann boundary condition. The top and bottom sides of the box are set to periodic.

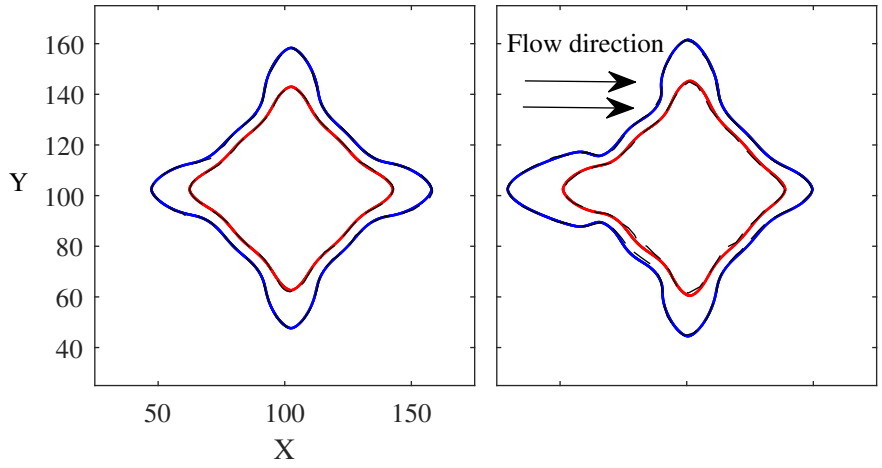

Figure 4.22: Computed PF contours from the dendritic growth in 2-D (left) without and (right) with flow at two different times. Red and blue symbols are our LB results at $t = 72$ and 104 while black dashed lines are corresponding reference data from [17].

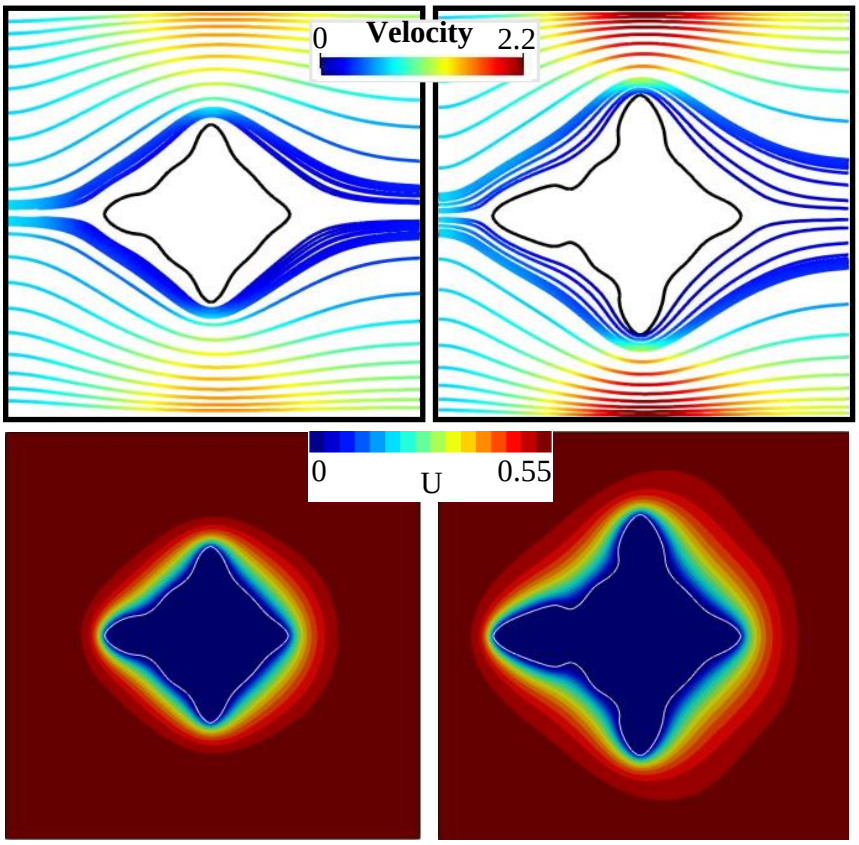

Figure 4.23: (top row) Velocity field streamlines and (bottom row) concentration fields at two different times: (left) $t = 72$ and (right) $t = 104$, as obtained in our LB simulations.

The evolution of all dendrite tips without/with velocity are plotted in Fig. 4.22. It can be observed that the PF contours are in agreement with the reference. To better illustrate the interaction of the flow field with the growing solid, the streamlines and species concentration field at two different times are shown in Fig. 4.23. As expected, one can readily see the non-isotropic distribution of the concentration field around the growing seed caused by the flow field. The incoming velocity induces a higher concentration gradient around the tip on the left causing it to grow faster than its counter-part in the opposite direction.

Table 4.10: Results of different grid resolution for the PF simulations with convection for initial undercooling $U_0 = 0.55$.

Cases	D	d_0/W_0	$N_x \times N_y$	$\tilde{V}_{tip}$	$\tilde{\rho}_{tip}$	Error
1	4	0.139	256×256	0.0257	8.22	6.6%
2	4	0.139	512×512	0.0238	7.68	1.2%
3	4	0.139	1024×1024	0.0241	7.61	-
4	3	0.185	512×512	0.0243	7.63	0.8%
5	2	0.277	1024×1024	0.0246	7.71	2.1%

The results of fundamental numerical test-cases of the present method for dendritic growth with convection are presented in Table 4.10. This table illustrates computed steady-state tip velocities (V_{tip}) and tip radius (ρ_{tip}) of the left-side dendritic tip, which evolves in a direction opposing the flow, through systematic variations in grid resolution (see case 1-3) and diffusion coefficient D (see case 4 and 5). It is crucial to highlight that the dendrite tip velocity is a good quantity to use in such test-cases due to its ease of measurement from the computed results and its high sensitivity to the tip operating state, determined by the surface energy anisotropy. A comparison of the evolution of all tip velocities for the finer grid is shown in Fig. 4.24. It is noteworthy that resolution adjustments can be most easily achieved by altering the spatial unit δx and temporal unit δt; evidently, for the phase-field method to achieve convergence, the computed results should demonstrate independence from the spatial unit δx and the temporal unit δt. The error is calculated based on the relative tip velocity $\tilde{V}_{\text{tip}} = d_0 V_{tip}/D$, with case 3 (finest resolution) serving as the reference for the error calculation in tip velocity. The tip radius, denoted as ρ_{tip}, exhibits an inverse proportionality to the diffusion coefficient D, as expounded in Sec. 4.4.1. In Fig. 4.24, it is evident that the steady-state velocity of dendrite tips normal to the flow shows only minimal variation when compared to that without convection. However, the dendritic tip facing the flow (upstream tip) exhibits significantly accelerated growth compared to the case without convection, while the tip in

the direction of the flow (downstream tip) experiences a notably decelerated growth in comparison to the tips normal to the flow.

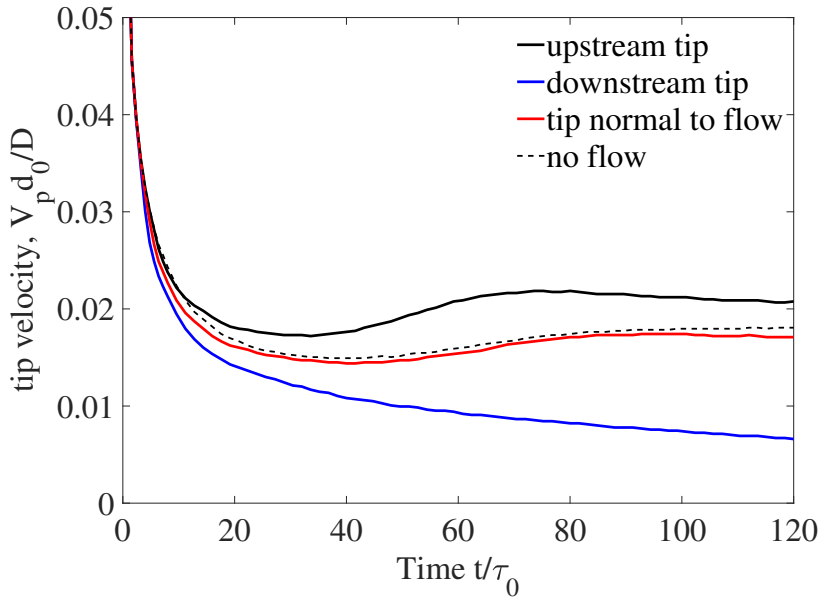

Figure 4.24: Evolution of the dimensionless tip velocities $\tilde{V}_{tip}$ as a function of time in unit τ_0 for supersaturation $U_0 = 0.55$ with the flow velocity $\boldsymbol{u}_{in} = 1$.

4.7 Summary

In this chapter, we initiated our analysis by the validation of the anisotropy ADE, examining isotropic order as a means to enhance the symmetry of the crystal in the simulations. Subsequently, we validated the tip velocity of a single crystal, observing a trend toward maintaining a constant value as the crystal progressed towards a steady state. Following this, we delved into the investigation of key physical parameters, such as anisotropy strength ε_s, capillary length d_0 and initial supersaturation U_0, to assess their influence on crystal morphologies and growth rates.

Moreover, we conducted an exploration of the interface interaction between the solid and liquid phases, comparing it with the no-slip approaches commonly employed. Finally, we delved into the validation of the flow/solid coupling, revealing the hydrodynamic effects on the growth rate of tips in different directions. Notably, it led to a hydrodynamics-induced asymmetrical growth. The tip facing the flow direction exhibited the fastest growth, while conversely, the tip growing opposite to the flow direction displayed the slowest growth. Meanwhile, tips oriented vertically to the flow direction exhibited uniform growth rates due to identical velocities in these regions.

Chapter 5

Crystal simulations in 3D

Contents

5.1 Anisotropy functions in 3D

In order to see the influence of each term of Eq. (2.32), a graphical presentation is plotted on a spherical surface. First, the PF $\phi(\boldsymbol{x},0)$ is initialized (by using Eq. (2.23) inside a cubic domain composed of 200^3 nodes. The initial sphere is set at the center of the domain $\boldsymbol{x}_s = (100,100,100)^T$ with a radius equals to $R_s = 50$ lattice units. Next, the components n_x, n_y and n_z are derived by calculating the gradient of ϕ. Finally, each term of Eq. (2.32) is calculated and post-processed on a spherical surface of radius R_s and centered at $\boldsymbol{x}_s$. 3D simulations are carried out by using three anisotropy function $a_s(\boldsymbol{n})$. The first anisotropy function is the standard one, defined by Eq. (2.30) with $\varepsilon_s = 0.05$. That function favors the growth in the <100>-direction (see Fig. 5.1(a)). The second one is defined by Eq. (2.32) which favors the crystal development in the <110>-direction if $\varepsilon_s = 0$ and $\gamma = -0.02$ (see Fig. 5.1(b)). The last one is defined by Eq. (5.1) which favors the crystal development in the <111>-direction as $\gamma = 0.02$ (see Fig. 5.1(c)). Results are presented in Fig. 5.1 for various values of ε_s and γ. On those figures, the regions highlighted in red and blue signify areas of maximal and minimal growth, respectively. Crystal tips manifest in the maximal zones (red-colored areas), while the blue-colored regions exhibit a concave configuration. All figures are plotted for a same orientation of the coordinate system to facilitate the comparison between functions. The anisotropy function in the <111>-direction (see Fig. 5.1(c)) is defined by:

$$a_s(\boldsymbol{n}) = 1 + 66\gamma n_x^2 n_y^2 n_z^2, \tag{5.1}$$

with $\gamma = 0.02$.

Crystal growth simulations incorporating three distinct anisotropy functions are depicted in Fig. 5.2. As expected, function $Q(\boldsymbol{n}) = n_x^4 + n_y^4 + n_z^4$ demonstrates a preference for growth in the <100>-direction, as shown in Fig. 5.2(a), resulting in a 3D crystal with six tips. The anisotropy function $a_s(\boldsymbol{n})$ defined by Eq. (2.32) with $\varepsilon_s = 0$ and $\gamma = -0.02$, promotes growth in the <110>-direction, as illustrated in Fig. 5.2(b), with each face exhibiting tetrahedral tips in the xy, xz, and yz planes. The function $S(\boldsymbol{n}) = n_x^2 n_y^2 n_z^2$ favors growth in the <111>-direction, resulting in an octagonal faceted crystal with eight distinctive tips, as depicted in Fig. 5.2(c). The top row of Fig. 5.2 presents simulation outcomes obtained by Cartalade et al. [1], while the bottom row showcases results from the present study. Obviously, a notable agreement is observed between the numerical results presented in this work and those reported by Cartalade et al. [1].

In Fig. 5.3, the regions highlighted in red show the growth direction of the side branches. Integrating the information from the figures in the first column with those in the third column, it is evident that the side branches adopt a tetrahedral shape in the crystal growing in the <100> direction and a triangular shape in the crystal growing in the <111> direction.

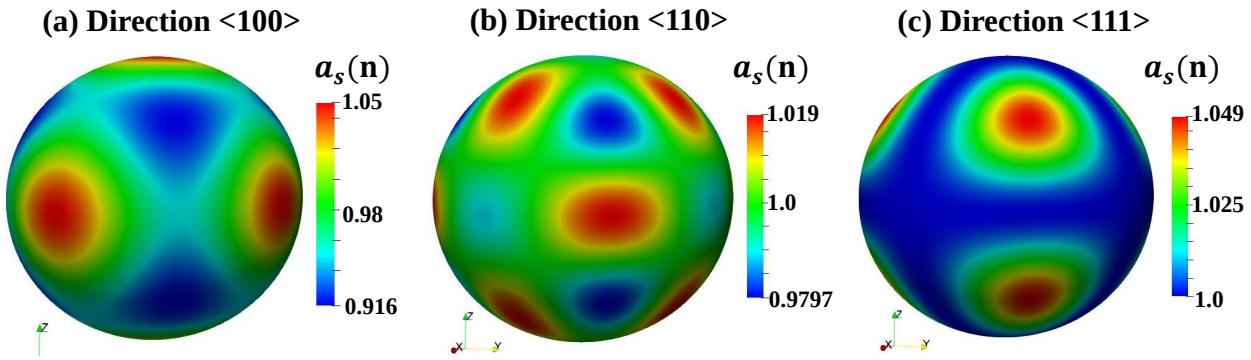

Figure 5.1: Graphical representation of different anisotropy function in 3D with: (a) the anisotropy strength coefficient $\varepsilon_s = 0.05$ in Eq. (2.30); (b) $\varepsilon_s = 0.0$ and $\gamma = -0.02$ in Eq. (2.32); (c) $\gamma = 0.02$ in Eq. (5.1).

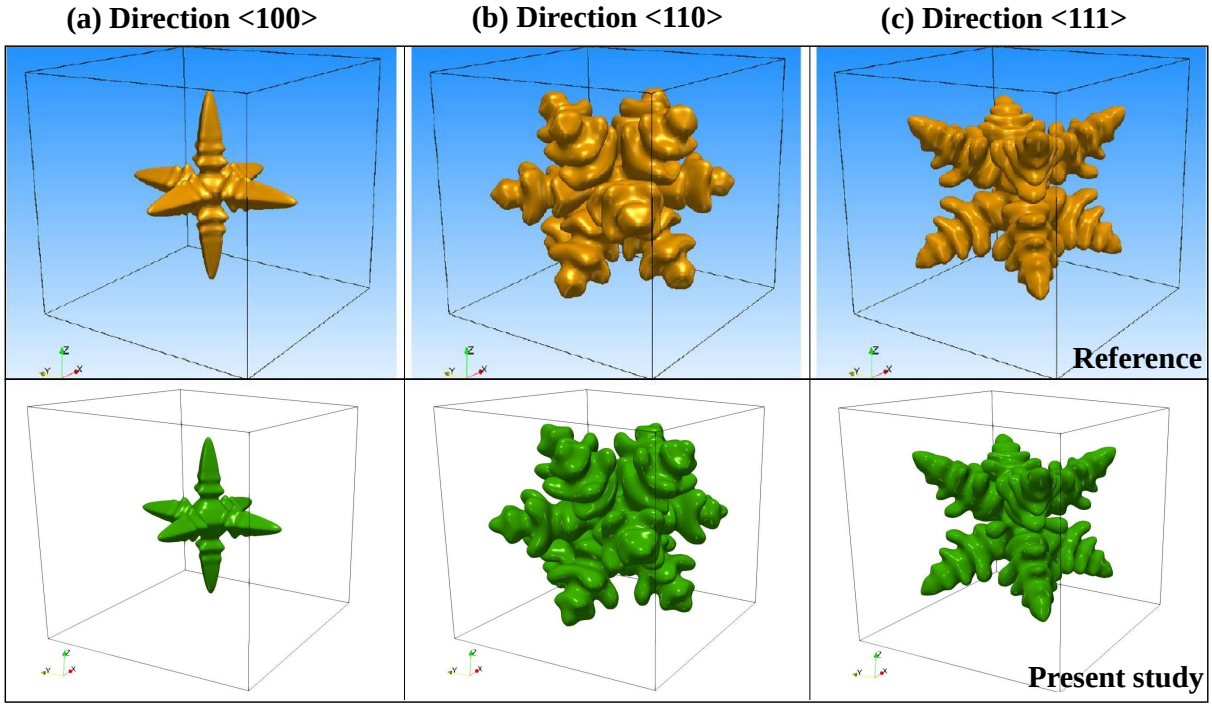

Figure 5.2: Dendritic shapes with contour value of $\phi = 0$ for anisotropy function $a_s(\boldsymbol{n})$ defined by (a) Eq. (2.30) with $\varepsilon_s = 0.05$ at $t = 5 \times 10^3 \delta t$; (b) Eq. (2.32) with $\varepsilon_s = 0$ and $\gamma = -0.02$ at $t = 2.5 \times 10^4 \delta t$; (c) Eq. (5.1) with $\gamma = 0.02$ at $t = 1.5 \times 10^4 \delta t$. The first row shows the simulation results from Cartalade et al. [1] as a reference.

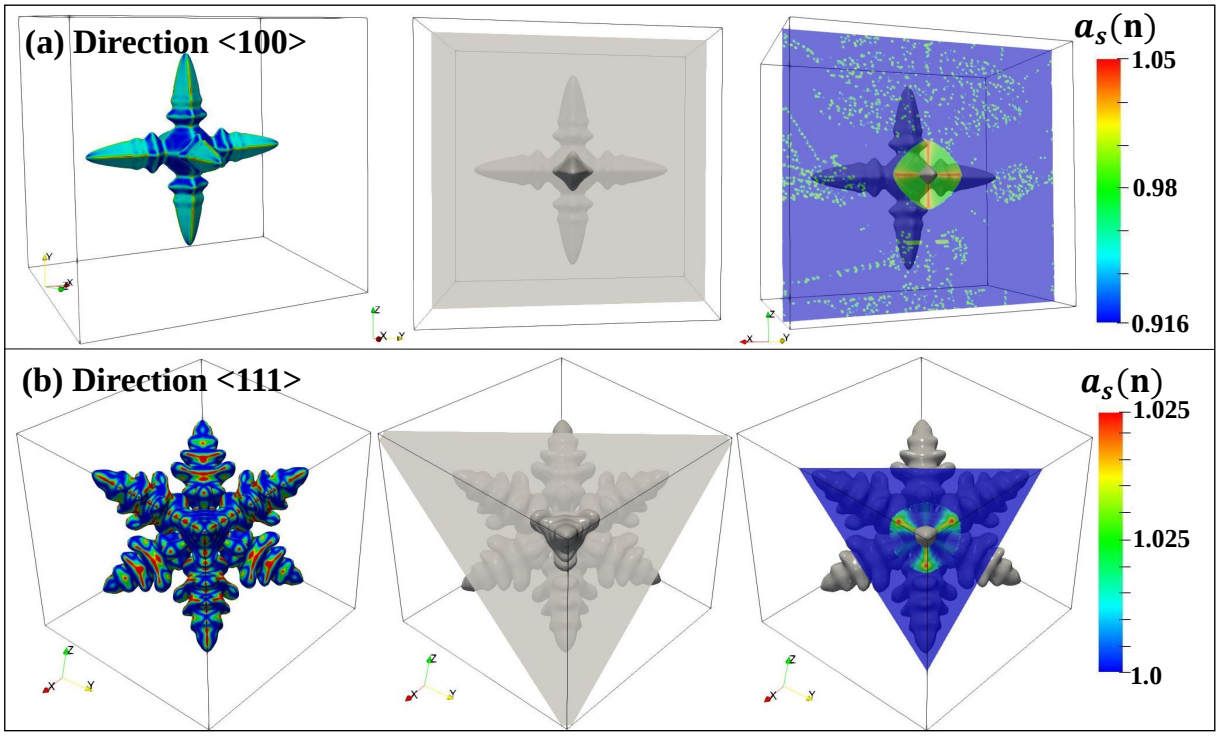

Figure 5.3: Two distinct dendrite shapes are selected: (a) a six-tip crystal aligned with the <100> direction, and (b) an octagonal faceted crystal featuring eight distinctive tips oriented along the <111> direction. In the first column, the anisotropy function $a_s(\boldsymbol{n})$ is depicted on the contour with a value of $\phi = 0$; The second column shows the cut-face shape of the crystal contour at $\phi = 0$; The third column depicts the values of the anisotropy function on the corresponding cut face.

5.2 Undercooling effect

The simulations in this part are conducted using the phase field model outlined in Sec. 2.3 but excluding the temperature equations. The computational mesh employed for this case consists of a total of 501^3 grids. The initial condition is set as a nucleus with a radius, denoted as R_s, of 10 lattice units, located at the center of the computational domain. All boundary conditions are enforced as zero flux conditions for both the PF and temperature equations. The parameters in the simulations are defined as follows: $\lambda = 10$, $\kappa = 1.0$, $\varepsilon_s = 0.05$, $W_0 = 0.0125$ and $\tau_0 = 1.5625 \times 10^{-4}$. An anisotropy function for tip growth direction <100> is employed. The time-step is $\delta t = 1.5 \times 10^{-5}$ and the space step is $\delta x = 0.01$.

To compare and contrast crystal shapes, particularly focusing on iso-values where $\phi = 0$, we plot Fig. 5.4. In this figure, crystal shapes corresponding to different values of undercooling, denoted as Δ, are depicted. Specifically, Fig. 5.4(a) showcases the crystal shape for $\Delta = 0.2$,

Fig. 5.4(b) for $\Delta = 0.25$, and Fig. 5.4(c) for $\Delta = 0.3$. As expected, a larger value of undercooling leads to a faster growth of the crystal. Furthermore, it is observed that side branches become more pronounced with increasing undercooling.

The acceleration of crystal growth with increased undercooling can be explained by two fundamental mechanisms. Firstly, heightened undercooling contributes to the diminution of the interfacial energy barrier between the liquid and solid phases. This reduction in the energy barrier facilitates the nucleation and growth of crystals, particularly in situations where the energy cost of creating new solid-liquid interfaces hinders crystal growth. Simultaneously, undercooling commonly induces heightened levels of supersaturation in the liquid phase. Supersaturation, acting as a potent driving force for crystal growth, enhances the kinetics of both nucleation and subsequent crystal growth processes.

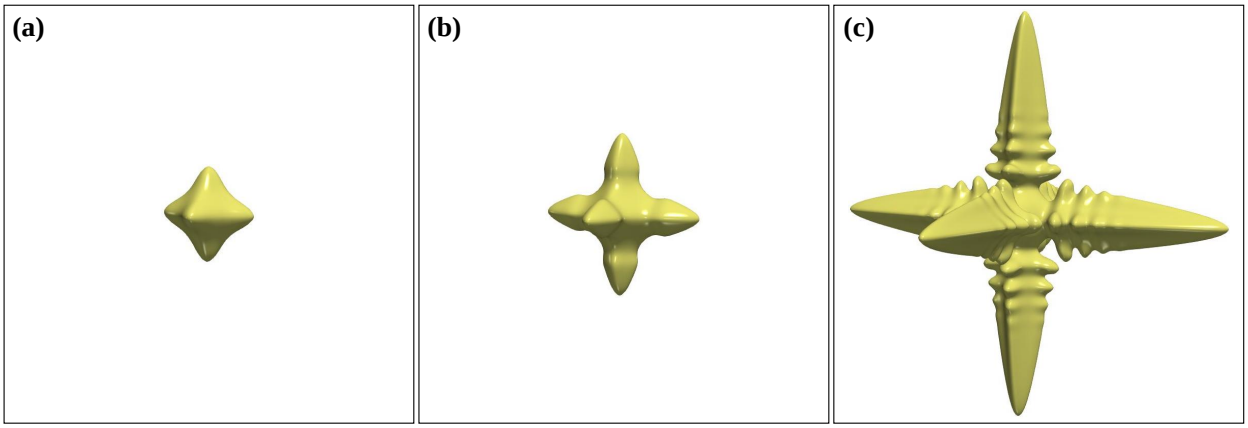

Figure 5.4: Undercooling effect on crystal shape. Iso-values $\phi = 0$ at $t = 1.0 \times 10^4 \delta t$ for (a) $\Delta = 0.2$, (b) $\Delta = 0.25$, (c) $\Delta = 0.3$.

5.3 Reynold number effect

The growth of a crystal is significantly influenced by the fluid flows within the liquid phase. To investigate the hydrodynamic impact on crystal growth, we employ the governing Eqs. (2.16), (2.17) and (2.39), as detailed in chapter 2. The hydrodynamic model and the specific coupling terms applied in this study are derived from the work of Cartalade et al. [12].

In this hydrodynamic model, the PF equation remains unchanged, while modifications are introduced to both the heat equation and the momentum equation. Notably, the PF variable, denoted as ϕ, does not directly contribute to the heat equation and the Navier-Stokes equations. To address this, the advective terms within the solid region are effectively annulled by introducing a new function, $(1-\phi)/2$, which equals 0 within the solid phase and +1 within the liquid phase. This

approach is applied in the simulations, employing parameter values identical to those employed in undercooling sensitivity studies. Additionally, an initial velocity, directed from left to right, is imposed.

The simulations are presented in Fig. 5.5 with different time steps, illustrating the results for two distinct initial velocities, denoted as $\boldsymbol{u}_1$ and $\boldsymbol{u}_2$, where $\boldsymbol{u}_2 = 4\boldsymbol{u}_1$. It is noteworthy that the crystal's growth is no longer symmetrical under these conditions. One side of the crystal exhibits accelerated growth compared to the other sides, and this effect is more pronounced with a higher inflow velocity.

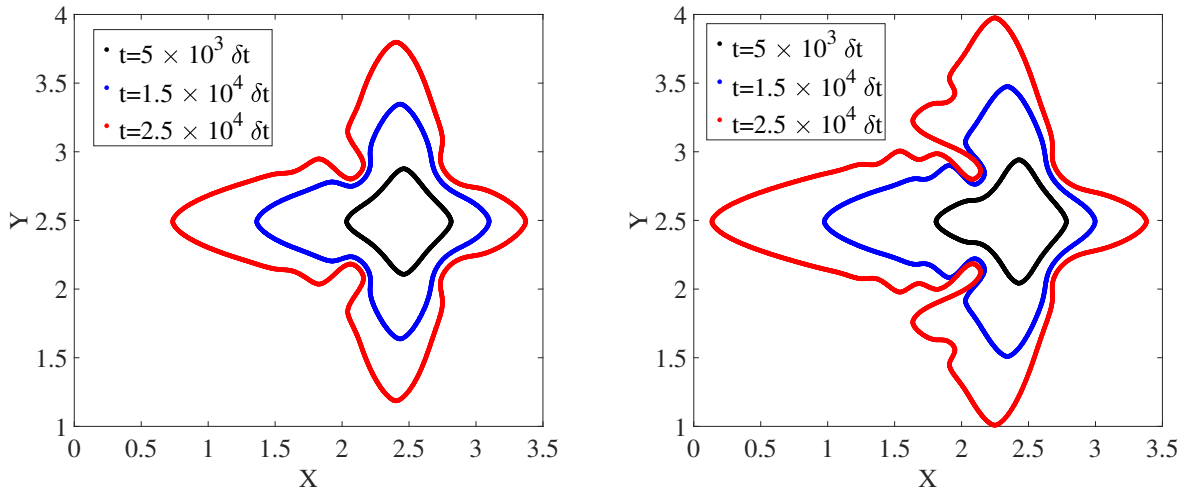

Figure 5.5: Contour value of $\phi = 0$ with velocity $\boldsymbol{u}_1$ (left side) and velocity $\boldsymbol{u}_2 = 4\boldsymbol{u}_1$ (right side), with inflow from left.

In Fig. 5.6(a), the interface releases heat as the liquid undergoes solidification, resulting in a higher temperature within the crystal compared to the liquid. Notably, the crystal growing in the direction facing the flow exhibits a markedly faster growth rate. This phenomenon can be ascribed to more pronounced temperature gradients in the upstream direction compared to the downstream direction. The heightened temperature gradients in the upstream region enable more rapid dissipation of latent heat, thereby facilitating accelerated growth of the side branch.

In Fig. 5.6(b), the flow velocity within the solid phase becomes zero, impacting crystal growth not through the PF equation but rather through the temperature field. Both crystal tips in the top and bottom directions exhibit symmetry due to identical flow velocities in these regions. However, the crystal tip in the upstream direction faces a stronger heat exchange at the interface, resulting in a higher temperature gradient.

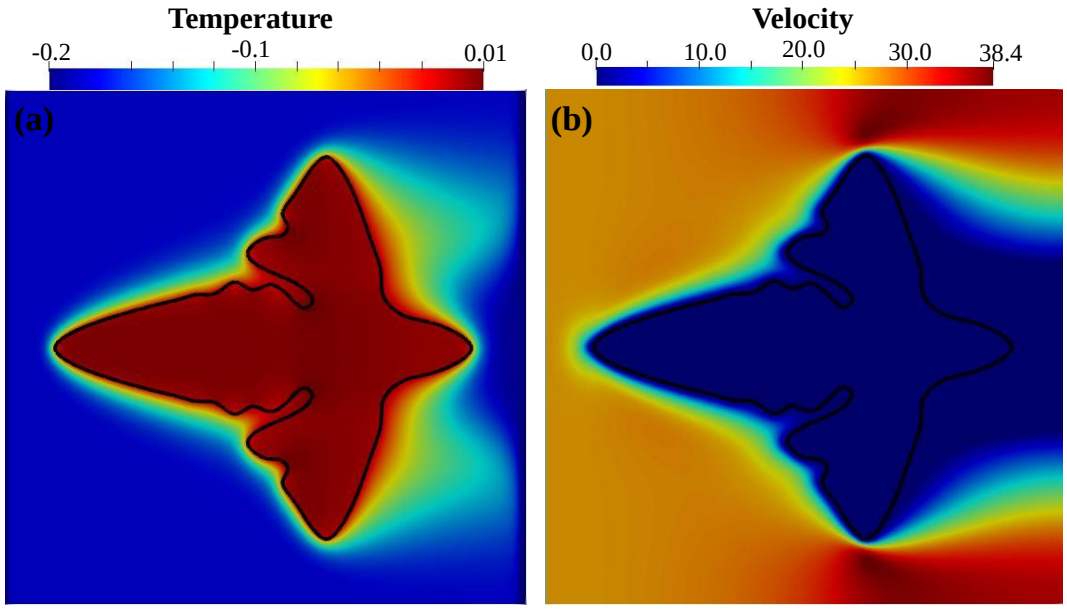

Figure 5.6: Crystal growth for a flow directed from left to right with inflow velocity $\boldsymbol{u}_2 = 26.67$ and initial undercooling $\theta_0 = -0.2$ for (a) Temperature field; (b) Velocity field at $t = 2.5 \times 10^4 \delta t$.

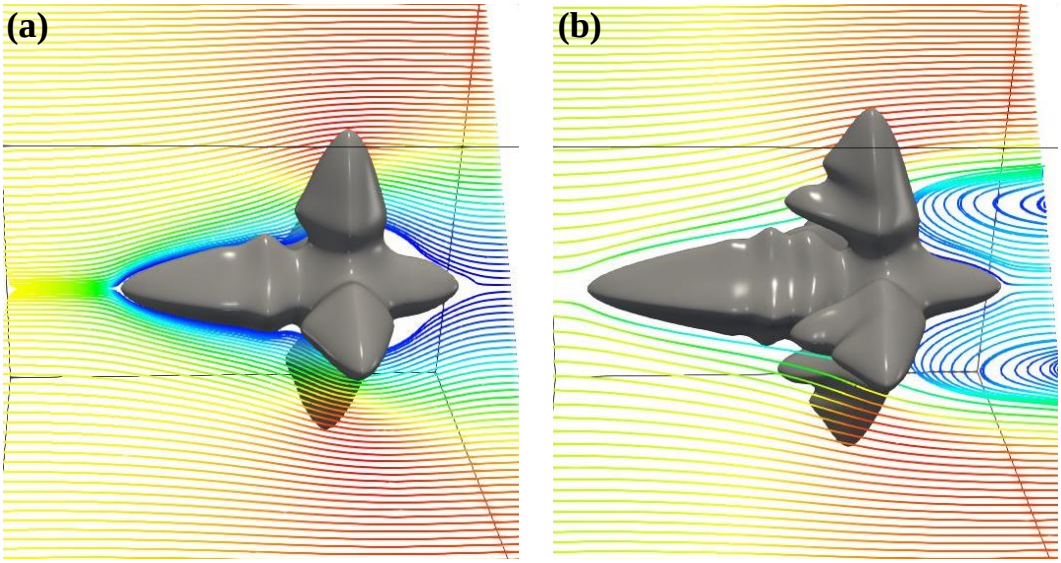

Figure 5.7: Hydrodynamic effect on crystal growth for a flow directed from left to right (a) Initial velocity $\boldsymbol{u}_1$; (b) Initial velocity $\boldsymbol{u}_2 = 4\ \boldsymbol{u}_1$ at $t = 2.5 \times 10^4 \delta t$.

Fig. 5.7 illustrates the contour of the phase value $\phi = 0$ at the same time step in 3D, considering two different velocity ($\boldsymbol{u}_2 = 4\boldsymbol{u}_1$). Obviously, side branches manifest as symmetric tetrahedral shapes on the tips in the upstream direction, owing to the uniform flow velocity around

them. Conversely, the side branches on front and back side exhibit asymmmetry. Despite being tetrahedral-shaped, those facing the flow develop more prominently. These results align with the findings reported in Cartalade et al. [12].

5.4 Simulations of several crystals

After investigation of the convection effect, we are interested in the simultaneous growth of several crystals with hydrodynamic effect. At first, in the presence of multiple crystals, there may be competition for resources, such as available solute in the solution. Larger or more favorably oriented crystals may outcompete smaller or less favorably oriented ones, influencing the overall crystal size distribution. furthermore, the arrangement of multiple crystals can result in complex patterns, especially if the crystals exhibit different growth rates, shapes, or orientations. This can lead to the formation of polycrystalline or dendritic structures. At last, the existence of multiple crystals can alter local temperature and flow fields within the system. This, in turn, may influence the growth rates and morphologies of the crystals.

For simulating the growth of three crystals, three initial grains are set in the middle of a box (see Fig. 5.8). Each of them will grow progressively during the simulation with the same anisotropy function. Three seeds are initialized in a computational domain composed of $1006\times401\times401$ nodes. The radius is set at $R_s = 10$ lattice nodes for each of them and positions are $\boldsymbol{x}^1 = (2, 1.9, 1.9)$, $\boldsymbol{x}^2 = (5, 2, 2)$ and $\boldsymbol{x}^3 = (8, 2.1, 2.1)$. Parameters are $\delta x = 0.01$, $\delta t = 1.5 \times 10^{-5}$, $W_0 = 0.0125$, $\tau_0 = 1.5625 \times 10^{-4}$, $\lambda = 10$, $\varepsilon_s = 0.05$, $\kappa = 1.0$ and $\Delta_0 = 0.2$. The fluid viscosity is $\nu_f = 0.667$ and the inlet velocity $\boldsymbol{u}_{in} = 26.67$, from left to right direction. The boundary conditions at the top and bottom, as well as at the front and back, are periodic.

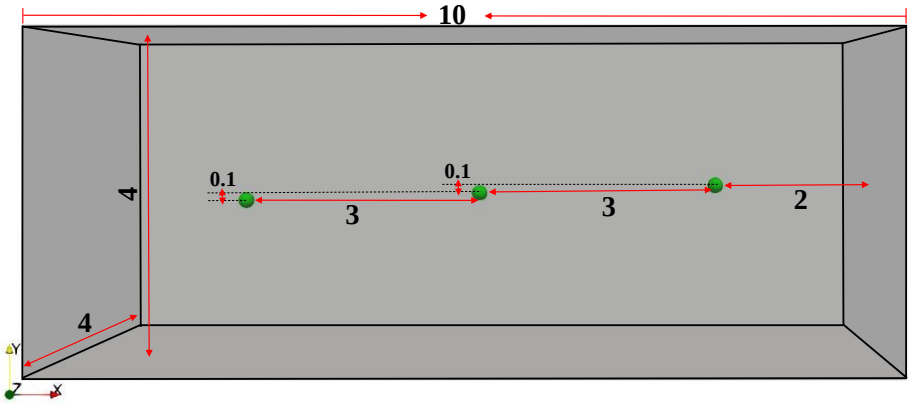

Figure 5.8: Box geometry for several crystals in 3D.

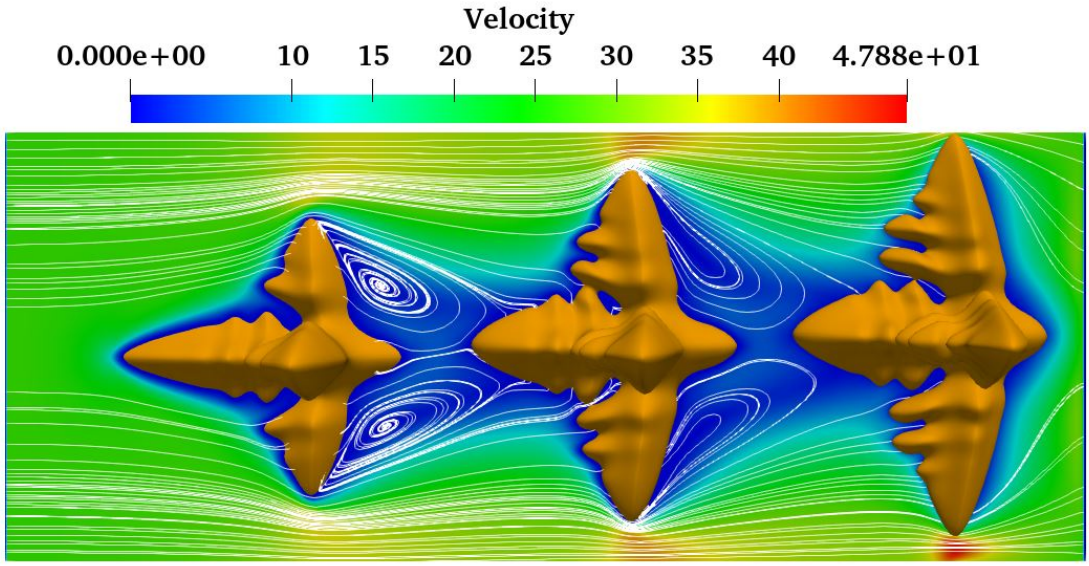

Figure 5.9: Hydrodynamic effect on crystal growth for a flow directed from left to right with inflow velocity $\boldsymbol{u} = 26.67$ at $t = 2.5 \times 10^4 \delta t$.

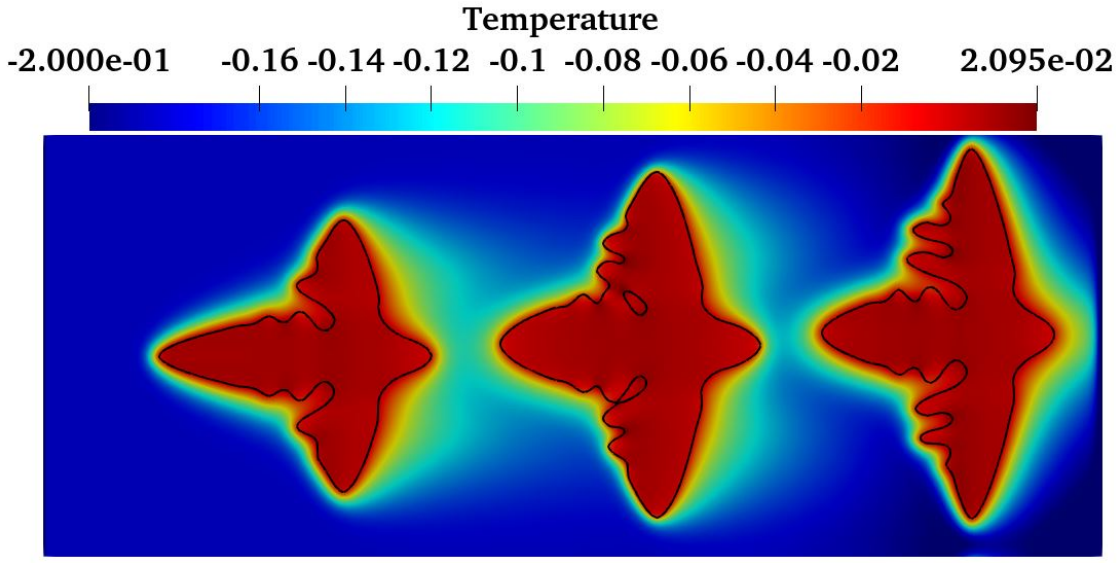

Figure 5.10: Temperature field on crystal growth for a flow directed from left to right with initial velocity $\boldsymbol{u} = 26.67$ at $t = 2.5 \times 10^4 \delta t$.

Results are presented on Fig. 5.9 and Fig. 5.10. The growth of crystals from left to right is faster, leading to more obvious side branches. The presence of a crystal in the forefront impedes the flow velocity of the main body of the crystal positioned behind it. Consequently, the upper and lower branches of the rearward crystals experience a more pronounced influence from the

augmented flow velocity. As a result, the tips of these branches dissipate heat more rapidly, leading to an increased temperature gradient. This heightened temperature gradient contributes to the accelerated development of the branches.

5.5 Multiple crystals with a baffle

In the preceding section, an examination of several crystals was conducted. In the subsequent investigation, a baffle is introduced around the inlet of the rectangular box. The computational domain is discretized with $1006 \times 501 \times 501$ points, and the governing parameters are maintained consistent with those outlined above. The baffle is a flat cylinder and its size is shown in Fig. 5.11. Crystal positions are $\boldsymbol{x}^1 = (2, 2.5, 2.5)$, $\boldsymbol{x}^2 = (5.9, 2.5, 2.5)$ and $\boldsymbol{x}^3 = (8.4, 2.5, 2.5)$.

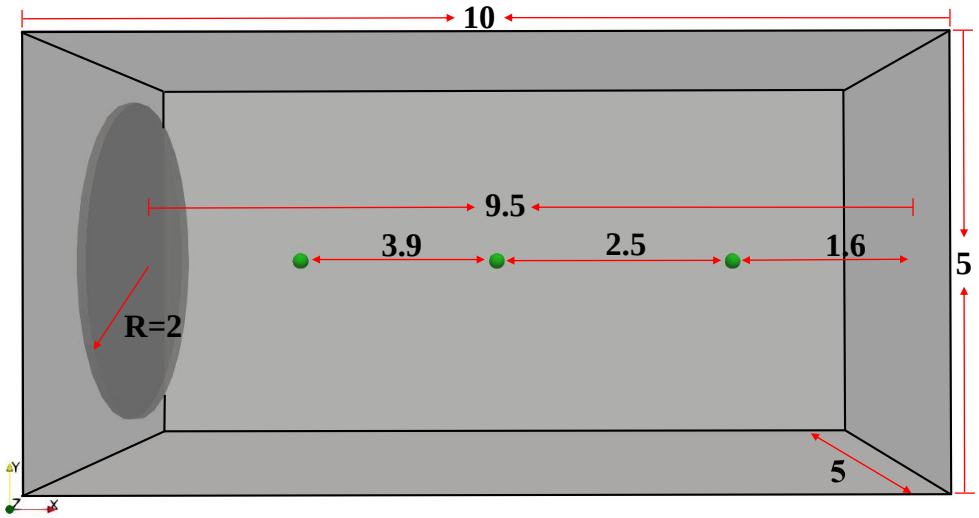

Figure 5.11: The geometry with baffle in 3D.

Results are presented in Fig. 5.12 and Fig. 5.13. Notably, the crystal on the left exhibits marked differences compared to its counterpart in Fig. 5.9. The presence of the baffle impedes the flow velocity in the upstream direction of this crystal, resulting in the explicit development of side branches in the downstream direction. These side branches are particularly conspicuous and well-defined. Toward the terminus of the first crystal, an acceleration in velocity induces faster growth of side branches in this specific direction.

In contrast to the scenario depicted in Fig. 5.9, the progression of crystal growth from left to right is discernibly decelerated, reducing side branch formations. This phenomenon is attributed to the substantial diameter of the baffle situated in the frontal position.

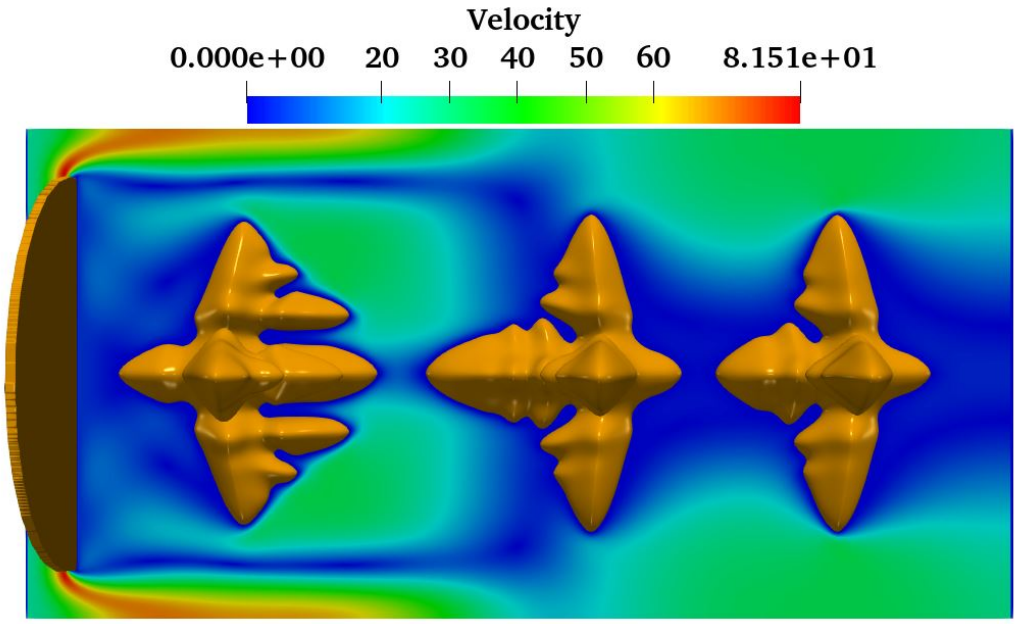

Figure 5.12: Hydrodynamic effect on crystal growth for a flow directed from left to right with inflow velocity $\boldsymbol{u} = 26.67$ at $t = 2.5 \times 10^4 \delta t$ with a baffle behind the inlet area.

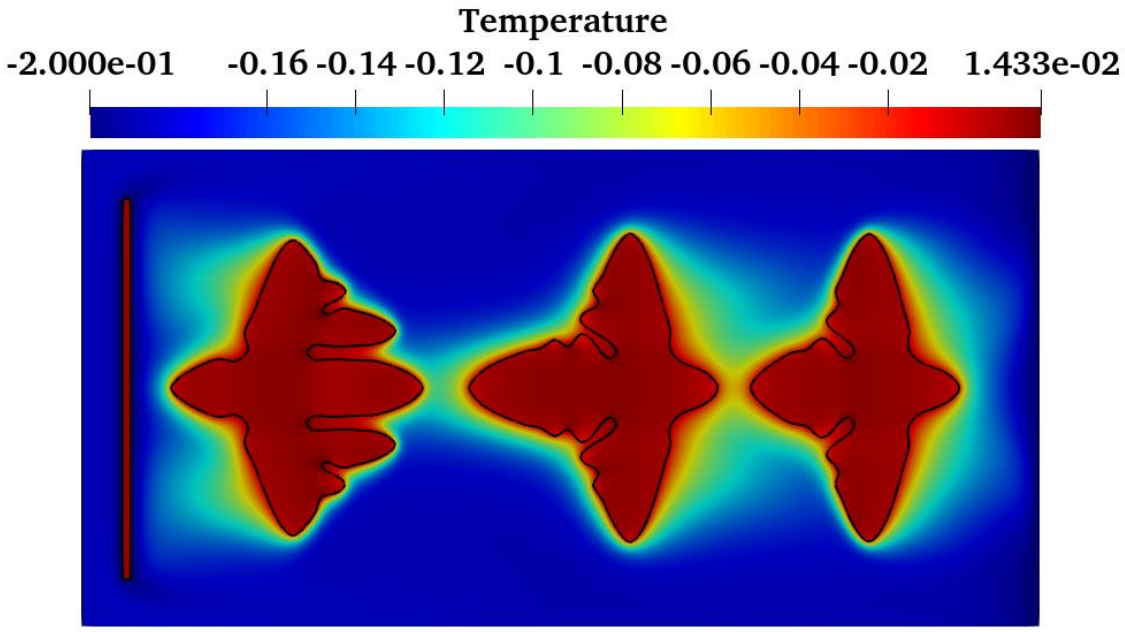

Figure 5.13: Temperature field on crystal growth for a flow directed from left to right with inflow velocity $\boldsymbol{u} = 26.67$ at $t = 2.5 \times 10^4 \delta t$ with a baffle behind the inlet area.

In Fig. 5.12, it is noteworthy that the top-bottom tips exhibit accelerated growth compared to the tips in the horizontal direction for the first and last crystal. This disparity is a consequence of

the heightened temperature gradient at these locations. Owing to the narrow inter-crystal gap, tips in the horizontal direction engage in mutual competition, resulting in insufficient solute availability for complete development. Consequently, the tips in the horizontal direction exhibit a comparatively slower growth rate than their counterparts in the vertical directions.

5.6 Summary

In this chapter, we have initially discussed the formulations of the anisotropy function $a_s(\boldsymbol{n})$. Subsequently, we conducted simulations encompassing various shapes of 3D crystals, utilizing both standard and nonstandard anisotropy functions that favor growth in <100>-, <110>-, and <111>-directions. The impact of undercooling and Reynolds effects on the growth rate and dendrite shapes of the crystal was then explored. Higher undercooling values were found to correlate with an increased growth rate, with side branches appearing earlier and exhibiting more distinct behaviors.

Following this, we extended our simulations to investigate the simultaneous growth of multiple crystals, each defined by the same anisotropy function. The positions and flow velocities exerted notable influences on the shapes and growth rates of the crystals, illustrating a competitive dynamic for solute acquisition, particularly in the development of branches. The interaction between multiple crystals and flow velocities also induced alterations in temperature fields, thereby affecting the growth rates and morphologies of the crystals.

Finally, we introduced a baffle to examine its impact on crystal habits. Our findings indicate that the baffle exerts influence on the flow field, indirectly affecting the temperature field of the crystal. Consequently, alterations in growth rates and morphologies were observed. This comprehensive exploration underscores the intricate interplay of factors influencing crystal growth in complex systems.

Chapter 6

Modeling ice crystal growth [1]

Contents

[1] Part of this chapter has been published in

- **Q. Tan**, S.A. Hosseini, A. Seidel-Morgenstern, D. Thévenin, and H. Lorenz. Modeling ice crystal growth using the lattice Boltzmann method. *Physics of Fluids*, 34(1):013311, (2022).

6.1 Introduction

Ice crystals and their growth are of interest in many fields such as environmental sciences, agriculture and industries as aviation (encountering de-icing issues). Due to the wide spectrum of habits they take on, they have been the topic of scientific research for decades [81–83]. Johannes Kepler was the first person to explore the growth mechanisms of snowflakes in 1611, and attempted to explain the possible origins of snow crystal symmetry [84]. With the development of photography in the late 19th century, Wilson Bentley [85] collected in 1931 thousands of snow crystal images [86]. In 1938, Ukichiro Nakaya and his co-workers [87–89] conducted comprehensive experimental studies of ice crystal growth to determine the relationship between growth conditions and crystal shape. The different growth modes and associated habits as a function of temperature and supersaturation (humidity) are illustrated in Fig. 6.1.

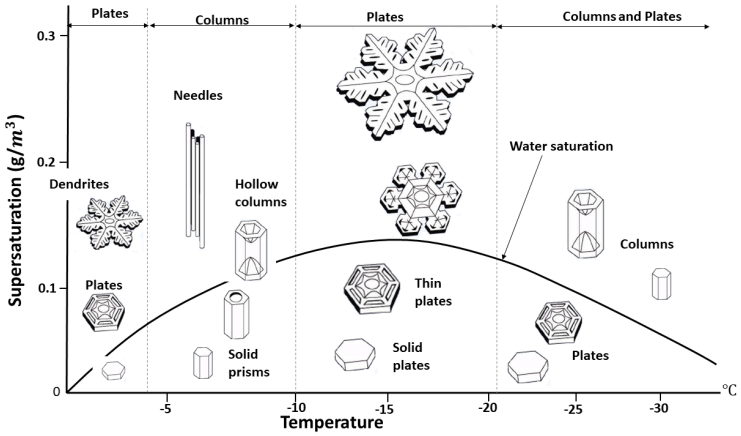

Figure 6.1: The snow crystal morphology diagram, showing the morphology of ice crystals growing from water vapor in air at 1 bar as a function of temperature and supersaturation. This figure is taken from [90, 91].

Overall, based on the dominant growth direction, snowflakes can be classified as pertaining to one of these two categories: plates, or columns/needles. The growth mode is essentially dictated by the temperature, while growth rate, and the associated instabilities, are affected by both temperature and humidity. As observed in Fig. 6.1, crystal habits alternate between flat and columnar. Transitions between the different modes, i.e. plate and column, occur at around -5, -10 and -20°C. Furthermore, higher humidity and thus, higher supersaturation as crystallization driving force contributes to more pronounced instability effects and therefore more complex shapes. Despite the efforts by Ukichiro Nakaya [89] and other researchers, much of the phenomenology behind the growth of snowflakes still remains uncertain [92–95]. In 1958, Mason [96] suggested that the basic habit is determined by the surface diffusion rates. Later, Nelson and Knight [97] suggested

that layer nucleation rates influence the morphology of snow crystals. Libbrecht [94] suggested that the different crystal habits and instabilities appearing during growth are direct consequences of two main competing mechanisms: vapor diffusion in air and kinetics of the water molecules attachment to the crystal surface [88,98,99]. The geometrically ordered potential field on the crystal surface dictates the growth into faceted structures (resulting from the molecules' arrangement within the crystal lattice), while diffusion contributes to growth instabilities that produce dendritic branching and associated complex structures. Attempts to further explain the growth mechanism of snowflakes are still ongoing.

While most of the previous research was focused on experimental studies of ice growth, widespread effort has also been put on developing mathematical models and numerical tools. Microscopic models and simulations such as Molecular Dynamic simulations [29] have been conducted to analyze fundamental processes such as surface adsorption and diffusion. While physically sound, these simulations are limited in time and space and are not efficient for simulations of a full snowflake (especially at later stages when instabilities appear and the crystal grow in size). So-called mesoscopic formulations are an interesting alternative. The cellular automaton of Gravner and Griffeath [100] is an illustration of such approaches. While providing spectacular results in predicting faceted growth, such models lack established connections with physical processes and parameters [101]. Furthermore, reliable models introducing additional physics such as interaction with a flow field are yet to be developed [50]. At the macroscopic level, crystal growth is modeled using either sharp or diffuse interface formulations. Various snowflake morphologies were simulated by Barrett et al. [102] with a sharp interface model. However, only small supersaturations could be considered because of the numerical cost of the interface parametrization [103]. In recent years, the PF model [10], a type of diffuse interface formulation, has become one of the most popular methods for the simulation of crystal growth. The PF model is a powerful tool to simulate interface development in the crystallization process as the model does not require explicit tracking of the interface via front-tracking algorithms. In addition, the non-linear partial differential equations are obtained from the principles of non-equilibrium thermodynamics making the interface dynamics consistent without the need for explicit boundary treatments. Over the past several decades, few successful attempts are reported to model faceted snowflake growth [14, 15]. Comparisons with experimental data were rather promising. While readily applied to generic systems, these models have rarely been used to simulate realistic systems such as snowflake growth.

For the sake of clarity, this chapter is organized into two different sections. In the first section the results for snowflakes in the plate regime are presented and discussed. The effect of fluid flow on snowflake growth are presented in the second section.

6.2 Ice crystal habit in thin-plate regime as a function of temperature and supersaturation

In this section, we first study the plate growth regime of snowflakes as a function of the supersaturation to showcase the ability of the proposed model to capture the wide variety of habits exhibited by snowflakes. The governing Eqs. (2.25) and (2.26) ($\Gamma_z = 0$ for 2D) are described in chapter 2.

The focus of the present chapter is on the plate growth regime ($\varepsilon_z = 0$). According to the Nakaya diagram in Fig. 6.1, the widest variety of habits and instabilities in this regime can be observed at $-16°$C where the saturated vapor density of ice [92] is around $\rho^I_{sat} = 1.21\text{g/m}^3$ and the saturated vapor density of water [104] is around $\rho^W_{sat} = 1.65\text{g/m}^3$. The excess density over vapor-water equilibrium is $\Delta\rho^W = \rho - \rho^W_{sat}$ which is shown in the Fig. 6.1 by the vertical axis, where ρ^W_{sat} is the saturation vapor density of water. The supersaturation is given by $U = (c - c^I_{sat})/c^I_{sat}$, where c^I_{sat} is the saturation number density of vapor of ice at temperature T. Using $\rho = m_{H_2O}c$, where m_{H_2O} is the mass of a molecule of water, it could be written $U = (\Delta\rho^W + \rho^W_{sat} - \rho^I_{sat})/\rho^I_{sat}$ and different snowflake morphologies are obtained by changing the initial excess vapor density $\Delta\rho^W$. According to [105], the melting temperature of the snow crystals is $T_m = 276.9$K, heat capacity $c_p = 4.23 \times 10^6 \text{Jm}^{-3}\text{K}^{-1}$, diffusion coefficient of the vapor $D = 1.17 \times 10^{-7}\text{m}^2\text{s}^{-1}$, surface tension $\gamma = 2.845 \times 10^{-2}\text{Jm}^{-2}$, and latent heat $L = 1.12 \times 10^8 \text{Jm}^{-3}$. The capillary length is computed to be $d_0 \simeq 2$ nm. The coupling parameter is set to $\lambda = 3$ [11].

The simulation parameters are chosen as: $W_0 = 1.25\delta x$ and $\tau_0 = 20\delta t$. The influence of grid resolution has first been checked, as shown in Table 6.1 and Fig. 6.2. For this purpose, grid resolutions between 800×800 and 4000×4000 have been compared, the latter one being considered as reference solution. The errors are again calculated using Eq. (4.3). Table 6.1 shows that the grid resolution of 1600×1600 is sufficient in the present configuration for an accurate simulation of snowflakes, leading to a relative error below 1%. Hence, all corresponding simulations were conducted in a box with a discretization of 1600×1600. The anisotropy strength was set to $\varepsilon_{xy} = 0.05$. To produce different snowflake morphologies, the following parameters were varied: initial supersaturation u_0, depletion rate L_{sat} and excess density $\Delta\rho^W$. The corresponding values are listed in Table 6.2.

The results obtained for the conditions listed in Table 6.2 are shown in Fig. 6.3 along with corresponding numerical and experimental data from [14] and [90]. The Peclet number is about 0.6 during the simulations of this regime.

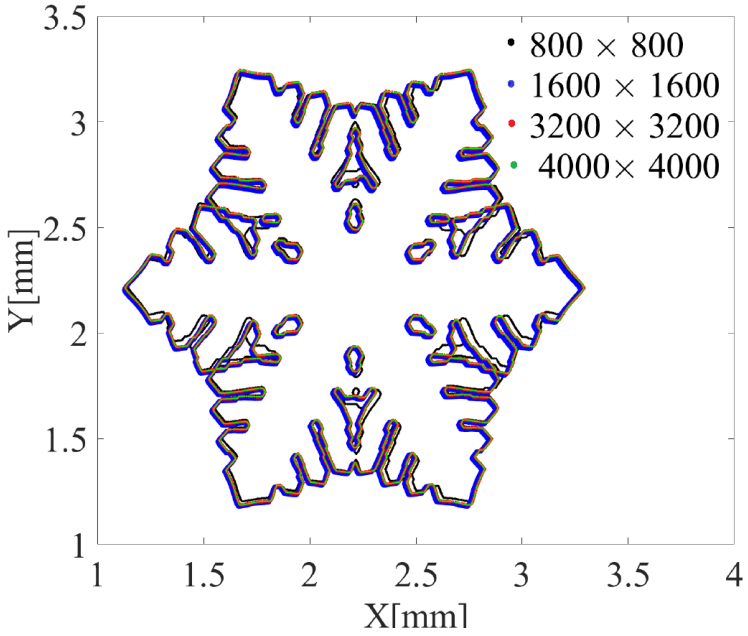

Figure 6.2: $\phi = 0$ iso-contour for $U_0 = 0.8$ and $L_{sat} = 1.0$ with 800 × 800, 1600× 1600, 3200 ×3200 and 4000×4000 grid points, respectively.

Table 6.1: Influence of grid resolution for PF simulations of snowflakes

Resolutions	800×800	1600× 1600	3200 × 3200
% Error	2.65	0.081	0.043

Table 6.2: Parameters chosen to investigate different snowflake morphologies

Nr.	shapes	$U_0[-]$	$L_{sat}[-]$	$\Delta\rho^W[\mathrm{g}/m^3]$
1	solid plate	0.4	2.0	0.03
2	stellar plate I	0.5	1.8	0.15
3	sectored plate	0.5	1.6	0.15
4	stars	0.6	1.0	0.27
5	fern dendrite	0.8	1.6	0.51
6	fernlike stellar	0.7	1.0	0.39
7	stellar plate II	0.5	1.2	0.15

Table 6.3: Comparison of snowflake characteristic size between experiments [106] and simulations in present study

Size (mm)	solid	stellar	sector	star	fern dendrite
Simul.	0.2	0.3	0.46	0.41	2.2
Exper.	0.2	0.35	0.4	0.45	2

Figure 6.3: The morphology numbers are from 1 to 7 (from left to right) in this figure, as indicated in Table 6.2. Comparison between (top) real snowflakes photographs taken from Libbrecht's experiments [90], (middle) our PF simulations in two dimensions, and (bottom) the simulations from [14] in three dimensions

.

The primary habit of the crystal (six-fold symmetry) is dictated by the anisotropy function (and the microscopic crystallographic structure). At lower supersaturation values where the adsorption rate is slow, the surface diffusion process characteristic time is smaller and therefore dominates over surface adsorption. More explicitly it means that the adsorbed water molecules have enough time to propagate on the crystal surface and find the points with the lowest potential (dictated by the molecules' arrangement in the crystal lattice). Furthermore, given the low growth rate and gradients, the surface is not subject to branching instabilities. As the supersaturation goes up, the larger adsorption rate at the sharper parts of the interface (regions with the highest curvatures and consequently highest surface area) result in the formation of six thick branches (usually referred to as primary branches). In the lower supersaturation regimes these primary branches have a faceted structure following the symmetry of the crystal. As the concentration goes further up, the branches

get thinner and rougher (the straight faces tend to disappear); this eventually produces secondary instabilities and branches going towards a somewhat fractal structure. All the obtained crystal habits, are in excellent agreement with not only numerical simulations from [14] but also experimental data from [90]. Further comparing the different crystal habits to Nakaya's diagram, it can be concluded that the proposed model correctly predicts the behavior of the crystal in the platelet regime. Table 6.3 shows that the size of the snowflakes obtained in the simulations are comparable with the experiments [29]. The next part will focus on the effects of ventilation on the evolution of the crystal habit.

6.3 Hydrodynamic effects on snowflakes in 2D

Growth of snowflakes under forced convection is a topic of interest, as for example falling flakes are usually subject to ventilation. The dynamics of snowflake growth under ventilation effects are not very well-documented. Libbrecht and Arnold [107, 108] worked on an aerodynamic model to show the growth and appearance of new habits such as the triangular snow crystals both in nature and in laboratory settings. Furthermore, the anisotropy induced by the flow field can, when pronounced, cause different regions on the surface of the crystal to grow in different regimes. The present section will focus on the recovery of these effects and on a qualitative validation with experimental observations.

For the first configuration, the domain has a size of 1600×1600 grids, the initial seed radius is $R = 25\delta x$ and the initial vapor density $\rho_0 = 1.364\text{g/m}^3$ (supersaturation $U_0 = 0.2$). The Reynold number is set as $\text{Re} = u_y d/\nu_f = 12.5$, where d denotes the diameter of the initial crystal seed. The grid size is set to $\delta x = 4.8 \times 10^{-6}$ m while the time-step is $\delta t = 2 \times 10^{-7}$ s. The coupling strength is $\lambda = 3$. The flow blows from the bottom to the top along the y-axis. The inlet velocity is set to $u_y = 0.12\text{m/s}$ and the kinematic viscosity to $\nu_f = 1.152 \times 10^{-6}\text{m}^2/\text{s}$. The outlet is modeled using a zero-gradient Neumann boundary condition, while along the x-axis periodic boundary conditions are used. The resulting snowflake morphology is shown in Fig. 6.4.

It can be clearly observed that the crystal growth on the side facing the incoming flow is higher than its neighboring sides. Furthermore, its opposite side is growing slower than its neighbour. Both of these non-symmetrical growth rates push the habit towards, first a non-symmetrical hexagon and then a triangular shape, in agreement with experimental observations.

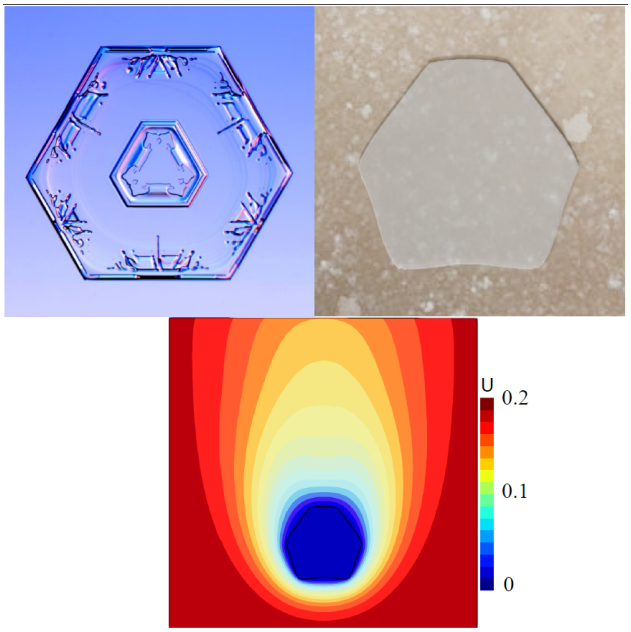

Figure 6.4: The morphology of the asymmetrical hexagonal snowflakes at $t = 7500$ in units of τ_0. Top left: experimental image [107, 108], top right: our LB simulation, and bottom: associated supersaturation field.

To further put the effect of hydrodynamics into perspective we also consider another test-case with the same configuration as the previous one, however with a larger initial supersaturation. The initial vapor density is set to $\rho_f = 1.445\text{g/m}^3$ (supersaturation $U_0 = 0.3$). The inlet velocity is set to $\boldsymbol{u}_y = 0.24\text{m/s}$. The Reynolds number is Re$=25$. The evolution of the crystal, streamlines and supersaturation fields at different time-steps are illustrated in Fig. 6.5.

As observed in these figures, the natural anisotropy in supersaturation around the crystal is further accentuated by the formation of two re-circulation zones. Due to the presence of these flow structures, the growth rate on the top half of the crystal is slowed down and brought into the regular hexagonal habit regime. The lower half, however, is subject to larger concentration gradients (further amplified by the incoming convective flux) and therefore exhibits primary branching instabilities. As the system progresses further in time, the bottom-facing branches distinguish themselves from the side-branches, as we observe secondary instability effects on them, along with a much faster growth rate on the main branches. These observations are in clear agreement with expectations from fluid dynamics. The dimensionless tip velocity shown in Table 6.4 is defined as $\tilde{V}_{tip} = V_p d_0/D$, with d_0 the capillary length. As documented in Table 6.4, the growth rate of the tip facing the flow is about three times larger than the growth rate of snow crystal tips in the opposite sides. Going into the details of the crystal structure and supersaturation fields, we can also see that secondary branching instabilities are not present at the bases of the down-facing primary branches.

That is explained by the fact that they are in a flow stagnation zone (due to the built-up pressure in this closed area), where the supersaturation is almost fully depleted. All of these effects are in qualitative agreement with experimental observations reported in the literature [18].

Table 6.4: Comparison of dimensionless tip velocity $\tilde{V}_{tip}$ in non-symmetrical snowflake growth at different time steps.

$\tilde{V}_{tip}$ at timestep	0	4000	8000
facing side	0	2.2×10^{-3}	1.72×10^{-3}
opposite side	0	9.55×10^{-4}	5.8×10^{-4}

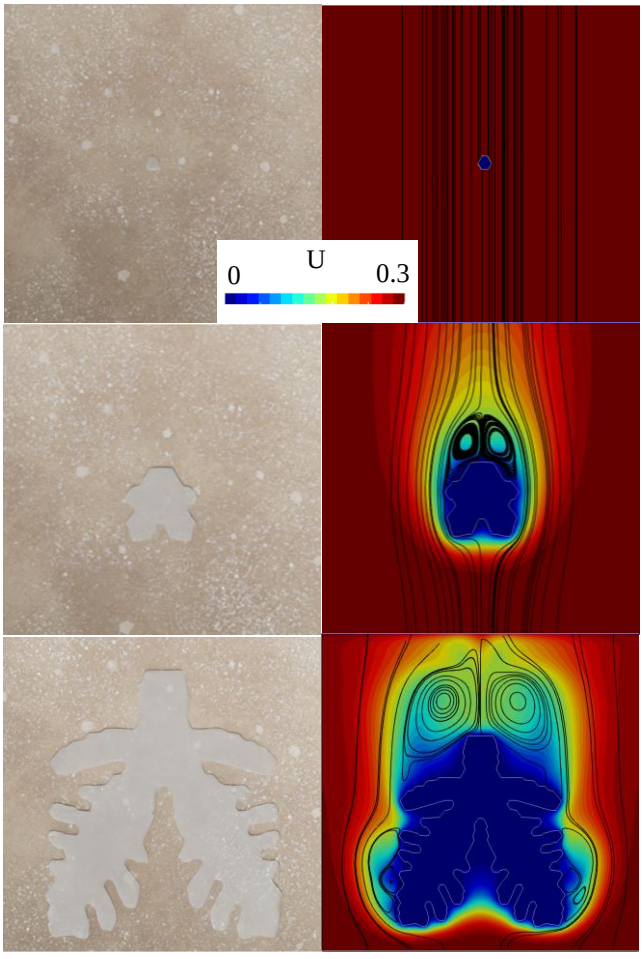

Figure 6.5: (left) morphology of the snowflakes with ventilation effects and (right) velocity field streamlines and supersaturation fields at (from top to bottom) $t = 0$, 4000 and 8000 in units of τ_0.

6.4 Final remarks

In this chapter, we presented a modified phase-field model that describes vapor-ice phase transition through anisotropic surface tension, surface diffusion, condensation, and water molecule depletion rate. It focused on the development of such a coupled flow/species/phase solver in two spatial dimensions based on the LBM. First, generic test-cases have shown that this model closely matches results from other solvers for the system of macroscopic PDEs needed for this system. It was further shown that the proposed formulation was able to capture the different crystal habits in the plate growth regime. The obtained numerical results are generally in good agreement with experimental data and the Nakaya diagram predictions [89]. To go one step further, the model was also used to look at the possible effects of forced convection on the growth dynamics and resulting asymmetrical shapes.

The numerical model used in this study and relying on a combination between LB and PF model based on the Allen-Cahn equation, while requesting only second-order spatial discretization and being fully local, should provide the best possible combination between accuracy and computational efficiency. The Allen-Cahn formulation being second order, like the underlying LBM mode, it is has been preferred over the Cahn-Hilliard equation for reasons of compatibility. The performance of this combination remains to be demonstrated for three-dimensional cases, in future research.

Given the promising results obtained using this model, future work will focus on the extension of this study to the long-prismatic growth regime to cover the entire spectrum of habits exhibited by snowflakes. Effects from local variations in temperature will also be added to the model [109] to have a better image of the mechanisms behind the growth of snowflakes.

Chapter 7

Modeling mandelic acid crystallization [1]

Contents

[1] Part of this chapter has been published in

- **Q. Tan**, S.A. Hosseini, A. Seidel-Morgenstern, D. Thévenin, and H. Lorenz. Thermal effects connected to crystallization dynamics: a lattice Boltzmann study. *International Journal of Multiphase Flow*, 171:104669, (2024).
- **Q. Tan**, S.A. Hosseini, A. Seidel-Morgenstern, D. Thévenin, and H. Lorenz. Mandelic acid single-crystal growth: Experiments vs numerical simulations. *Communications in Computational Physics*, 33, 77-100 (2023).

7.1 Introduction

Mandelic acid is an aromatic alpha-hydroxy acid, with formula $C_8H_8O_3$. It is a white crystalline powder that is soluble in water and most common organic solvents. It has a density of 1.3 g/cm^3 and molecular weight of 152.5 g/mol. It is particularly important in the pharmaceutical industry for the organic synthesis of pharmaceutical components. For instance an ester of mandelic acid is essential to produce homatropine, used in eye drops as both a cycloplegic and mydriatic substance. In addition, it is also popular in the production of face peeling components [110], urinary tract infection treatments [111], and for oral antibiotics [112]. In toxicological studies, the concentration of styrene or styrene oxide is quantified by converting it into mandelic acid.

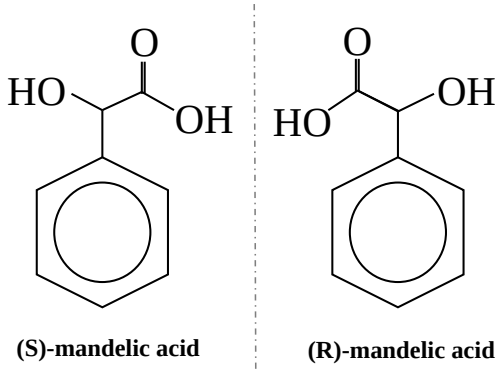

Figure 7.1: Molecular structure of mandelic acid enantiomers.

Mandelic acid exists in two enantiomeric forms as shown in Fig. 7.1, (S)- and (R)- mandelic acid. Most practical applications require the enantiopure form [111]. Amongst the different approaches to separate enantiomers, crystallization process such as classical resolution and preferential crystallization approaches are frequently used [113]. In such separation processes, the properties of the crystalline products such as crystal size and shape are largely determined by the growth process, which in turn depends on the crystallization conditions. In the pharmaceutical industry, the resulting crystal morphology is often of great importance, since it influences the rate of dissolution and the absorption of drugs. Compressibility, hardness, and flow properties of the drug are also strongly dependent on the crystal form [114]. Accurate investigations regarding crystal growth are difficult because the growth process varies greatly even under similar conditions: *crystal growth dispersion* is the term used to describe the fact that crystals, although initially of same shape and size, can rapidly grow differently even under the same growth conditions [115,116]. The main reason for these growth differences is probably related to minute tensions and deformations, leading in turn to minimal structural differences [117]. Other reasons are accidental deposits, or deposits of foreign bodies on the growing crystals' surface, which lead to incorporation into the

crystal and ultimately different growth. A proper understanding of growth conditions and their effect on the final product is therefore essential to design and scale-up production units for enantiopure substances.

A lot of experimental studies have been conducted concerning crystallization-based enantioseparation process including growth kinetics of mandelic acid, e.g. [113, 115, 118–123]. However, numerical studies regarding crystal habit and size of enantiopure S-mandelic acid remain scarce. The phase-field method has been shown in general to be a powerful tool for modeling structural evolution of materials and crystals. It is now widely used for modeling solidification [124, 125] and grain growth [10, 126–128]. The phase-field approach has also been used in the context of the lattice Boltzmann method, now widely recognized as an efficient alternative to classical tools, to simulate solidification processes [1, 56, 129–133]. This approach can reproduce numerically the solid-liquid interface interactions and the hydrodynamic effects affecting the habits of growing crystals [18, 53, 134–137].

In this chapter, we study the growth of a single (S)-mandelic acid crystal under different conditions (supersaturation, initial crystal size, flow rate, temperature) with a previously developed and validated LB-based numerical model (see chapter 4). All simulations presented here are carried out using the in-house solver ALBORZ [138]. The experimental setup is described in Sec. 7.2. The remaining part of the chapter is systematically organized into two distinct sections:

1. In Sec. 7.3, a LB simulations are carried out to model crystallization dynamics of (S)-mandelic acid using PF, species conservation, and NS equations. After validating the numerical procedure in a standalone manner via a self-convergence test, it is used to model the growth of a single (S)-mandelic acid rhombic seed at temperature and supersaturation corresponding to experimental settings; this provides a further, independent validation of the numerical model. The solver is then used to investigate the effect of different parameters such as supersaturation and initial seed size on crystal growth. Finally, a detailed study of the interaction between forced convection and crystal growth is presented. Analyzing the results, a simple solution is proposed to improve symmetrical growth under natural convection in the single-crystal cell used for all experimental investigations.

2. In Sec. 7.4, the crystal growth of (S)-mandelic acid is studied in detail using a hybrid lattice Boltzmann/finite-difference method under different reaction conditions and taking into account temperature difference changes; additionally, possible convection (sometimes also called ventilation) effects will be considered. The treatment of species/energy equations is based on the FD method, while the PF and NS equations are adeptly handled using the LBM. Distinct from the investigations presented in Sec. 7.3, the enthalpy production due to mandelic acid lattice integration is included in the model and an energy balance equation is solved

in the whole domain; in this manner, the effects of possible temperature gradients within the crystallizer are fully taken into account. In companion experiments, well-characterized seed crystals must be produced from supersaturated aqueous (S)-mandelic acid solutions. The single grain growth is then tracked, the growing crystal being inserted into a dedicated measurement cell. For the present section focusing on thermal effects: (i) the growth rate of the crystal was investigated for different crystallization temperatures in the growth cell; (ii) numerically, heat generation is taken into account at the crystal interface and temperature changes are solved for within the entire growth cell. Finally, (iii) the impact of convection effects on crystal habit is studied at different Reynolds numbers. Baffles are additionally placed in the cell to support symmetrical crystal growth.

7.2 Experimental setup

Experimental data for the growth rates have been obtained in the single-crystal growth cell [121, 139] illustrated in Fig. 7.2. The supersaturated aqueous solution of mandelic acid is pumped into a constant-temperature cylindrical crystallization cell, with solution temperatures varying between 20 and 30 °C. The temperature within the cell is maintained constant via a water-based cooling/heating system connected to a Pt-100 sensor monitoring the temperature inside the cell. Vessel 2, denoted V2 in Fig. 7.2b contains a saturated solution at temperature T_2 while vessel 1 (V1) was set to a lower temperature T_1, corresponding to the temperature of the cell. To create the supersaturated solution, the initially saturated solution in V2 is pumped into V1 and cooled down to T_1 before entering the growth cell. This effectively allows to control the supersaturation level of the incoming solution by choosing temperature T_1. In the present case, the supersaturation is defined as [140]:

$$U = \frac{C_{sat,2} - C_{sat,1}}{C_{sat,1}} \tag{7.1}$$

To start the experiment, the supersaturated solution is continuously pumped from vessel 1 to the growth cell, in which a single (S)-mandelic crystal is glued on the pin head of a crystal holder. Then, the solution is recycled to vessel 2 and the concentration of the solution is compensated. In that way, a stable degree of supersaturation is guaranteed during the whole process. A microscope with camera (Stemi2000C, company Carl Zeiss) is used to take pictures of the single crystal at every one hour. The images are afterwards post-processed by applying Carl Zeiss' Axio Vision software [121].

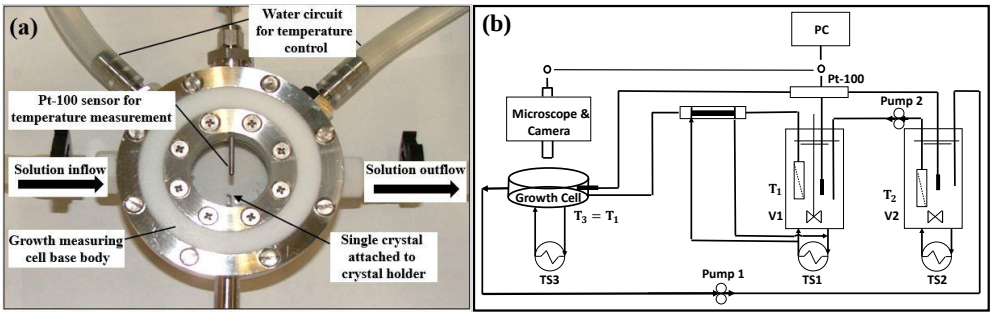

Figure 7.2: Single-crystal growth cell used for all experiments: (a) photograph; (b) Schematic diagram of experimental arrangement for the measurement of growth rate of a single crystal [121, 139]

.

In the experimental setup, small temperature differences and gradients cannot be measured, since this quantity is measured at a single point. Due to this fact it is interesting to analyze the temperature field within the entire growth cell numerically, as done in Sec. 7.4.

7.3 Impact of various properties

7.3.1 Validation

7.3.1.1 Self-convergence of the numerical solver

Based on the experiments, the evolution of mandelic acid without enantiomers follows habits with hexagonal symmetry. First, before going into further validation steps against experimental results, we look into the convergence behavior of the numerical scheme. To that end growth simulations are conducted using the hexagonal anisotropy function that will be used for the remainder of this chapter, starting with a rhombic initial seed. The seed is placed at the center of a fully periodic rectangular domain, with a length of 31 and a width of 26 mm. The perimeter of the initial rhombic crystal is 6.9 mm and the initial supersaturation is set to $U = 0.06$. Simulations are conducted using four different spatial resolutions, $\delta x \in \{0.04, 0.025, 0.02, 0.0125\}$ mm. Since the overall size of the numerical domain is kept fixed, an improved spatial resolution automatically comes with a larger number of grid points.

The highest resolution simulation with 2480 $\times$ 2080 points is used as reference to compute relative errors at the three lower spatial resolutions. The l^2 relative error norm is calculated based on the ϕ-profiles plotted along the x-direction on the centerline starting from the center of the domain (0,0) in positive x-direction until point (4 mm,0). The corresponding profiles along with

the crystal shape obtained after 16 hours are shown in Fig. 7.3. The l^2 norm is defined as:

$$\mathrm{E}_{l^2} = \sqrt{\frac{\sum_i \left(\phi_i - \phi_{ref,i}\right)^2}{\sum_i \phi_{ref,i}^2}} \tag{7.2}$$

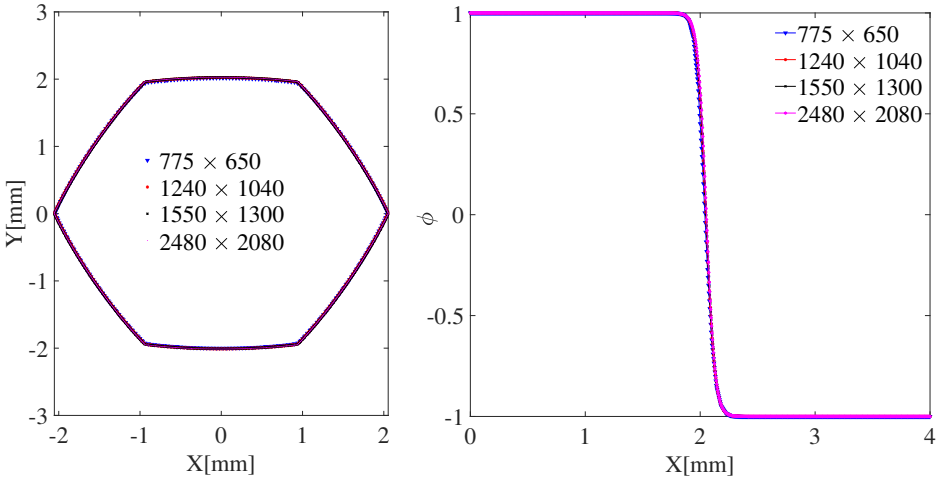

Figure 7.3: Left: $\phi = 0$ iso-contour, showing the boundary of the solid crystal (only the central part of the numerical domain is shown) after 16 hours; Right: Evolution of function ϕ in space along the line joining the center of the domain at (0,0) and point (4 mm,0) for $U = 0.06$ at increasing spatial resolution (grids with 775 × 650, 1240 × 1040, 1550 × 1300, and 2480 × 2080 points, respectively).

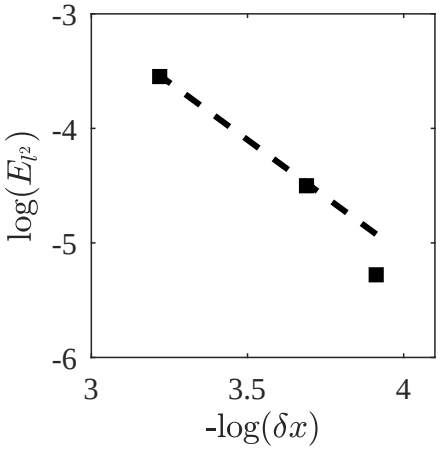

Figure 7.4: Scaling of the l^2 norm of errors as obtained from the self-convergence study. Black markers represent error data from the simulations while the black dashed line shows the theoretical -2 slope.

where ϕ represents a lower resolution and ϕ_{ref} denotes the highest resolution (used as reference). The errors obtained from the different simulations are illustrated in Fig. 7.4.

As observed from this plot, the numerical scheme is convergent as the error decreases with resolution. Furthermore, as expected from theoretical analyses, a second-order convergence is obtained in space.

7.3.1.2 Validation against experimental data

Next, to showcase the ability of the model to correctly reproduce the behavior of the real system, 2-D simulations are considered using the real reactor geometry. The simplification to two-dimensional simulations is justified by the fact that, in all conditions considered here, the crystal follows a platelet growth mode indicating clear separation of scales between growth in the axial and planar directions, in connection to a symmetry of the flow field [134]. The geometry used for the simulations is shown in Fig. 7.5. First, configurations are considered where forced convection is negligible. For all experiments presented in this section the initial seed is a rhombic crystal. Two different initial supersaturations are considered, namely $U = 0.06$ and $U = 0.11$ for the same temperature, $T = 20°\text{C}$. The diffusion coefficient of mandelic acid in the aqueous solution under the conditions considered here is $D = 4.273 \times 10^{-4}\text{mm}^2/\text{s}$ [141]. Based on the excellent agreement observed in the previous section, all simulations are conducted with a spatial resolution of $\delta x = 0.025$ mm. The interface thickness is set to $W_0 = 0.05$ mm, the relaxation time to $\tau_0 = 11$ s, and the coupling coefficient $\lambda = 3$ is chosen as a numerical parameter, consistently with the standard PF method for dendrite growth [11]. At the walls of the reactor, zero-flux boundary conditions are applied to both the species and phase fields via the anti-bounce-back scheme [63]. At the inlet a constant supersaturation is imposed.

Simulation results are compared to experiments and validated both qualitatively using the crystal shape, and quantitatively by comparing the growth rate.

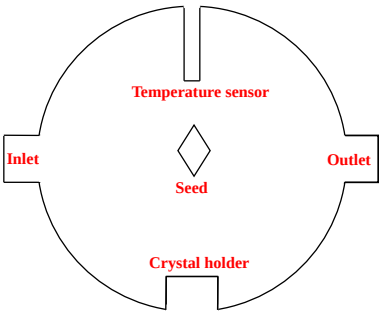

Figure 7.5: Reactor geometry employed for all simulations.

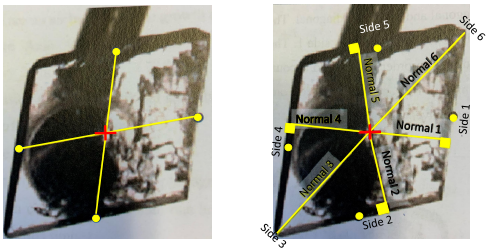

Figure 7.6: Method used to number the crystal sides and the associated normal directions [139].

To measure the crystal growth rate in both experiments and numerical calculations, the average length quantifying the crystal size is introduced following [139] as illustrated in Fig. 7.6:

- Connect opposite sides via their centers.
- Identify the crystal center as the intersection between those lines.
- Number the different sides as shown in Fig. 7.6.
- Compute the lengths of the corresponding normal distance from the center identified in the previous step (L_1, L_2, L_3, L_4, L_5 and L_6).
- The average normal length is simply defined as $L_{\text{avg}} = (L_1 + L_2 + L_3 + L_4 + L_5 + L_6)/6$.

The experiments are systematically conducted over a period of 12 hours. The average length is computed every hour and subsequently fitted with a linear function to extract an average growth rate $G_{th} = L_{avg}/t$, where t is the corresponding growth time during the crystallization process. The evolution of the crystal shape in both experiments and simulations are illustrated in Fig. 7.7 and 7.8.

A visual comparison regarding crystal shape and size over time for $U = 0.06$ points to a good agreement between experiments and simulations. For $U = 0.11$ only numerical results are shown since experimental snapshots are not available. To validate the results in a quantitative manner, the growth rates corresponding to the six different sides of the crystal for both supersaturations as obtained from experiments and simulations are compared in Table 7.1.

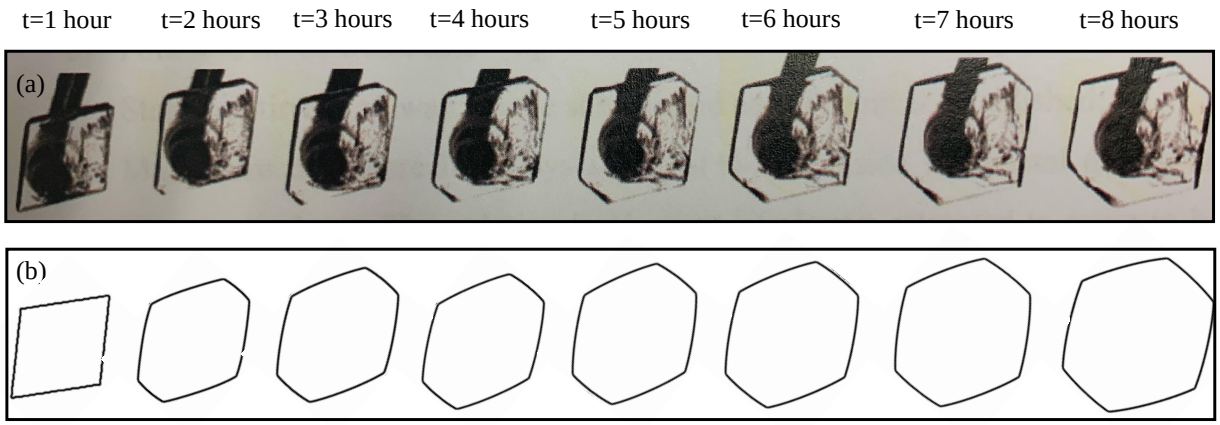

Figure 7.7: Contours of an (S)-mandelic acid crystal vs. time as obtained from (a) experiments [139] and (b) simulations. The supersaturation is $U = 0.06$ in both cases. The spatial scale is the same in all images, enabling a direct comparison.

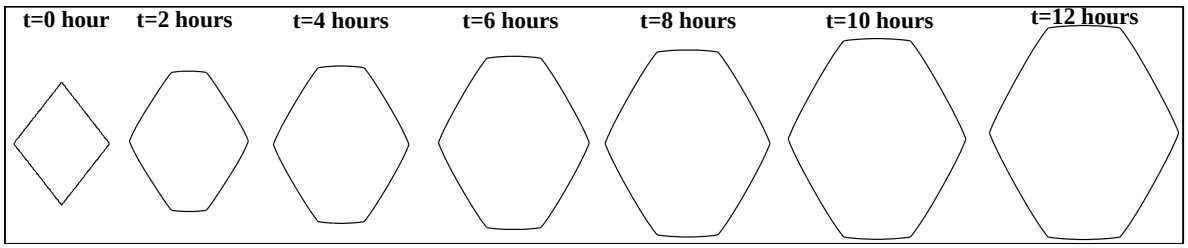

Figure 7.8: Contours of the (S)-mandelic acid crystal vs time as obtained from simulations for $U = 0.11$. No experimental image are available for this case.

R^2 is the coefficient of determination shown here to characterize the reliability of the linear regression used to extract growth rates. Representing the length of side i measured at time t in experiments as $L_i(t)$ and the value of the linear function as $L'_i(t)$ the coefficient is computed as:

$$R^2 = 1 - \frac{A_{\text{res}}}{A_{\text{tot}}}, \tag{7.3}$$

where the residual sum of squares is:

$$A_{\text{res}} = \sum_t \left(L_i(t) - L'_i(t)\right)^2, \tag{7.4}$$

and the total sum of squares is:

$$A_{\text{tot}} = \sum_t \left(L_i(t) - \overline{L_i}\right)^2, \tag{7.5}$$

Table 7.1: Comparisons between experiments and simulations for supersaturation $U = 0.06$ and $U = 0.11$ [139]

Cases	Experiments				Simulations	
Number	I		II		I	II
Supersaturation (%)	0.06		0.11		0.06	0.11
Seed perimeter (mm)	6.9		9.5		6.9	9.5
Parameter	Slope	R^2	Slope	R^2	Slope	Slope
Normal 1	0.07	0.99	0.14	0.98	0.08	0.14
Normal 2	0.09	0.97	0.14	0.94	0.08	0.14
Normal 3	0.00	0.10	0.00	0.50	0.01	0.02
Normal 4	0.06	0.94	0.06	0.78	0.08	0.14
Normal 5	0.03	0.92	0.08	0.86	0.08	0.14
Normal 6	0.00	0.20	0.09	0.93	0.01	0.02
Average growth rate G_{th} (mm/h)	0.06		0.10		0.057	0.10

where $\overline{L_i}$ represents the average over all data points.

A direct comparison of the growth rates for both values of U confirms the very good agreement between experimental observations and numerical simulations. For $U = 0.06$, the growth rate is numerically underpredicted by less than 6%. At $U = 0.11$, the relative difference is even reduced to 2%. This proves the ability of the numerical model to capture the growth of (S)-mandelic acid in a pure aqueous environment. At higher supersaturation, $U = 0.11$, the crystal experiences as expected a faster growth as compared to the lower supersaturation case, $U = 0.06$. It is interesting to take now a closer look into the effects of supersaturation on growth rate.

7.3.1.3 Impact of supersaturation on growth rate

In order to have a better understanding of the effect of supersaturation on crystal growth dynamics we keep a configuration similar to the previous one, but considering many more supersaturation values, $U \in \{0.06, 0.085, 0.11, 0.15, 0.2\}$. In all simulations presented in this section, the initial seed size and geometry follow that of configuration I in the previous section, see Table 7.1. The evolution of the crystal shape over time as obtained from these simulations are shown in Fig. 7.9.

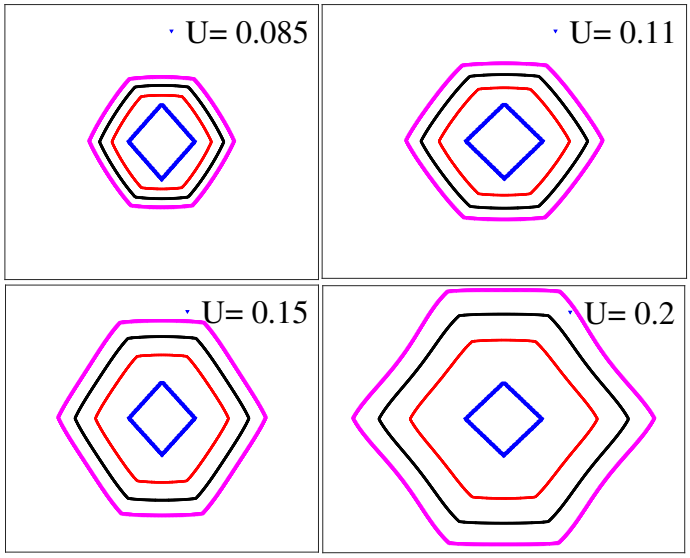

Figure 7.9: Boundaries of the single crystal of (S)-mandelic acid (iso-contours of $\phi = 0$) at time t=0 (blue), 4 (red), 8 (black), 12 hours (purple) as a function of supersaturation: (top-left) $U = 0.085$, (top-right) $U = 0.11$, (bottom-left) $U = 0.15$, and (bottom-right) $U = 0.2$.

Furthermore, the data representing average growth rate are listed in Table 7.2.

Table 7.2: Numerically observed averaged crystal growth rate as function of supersaturation between $U = 0.06$ and 0.2

Supersaturation(%)	0.06	0.085	0.11	0.15	0.2
Seed perimeter (mm)	6.9	6.9	6.9	6.9	6.9
Average growth rate G_{th} (mm/h)	0.057	0.0871	0.1136	0.1553	0.2093

As expected, higher supersaturations lead to faster crystal growth. It is worth noting that the average growth rate of the crystal can be very well approximated in the considered range as a linear function of supersaturation with slope one. Another parameter that has been observed experimentally to affect growth dynamics, especially during the early phase, is the initial seed size, better quantified via its perimeter. We will look into that effect in the next section.

7.3.1.4 Impact of initial size on growth rate

To quantify the effects of initial seed size, which is known to be sometimes important [115], a configuration with supersaturation $U = 0.06$ at crystallization temperature $T = 20°C$ has been

retained. Seeds with the same initial rhombic shape but different sizes have been simulated; the initial seed perimeters are $P \in \{6.9, 6.96, 8.4, 8.8\}$ mm, corresponding to available experimental data. The resulting growth rate data and parameters extracted from the experiments are listed in Table 7.3.

Simulations with exactly the same configurations have been conducted. The corresponding results are listed in Table 7.4.

Both experiments and simulations, while in fair agreement with each other, point to the fact that the average growth rate is only slightly affected by the initial seed size. The effect appears to be somewhat stronger for a larger initial seed. The growth behavior over time is illustrated in Fig. 7.10. The results for initial perimeters 6.9 and 6.96 mm cannot be differentiated visually. For a larger initial seed, the differences between 8.4 and 8.8 mm can be recognized, but only a minute increase in average growth rate can be recognized. It can be concluded that, compared to supersaturation, the influence of initial seed size is minor. Still, a larger initial seed corresponds to a slightly increased growth rate.

All the previous results have been obtained while neglecting any convection effect around the crystal. However, it is known that forced convection might lead to asymmetric crystal growth. This will be explored next.

Table 7.3: Impact of initial seed size in experiments with supersaturation $U = 0.06$ [139]

Experiment Number	I(1)		I(2)		I(3)		I(4)	
Perimeter (mm)	6.9		6.96		8.4		8.8	
Parameter	Slope	R^2	Slope	R^2	Slope	R^2	Slope	R^2
Normal 1	0.07	0.99	0.09	0.99	0.09	0.99	0.10	0.98
Normal 2	0.09	0.97	0.09	0.99	0.12	0.98	0.10	0.97
Normal 3	0.00	0.10	0.01	0.24	0.01	0.67	0.02	0.82
Normal 4	0.06	0.94	0.03	0.92	0.07	0.94	0.07	0.85
Normal 5	0.03	0.92	0.03	0.89	0.06	0.94	0.05	0.98
Normal 6	0.00	0.20	0.01	0.45	0.03	0.85	0.00	0.10
Average growth rate G_{th} (mm/h)	0.06		0.06		0.06		0.07	

Table 7.4: Impact of initial seed size in simulations with supersaturation $U = 0.06$

Simulation Number	I(1)	I(2)	I(3)	I(4)
Perimeter (mm)	6.9	6.96	8.4	8.8
Parameter	Slope	Slope	Slope	Slope
Normal 1	0.08	0.08	0.082	0.082
Normal 2	0.08	0.08	0.082	0.082
Normal 3	0.01	0.01	0.012	0.016
Normal 4	0.08	0.08	0.082	0.082
Normal 5	0.08	0.085	0.085	0.082
Normal 6	0.01	0.01	0.012	0.015
Average growth rate G_{th} (mm/h)	0.0567	0.0575	0.0592	0.0598

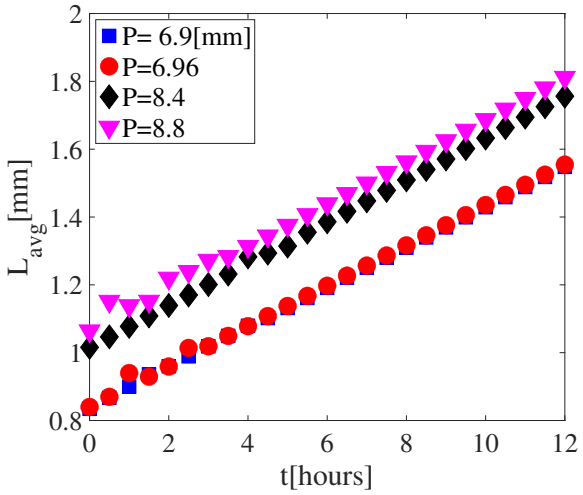

Figure 7.10: Numerical results concerning the effect of initial seed perimeter on the growth rate.

7.3.2 Ventilation effects

In the real single-crystal reactor the incoming flow of (S)-mandelic acid in water might have a large impact on crystal growth rate and shape development. The aim of the present section is to check and quantify this point.

Validation in presence of convection First, we validate the numerical model against available experimental data taking into account the real inflow conditions used in the reactor cell. For this purpose, and following the experimental settings [142], a hexagonal seed of perimeter $P = 3.7$ mm is used. The initial supersaturation is $U = 0.045$, the Reynold number Re = 17.2. Here, we keep the same Reynold number as the experiment [142]. The results, represented by the crystal shape, are compared over time via snapshots taken every two hours over an overall growth period of 16 hours, as shown in Fig. 7.11.

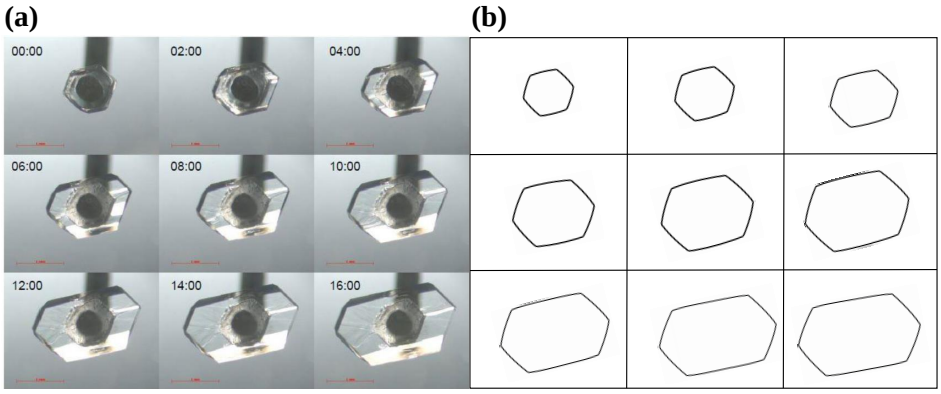

Figure 7.11: Morphologies of (S)-mandelic acid crystal captured by (a) camera during the experiments [142]; (b) simulations.

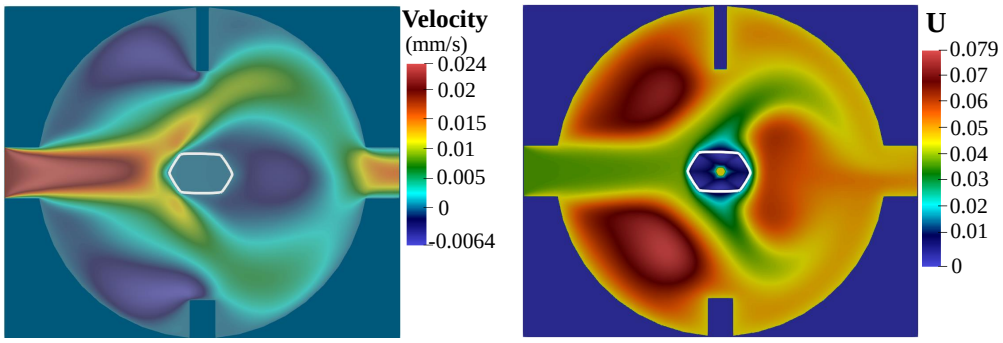

Figure 7.12: Non-symmetric growth of a (S)-mandelic acid crystal taking into account convection as obtained from the simulation for $U = 0.045$ after 16 hours. Flow is from left to right in the reactor.

It is observed that the evolution of the crystal shape over time as obtained from both experiment and simulation are in good agreement with each other; they both point to a non-symmetrical growth. The constant inflow of a solution with a higher concentration hitting the inlet-facing sides of the crystal subjects them to noticeably larger gradients at the interface, as compared to the other, leeward sides; this induces lower adsorption rates at the latter. As a result the (S)-mandelic crystal

grows faster on the sides facing the inflow, leading to a steady increase of the aspect ratio, defined as the ratio of the horizontal size of the crystal to its vertical size. This is clearly visible in Fig. 7.12 where both the velocity and supersaturation fields at t =16 hours are shown.

To further illustrate the effects of hydrodynamics on the crystal habit, the effect of the Reynolds number and of the initial orientation of the seed are considered numerically.

Effect of Reynolds number For this purpose, the supersaturation is kept constant at $U = 0.045$. The Reynolds number is the most important non-dimensional parameter of fluid dynamics, comparing quantitatively convective effects to dissipation by viscosity. It is defined as:

$$\mathrm{Re} = \frac{u_{\mathrm{in}} P}{\nu_f}, \tag{7.6}$$

where P is the initial seed perimeter. Two different Reynolds numbers, i.e. Re= 8.6 and 17.2, are considered. The obtained crystal shape and velocity fields are shown in Fig. 7.13.

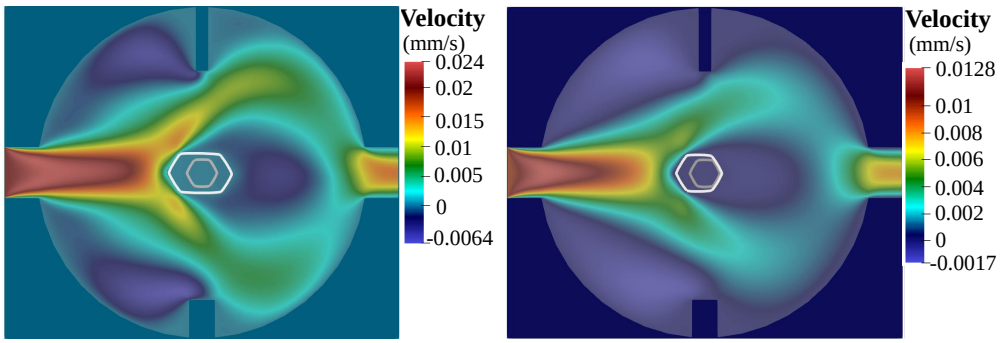

Figure 7.13: Convection effects on (S)-mandelic acid crystal growth after 10 hours for $U = 0.045$ and two different Reynolds numbers. Left side: Re = 17.2; Right side: Re = 8.6. The white line represents the crystal boundary taking into account the flow (ventilation effect), while the grey line shows the same results in the absence of any inflow.

As expected, higher inlet velocities hitting the inflow-facing sides of the crystal result in a faster growth in that direction; the resulting asymmetry becomes more marked, leading to elongated crystals in the horizontal direction for the present setup. This is particularly clear looking at Fig. 7.14. After 10 hours, the aspect ratio for Re= 17.2 is already more than twice as large than for Re= 8.6.

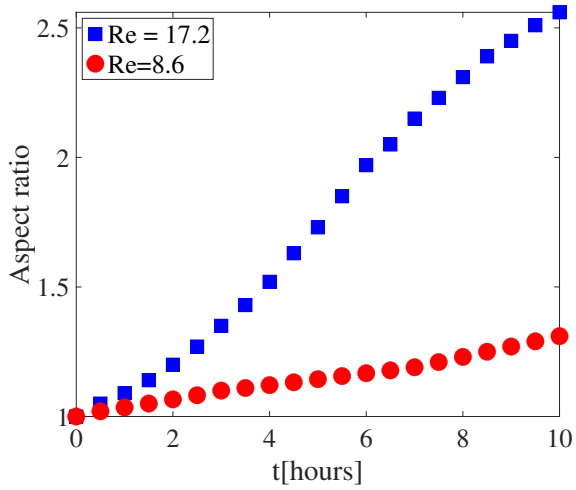

Figure 7.14: Evolution of the aspect ratio vs. time for Reynolds numbers Re= 8.6 and 17.2.

Effect of the initial orientation of the seed To show the effect of seed orientation, four simulations have been carried out with the same Reynolds number, Re= 17.2, but with different initial orientations, namely $\theta \in \{0, \frac{\pi}{12}, \frac{\pi}{6}, \frac{\pi}{4}\}$. This choice of tilt is motivated by the six-fold symmetry of the crystal natural habit, so that only the 0-$\pi/3$ range is relevant. The obtained crystal habits after 10 hours along with the corresponding velocity fields are illustrated in Fig. 7.15.

It is seen that the initial orientation not only affects the symmetry of the crystal, but also its average growth rate. Taking into account convective effects and initial seed orientation, the crystal habits become highly asymmetrical. It is also observed that a slight initial rotation in clockwise direction can result in a final habit showing preferential counter-clockwise orientation, due to a strong interaction with the convective flow field.

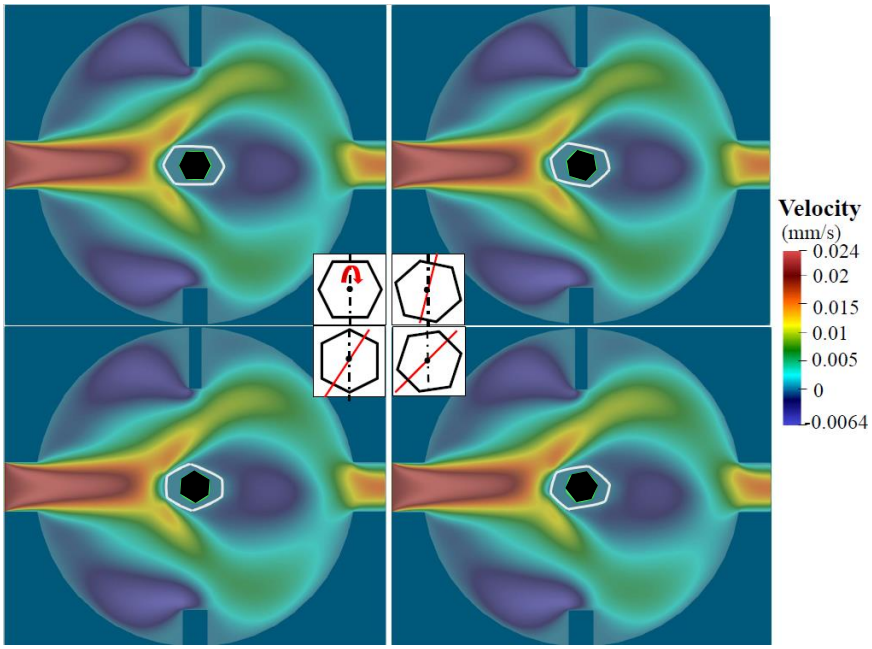

Figure 7.15: Effect of initial seed orientation on (S)-mandelic acid crystal growth after 10 hours for $U = 0.045$. Top left: without rotation; Top right: initial rotation of $\frac{\pi}{12}$ (clockwise rotation); Bottom left; initial rotation of $\frac{\pi}{6}$; Bottom right: initial rotation of $\frac{\pi}{4}$. The white line represents the crystal boundary taking into account the flow, while the black color shows the same results in the absence of any inflow.

Improving symmetrical growth in presence of convection using a baffle As seen from the previous simulations, the overall shape of the crystal varies considerably as function of the Reynolds number. It was mentioned earlier that the regularity of the crystal shape is a property of high interest regarding the final products performance. Therefore, it is desirable to find a simple geometrical modification to the single-crystal growth cell leading to isotropic growth rates and a desired final aspect ratio. For this purpose, a simple flat baffle has been placed in the simulation directly in front of the inlet in order to prevent a direct impact of the incoming flow onto the growing seed. Three different configurations (different position, different size) of the baffles have been compared. The resulting configurations are illustrated in Fig. 7.16; configuration 1 is the original case, without any baffle.

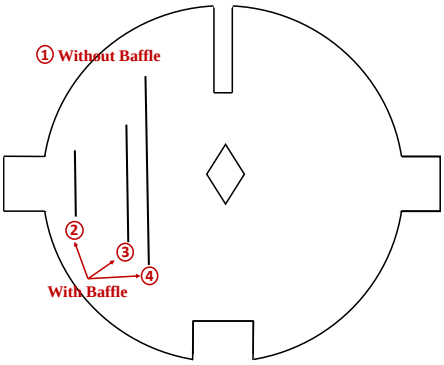

Figure 7.16: Proposed modifications of the geometry of the single-crystal growth cell reactor including a baffle (three different possible configurations).

To check the robustness of the proposed modification with the three different baffles (plus the original case), two different Reynolds numbers (Re= 8.6 or 17.2), and two different initial seed orientations (θ=0 or $\pi/6$) have been considered, making up for a total of ($4 \times 2 \times 2 =$) 16 different cases. All numerical results after 10 hours of growth are shown in Figs. 7.17 (for Re=17.2) and 7.18 (for Re= 8.6).

To quantify the effects of the baffles on the quality of the crystal, a quality parameter is defined as $Q = \max(L_i)/\min(L_i)$ where index $i \in \{0,\ldots,5\}$ covers the length of all sides of the resulting crystal. Parameter Q quantifies non-isotropic growth, with $Q = 1$ (the minimum value) corresponding to a perfectly isotropic growth, while an increasing value of Q corresponds to growing non-isotropy. The values of crystal quality as obtained from all simulations after 10 hours of growth are listed in Table 7.5.

From Table 7.5 it is clearly observed that, while all baffles contribute to reducing asymmetrical growth, the larger one, i.e. baffle 3, leads to the best crystal quality in terms of symmetry for all considered conditions. It successfully reduces deviations from perfect symmetry by about 20% for Re= 8.6 and 30% for Re= 17.2. Since the complexity of the experimental setup would not be significantly increased by adding a baffle, such a modification is recommended for further studies.

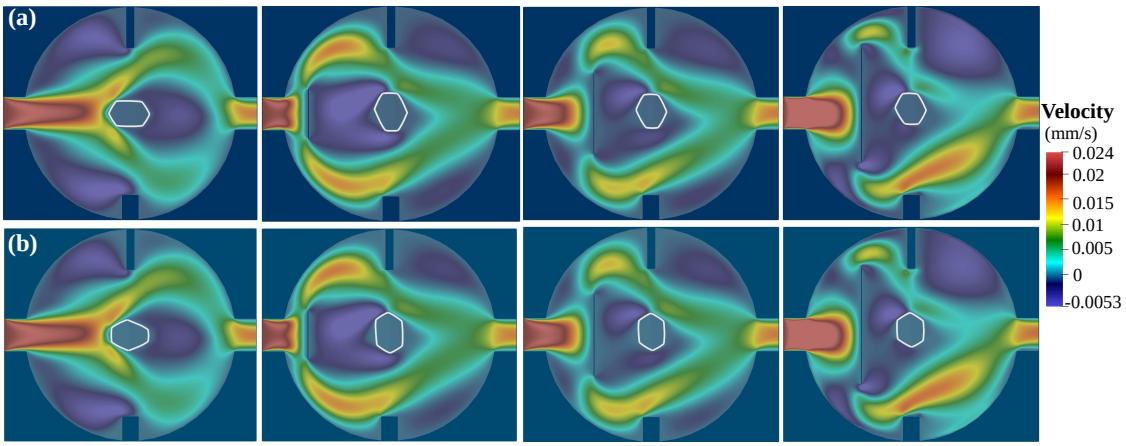

Figure 7.17: Numerical prediction for the growth on (S)-mandelic acid crystal after 10 hours for $U = 0.045$ and Re$=$ 17.2. First column: original configuration, without baffle; second column: baffle configuration 2; third column: baffle configuration 3; fourth column: baffle configuration 4. Top line (a): without any rotation of the initial seed; Bottom line (b): with initial rotation of the seed by $\pi/6$.

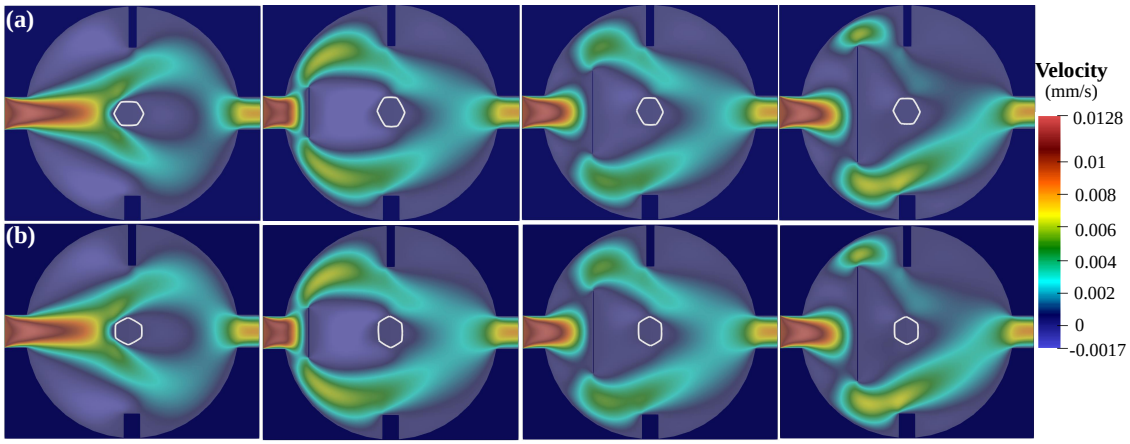

Figure 7.18: Numerical prediction for the growth on (S)-mandelic acid crystal after 10 hours for $U = 0.045$ and Re$=$ 8.6. First column: original configuration, without baffle; second column: baffle configuration 2; third column: baffle configuration 3; fourth column: baffle configuration 4. Top line (a): without any rotation of the initial seed; Bottom line (b): with initial rotation of the seed by $\pi/6$.

Table 7.5: Impact of the baffles for $U = 0.06$ for two different Reynolds numbers and seed orientations in Fig. 7.16

Q	Re=8.6; tilt=0	Re=8.6; tilt=π/6	Re=17.2; tilt=0	Re=17.2; tilt=π/6
No Baffle	1.28	1.23	1.625	1.59
Baffle 1	1.22	1.21	1.41	1.39
Baffle 2	1.13	1.16	1.24	1.21
Baffle 3	1.05	1.07	1.14	1.12

7.4 Effect of temperature

Crystallization is widely used for the separation of enantiomers relying on classical resolution, or preferential crystallization approaches [113]. During crystallization, essential properties of the crystalline products (e.g., purity, shape, sizes [143]) are determined by the growth process, which again depends on the conditions within the crystallizer. The reaction conditions, such as supersaturation, temperature, other components possibly present in the solution (impurities, additives) play a central role for crystal growth. Many experimental studies have been conducted concerning crystallization-based enantio-separation processes. Of particular interest for the present work are measurements regarding growth kinetics of mandelic acid, e.g. [113, 115, 118–123]. Most of the studies carried out up to now relied on the assumption of a perfectly homogeneous temperature during crystallization. Typically, experimental temperature measurements rely on a single sensor (point measurement), so that possible temperature gradients could not be tracked. Since only small temperature differences are expected, experimental investigations regarding temperature effects during crystal growth would be challenging and costly.

Numerical simulations using accurate and efficient algorithms can in this case complement or replace such experiments and provide corresponding answers. In recent years, much effort has been put on developing mathematical models and numerical algorithms suitable for describing crystal habit and size of crystals [1, 10], also for enantiopure (S)-mandelic acid [137, 144]. The PF method has become one of the most popular approaches to simulate crystal growth. It is a powerful tool for modeling structural evolution of materials and crystals [131, 132, 145]. It is now widely used to investigate solidification [124, 125] and grain growth [10, 126–128]. The PF approach has also been used in combination with the LBM, now widely recognized as an efficient alternative to classical tools, to simulate solidification processes [1, 56, 129, 130, 133]. This approach can reproduce numerically the solid-liquid interface interactions and the hydrodynamic effects affecting the habits of growing crystals [53, 134–137, 144]. While widely used in the literature for hydrody-

namic simulations the LBM is known to suffer from Gibbs-type oscillations near sharp interfaces and instability issues in the limit of vanishing diffusion coefficients. Furthermore, the classical passive-scalar LB solvers can not take into account flows with variable density and/or specific heat capacity. For such flows the models need to be extended, see for instance [109]. In such cases an interesting alternative is to replace the solvers for the scalar fields, e.g. species and temperature, with classical FD solvers with discontinuity-capturing schemes for the advection term. The corresponding FD solvers are then coupled to a LB approach for describing hydrodynamics. Such hybrid approaches have been increasingly used in the past years for applications such as combustion, see for instance [48, 49, 146].

The single grain growth is then tracked, the growing crystal being inserted into a dedicated measurement cell. The thermo-physical properties of the mandelic acid at temperature $T = 298.15$K is evaluated in Sec. 7.4.1; The FD solver is validated in Sec. 7.4.2. Finally, temperature and convection effects on crystal habit are studied at different Reynolds numbers. Baffles are additionally placed in the cell to support symmetrical crystal growth in Sec. 7.4.3.

7.4.1 Evaluation of thermo-physical properties

Table 7.6: Physical parameters used for modeling single S-ma crystal growth at temperature of 25°C.

Property	Value	Unit	Ref.
Enthalpy of crystallisation ΔH_{cryst}	-18.5	kJ/mol	[147]
Specific heat capacity for solid $c_{p,S}$	160.5	J/mol · K	[148]
Specific heat capacity for liquid $c_{p,L}$	75	J/mol · K	[148]
Thermal diffusivity for solid κ_S	1.1	mm^2/s	[149]
Thermal diffusivity for liquid κ_L	0.146	mm^2/s	[150]
Diffusion coefficient in liquid D	1.2×10^{-3}	mm^2/s	[151]
Crystal growth rate constant k_0	1.0×10^{-5}	cm/s	[152]
Density of solid ρ_S	1.341	g/cm^3	[153]
Density of fluid ρ_L	1.0	g/cm^3	[154]

The physical parameters of the pure (S)-mandelic acid at temperature T = 298.15K (or 25 °C) are listed in Table 7.6. The enthalpy of crystallisation ΔH_{cryst} characterizes the energy difference per

mole of S-ma between the solid and liquid (melt) phase and is represented here as negative value of the enthalpy of fusion [147]. The value of specific heat capacity $c_{p,L}$ is that of water (being by far the dominating component) and $c_{p,S}$ is for racemic MA [148]. Furthermore, κ_S denotes the thermal diffusivity of the crystal and κ_L represents the thermal diffusivity of water [149, 150], while D is the diffusion coefficient for the solution [151].

7.4.2 Validation of the FD solver

In the present part, the FD method is adopted to solve for energy and species due to the large ratio between the value of thermal diffusivity and of mass diffusion coefficient; the corresponding Lewis number (the ratio between thermal diffusivity and mass diffusion) is of the order of $10^2 - 10^3$. FDs are more suitable for low values of the diffusion coefficient, since LBM becomes numerically unstable at very low non-dimensional diffusion coefficients, the relaxation time τ becoming close to 0.5.

7.4.2.1 Self-convergence of FD method

As known, LBM is of second-order accuracy for the phase-field model [144]. Here, the accuracy of the finite-difference method is checked by considering only diffusion for a case with non-homogeneous concentrations. In this test-case, periodic boundaries are implemented in a 2D box of size $[-1,1]\times[-1,1]$mm.

The concentration profile is set as a Gaussian hill at $t = 0$ following the analytical solution for this problem [63, 65]:

$$C(\mathbf{x},t) = \frac{\Psi_0}{2\pi\sqrt{|\boldsymbol{\sigma_t}|}}\exp\left(-\frac{1}{2}\boldsymbol{\sigma_t}^{-1} : \mathbf{x}^2\right). \tag{7.7}$$

where $\Psi_0 = 2\pi\sigma_0^2$ with initial variance $\sigma_0 = 0.01$mm. The tensor $\boldsymbol{\sigma_t} = \sigma_0^2\mathbf{I} + 2t\mathbf{D}$, $|\boldsymbol{\sigma_t}|$ is the determinant value and $\boldsymbol{\sigma_t}^{-1}$ is inverse matrix of $\boldsymbol{\sigma_t}$, respectively. Quantity $\mathbf{I}$ is the unit matrix. Note that σ_0 is small enough in the present case, so that periodic boundary conditions are suitable.

The diffusion tensor is written in 2D:

$$\mathbf{D} = \begin{bmatrix} D_{xx} & D_{xy} \\ D_{yx} & D_{yy} \end{bmatrix}. \tag{7.8}$$

Therefore, $\boldsymbol{\sigma_t}$ is:

$$\boldsymbol{\sigma_t} = \begin{bmatrix} \sigma_0^2 + 2tD_{yy} & 2tD_{yx} \\ 2tD_{xy} & \sigma_0^2 + 2tD_{xx} \end{bmatrix}. \tag{7.9}$$

Here, the diffusion coefficient is set by: $D_{xy} = D_{yx} = 0$, $D_{xx} = D_{yy}$. The simulations are conducted using four different spatial resolutions, $\delta x \in \{0.04, 0.025, 0.02, 0.016\}$mm. Since the overall size of the numerical domain is kept fixed, an improved spatial resolution automatically comes with a larger number of grid points. Then, the results are compared with the analytical solution (see Eq. (7.7)) at time $t = 10$ s.

The l^2 relative error norm is calculated based on the concentration profiles over the entire domain. The l^2 norm is defined as:

$$\mathrm{E}_{l^2} = \sqrt{\frac{\sum_i (C_i - C_{an,i})^2}{\sum_i C_{an,i}^2}} \tag{7.10}$$

where C_i represents the concentration obtained numerically at a certain position in the box and C_{an} denotes the analytical solution from Eq. (7.7). The errors obtained from the different simulations are illustrated in Fig. 7.19.

Table 7.7: Relative l^2 errors of the scalar variable C for different resolutions

Numerical grid	50×50	80×80	100×100	125×125
E_{l^2}	5.0565	0.1787	0.0193	0.0081

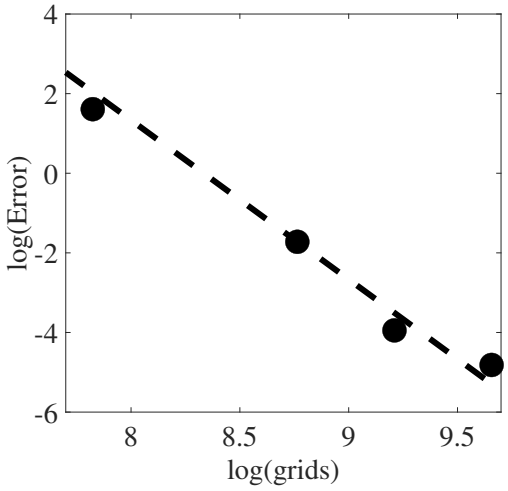

Figure 7.19: Scaling of the l^2 error norm as obtained from the grid convergence study. Black markers represent error data from the simulations (see Table 7.7) while the black dashed line displays the theoretical -4 slope.

As observed from this plot, the numerical scheme is convergent as the error decreases with

resolution. Furthermore, as expected from theoretical analyses, a fourth-order convergence is obtained for the finite-difference solver.

7.4.2.2 Limiting case: adiabatic single-crystal growth cell

In this section, in order to get rough insight regarding the possible temperature range, an adiabatic single-crystal growth cell is computed using mass and energy conservation for the purpose of verifying the proper function of the hybrid LBM/FD solver for describing single S-ma crystal growth rate and temperature within the cell.

The model is based on a square box in 3D (see Fig. 7.20) with a side length of 1 cm. The seed is set in the center of the box with initial radius R = 0.1 cm. The initial concentration of the supersaturated aqueous S-ma aqueous solution is 0.887 mmol/cm^3 in this closed adiabatic system. The S-ma crystal keeps growing until the solution concentration reaches equilibrium.

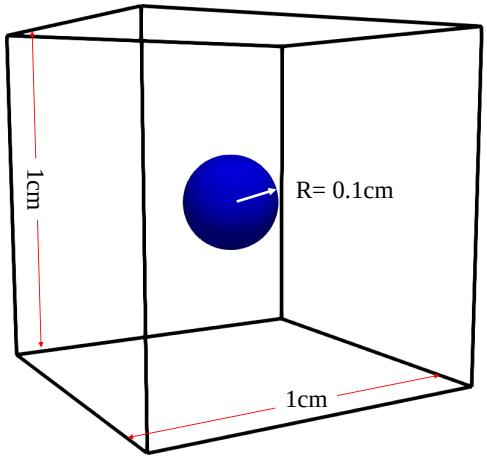

Figure 7.20: Schematic of adiabatic cell box in 3D.

The liquid phase mass balance involving liquid phase concentration c reads:

$$V_L \frac{\partial c}{\partial t} = -k(T) A_{solid} (c - c_{sat}(T)) = -k(T) 4\pi R^2 (c - c_{sat}(T)) \tag{7.11}$$

where V_L is the volume of the adiabatic box (here, 1 cm^3); variable $A_{solid} = 4\pi R^2$ is the surface area of the solid; $V_{solid} = \frac{4}{3}\pi R^3$ is its volume; $c_{sat}(T)$ is the saturation concentration (see Eq. (7.16)) and $k(T)$ the growth rate constant (see Eq. (7.17)), both at temperature T. The ordinary differential equation describing the liquid phase concentration c is:

$$\frac{\partial c}{\partial t} = -\frac{k(T)}{V_L} 4\pi R^2 (c - c_{sat}(T)) \tag{7.12}$$

The solid phase mass balance reads (assuming that the density does not depend on temperature, since temperature differences are expected to be low):

$$\rho_S \frac{\partial V_S}{\partial t} = \rho_S 4\pi R^2 \frac{\partial R}{\partial t} = k(T) 4\pi R^2 (c - c_{sat}(T)) \tag{7.13}$$

where ρ_S is the density of the mandelic acid crystal. The second ordinary differential equation describing radius is:

$$\frac{\partial R}{\partial t} = \frac{k(T)}{\rho_S}(c - c_{sat}(T)) \tag{7.14}$$

The third ordinary differential equation representing energy (here in the form of temperature) is:

$$\frac{\partial T}{\partial t} = -\frac{\Delta H_{cryst}}{V_L \rho_L c_{p,L} + \frac{4}{3}\pi R^3 \rho_S c_{p,S}} k(T) 4\pi R^2 (c - c_{sat}(T)) \tag{7.15}$$

The value of specific heat capacity $c_{p,L}$ is that of water, and $c_{p,S}$ is from the S-mandelic acid, taken from [148]. The saturation function for a mandelic acid aqueous solution is [155]:

$$c_{sat}(T) = -0.005006 + 0.00001923T \tag{7.16}$$

where temperature T with unit K and the kinetic growth rate constant is:

$$k(T) = k_0 e^{-E/(RT)} \tag{7.17}$$

where k_0 is the crystal growth rate constant with the unit [cm/s]; E is the activation energy, with unit [J/mol]. Due to the small temperature range covered, the growth rate coefficient $k(T)$ was assumed to be constant in the temperature range between 20 and 30 °C. The value used is given in Table 7.6.

In the numerical simulation based on the hybrid LBM/FD solver, the spatial discretization is 0.01 cm (leading to a grid [100 × 100 × 100]) and the time-step is 0.005 s. The physical parameters of S-ma are selected based on Table 7.6.

Fig. 7.21 shows average concentration, crystal radius, and average temperature as function of time. It can be observed that the numerical solution obtained with the hybrid LBM/FD solver matches well with the analytical solutions derived from mass and energy conservation.

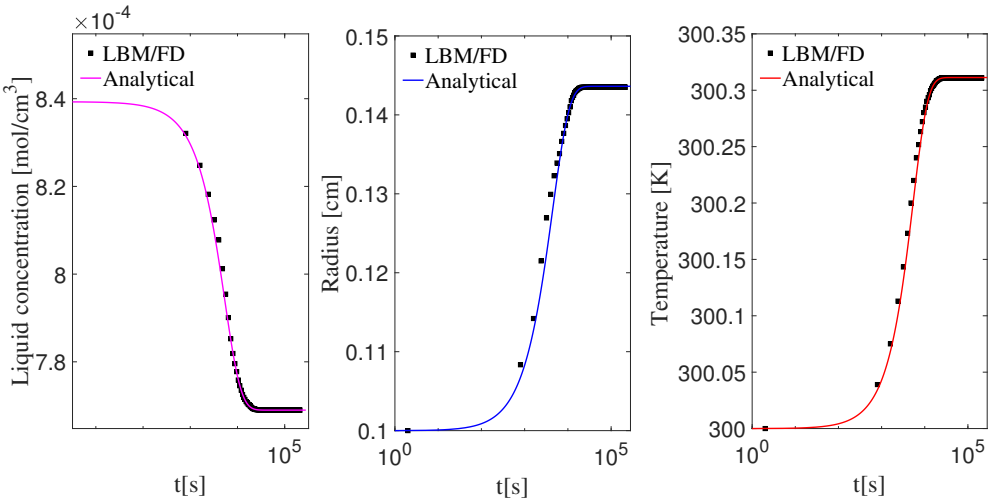

Figure 7.21: Plots showing average concentration (left), crystal radius (center) and average temperature (right) as function of time as obtained from the hybrid LBM/FD solver (symbols) compared with analytical solution (lines). Note the horizontal logarithmic scale due to the long duration of the process.

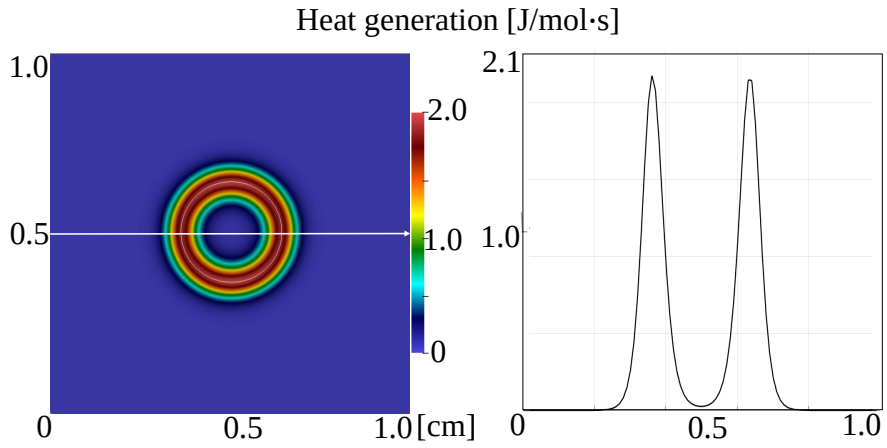

Figure 7.22: Molar heat generation during growth of spherical crystal at time $t = 1$ hour.

Fig. 7.22 and 7.23 illustrate the heat release process during phase-change from the liquid into the solid state at the interface of the crystal. Eventually, the heat release is stopped when the crystal stops growing (equilibrium state has been reached).

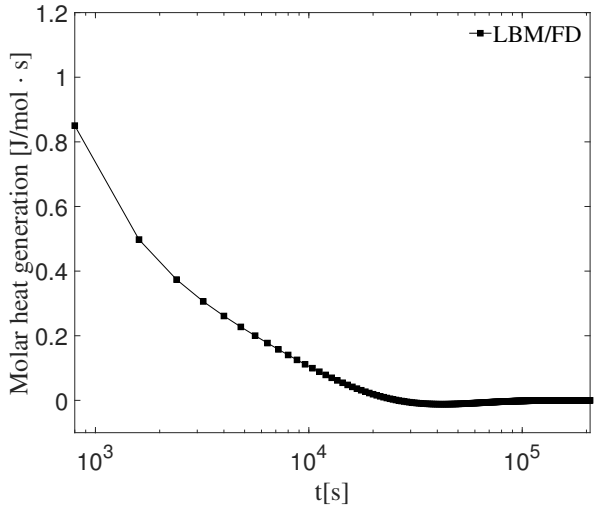

Figure 7.23: Evolution of average molar heat generation with time connected to spherical crystal growth.

This successfully terminates the verification procedure for the developed numerical model. It can now safely be used to investigate growth rates and possible temperature effects for a single S-ma crystal.

7.4.3 Validation for S-ma crystal growth including temperature effects

7.4.3.1 Experiments vs. numerical simulation for different temperatures

An excellent agreement between numerical predictions and experimental observations was observed in a previous section when neglecting the influence of changes in temperature [144]. In order to check now the ability of the solver to correctly describe S-ma crystal growth at different temperatures (from 20°C to 30°C), 2D simulations are carried out using the real reactor geometry. The reduction to two dimensions has already been justified. First, configurations are considered where forced convection is negligible. For all experiments presented in this section the initial seed is a hexagonal crystal. The initial supersaturation is $U = 0.045$, and the temperature is $T = 20°\text{C}$, $T = 25°\text{C}$, or $T = 30°\text{C}$, respectively. The employed physical parameters have been given in Table 7.6. All simulations are carried out with a spatial resolution of $\delta x = 0.1$ mm. The interface thickness is set to $W_0 = 0.25$ mm, the relaxation time to $\tau_0 = 0.02$ s, and the coupling coefficient $\lambda = 3$ was chosen as a standard value for the PF method for dendrite growth [11]. At the walls of the reactor, zero-flux boundary conditions are applied to both the species and phase fields. A constant wall temperature (set as the value of T_1, see Fig. 7.2) is used as boundary condition for the energy equation. At the inlet a constant supersaturation is imposed, following the implementation

described in [63] for the boundary condition.

Table 7.8: Comparison between experiments [142] and simulations for initial supersaturation $U = 0.045$ as a function of temperature.

Average growth rate [mm/h]	$T = 20°C$	$T = 25°C$	$T = 30°C$
Experiments [142]	0.011	0.023	0.0321
Simulations	0.0096	0.0222	0.0317

In Table 7.8, G_{th} is the average growth rate (in mm/h) obtained as $G_{th} = (L_1 + L_2 + L_3 + L_4 + L_5 + L_6)/6t$ in both experiment and simulation (see Fig. 7.6). The comparison between computed and measured values points to a good agreement at all temperatures. It is observed that the S-ma growth rate increases with temperature. As far as can be judged from only 3 values (no other conditions have been investigated experimentally), a quite linear behavior is observed between temperature and growth rate in the range studied. It is now interesting to check the occurrence and strength of possible temperature gradients within this growth cell.

7.4.3.2 Occurrence of temperature gradients during crystal growth

Although the temperature of the single-crystal growth cell in the experimental setting is kept constant through the walls at the temperature of vessel V1, the growth of the crystal generates heat at the interface between liquid and solid phase. The Pt-100 sensor used for the temperature measurements in the experiment delivers only a point value and cannot be used to track possible gradients. Hence, in this section, the temperature field in the whole growth cell is studied numerically. The initial supersaturation is kept at $U_0 = 0.045$ as in the previous section.

In Fig. 7.24, it is seen that the highest temperature in the crystal as well as the solution temperature far from the crystal are still found at around 300 K. However, a maximum difference in temperature of the order of 0.5°C is indeed observed within the cell, with a maximum temperature close to the interface. Though small, this shows that temperature differences do exist within the single-crystal growth cell. Since these differences appear locally, non-negligible temperature gradients will occur as well. Fig. 7.25 demonstrates that the temperature increase reaches a peak value close to the crystal and decreases in the fluid phase toward the walls of the cell.

Fig. 7.26 and 7.27 show the heat release process during phase-change from the liquid into the solid state at the interface of the crystal.

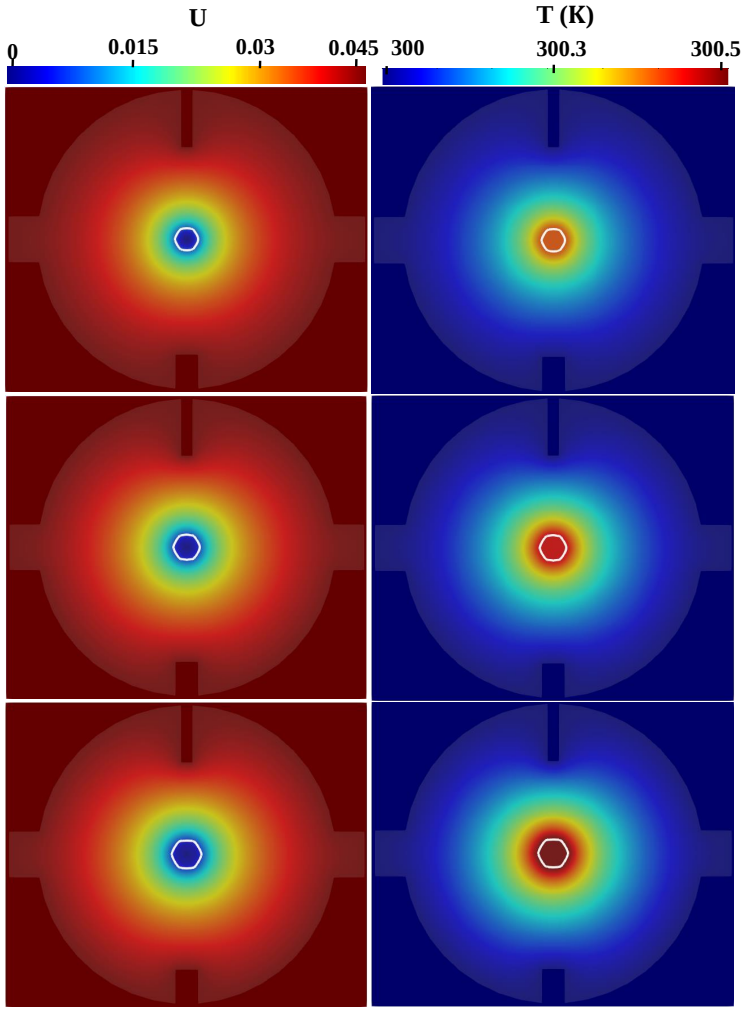

Figure 7.24: Instantaneous supersaturation and temperature fields in the growth cell for initial supersaturation $U_0 = 0.045$ at times $t = 4$ hours (top), 8 hours (center), 16 hours (bottom), respectively.

7.4.3.3 Ventilation and temperature effects during S-ma crystal growth

In the real single-crystal reactor the incoming flow of (S)-mandelic acid in solution might have an impact on crystal growth rate and shape, as demonstrated previous when neglecting temperature changes. The aim of the present section is to check this point for different Reynolds numbers, and to suggest the inclusion of baffles to support symmetrical growth.

Effect of Reynolds number The Reynolds number is defined as Re$= u_{in}D/\nu_f$, where D is the initial diameter of the crystal seed, ν_f is the kinematic viscosity of water, taken at 1 mm^2/s. The inlet velocity is set as u_{in} = 8, 10, 12 or 14 mm/s, respectively.

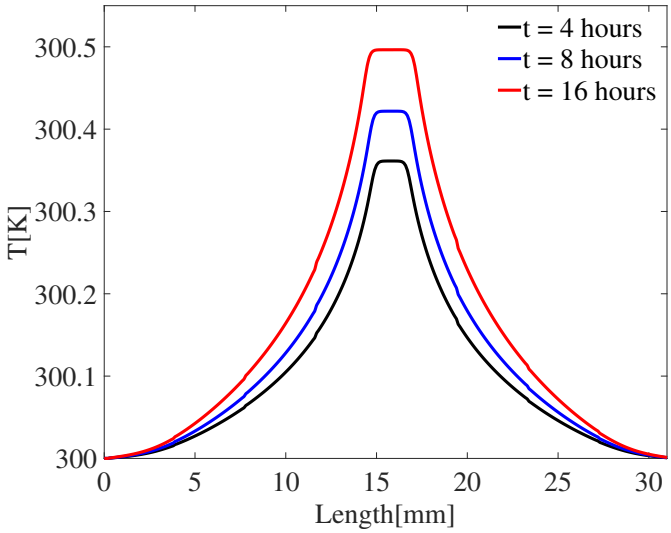

Figure 7.25: Temperature profile around the center-line of the numerical domain at times t =4, 8 and 16 hours, respectively.

Fig. 7.28 shows that at higher Reynolds number, the crystal grows much faster. As a consequence, more heat is generated at the interface because of the intensive solute convection around the crystal. This effect dominates over the accelerated transport of heat away from the crystal by the flow. Overall, an increase of the maximum temperature with Re is observed around the single crystal (see Fig. 7.29).

Baffle As seen from Fig. 7.28 (white lines in the bottom figure, showing the crystal boundary), the overall shape of the crystal varies considerably as function of the Reynolds number, and rapidly becomes non-symmetric. However, the regularity of the crystal shape is a property of high interest regarding the performance of the final products. Therefore, it would be desirable to find a simple geometrical modification to the single-crystal growth cell, leading to isotropic growth rates and/or a desired final aspect ratio. For this purpose, a simple flat baffle has been included in the simulation domain in front of the inlet, in order to prevent a direct impact of the incoming flow onto the growing seed. Three different configurations (different positions) of the baffle have been compared. The resulting configurations are illustrated in Fig. 7.30; what is called configuration 0 is the original case, without any baffle.

Fig. 7.31 shows that ventilation effects are still visible with the baffle at position 1, much more than at other positions; this case leads to the faster crystal growth in vertical direction. The single crystal growth becomes more symmetric as the baffle is placed at a farther distance from the inlet of the growth cell. To quantify the effect of the baffles on the symmetry of the crystal, a quality parameter has been defined as $Q = \max(L_i)/\min(L_i)$ where index $i \in \{0,\ldots,5\}$ covers the length

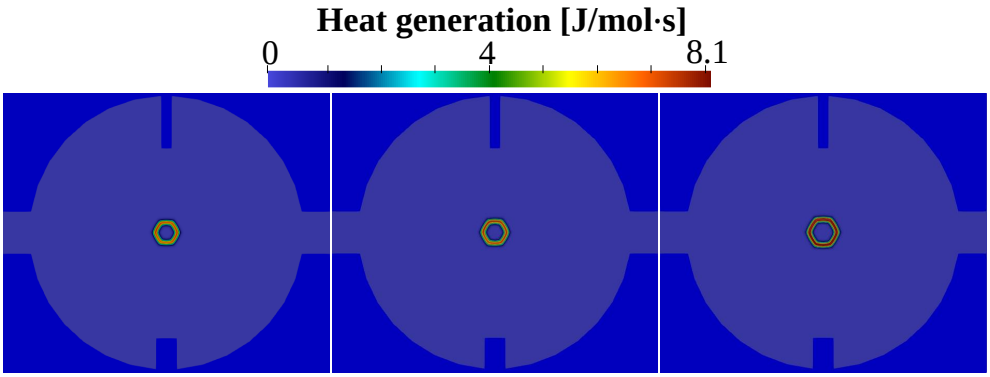

Figure 7.26: Instantaneous heat generation at the interface of the crystal at times t =4, 8 and 16 hours (from left to right), respectively.

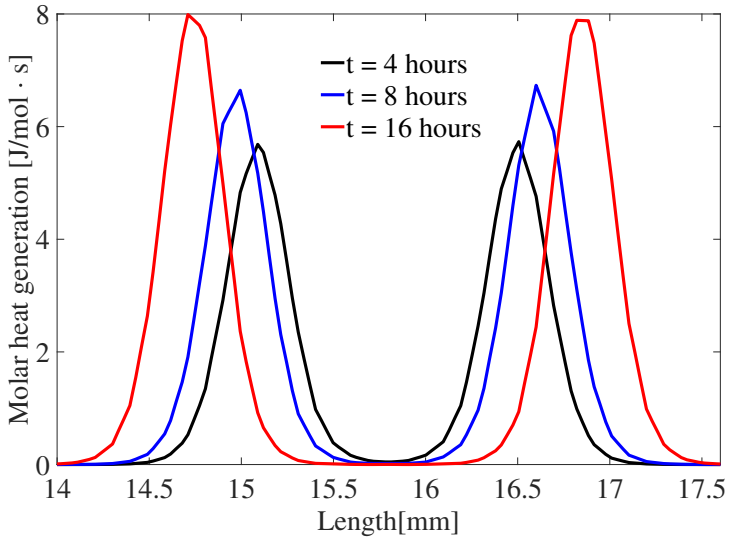

Figure 7.27: Instantaneous heat generation along the centerline of the numerical domain at times t =4, 8 and 16 hours, respectively (zoom on the crystal region).

of all sides of the resulting crystal. Thus, parameter Q quantifies non-isotropic growth, with $Q = 1$ (the minimum value) corresponding to a perfectly isotropic growth, while an increasing value of Q corresponds to increasing non-isotropy. The values of crystal quality as obtained from all simulations after 16 hours of growth are listed in Table 7.9. Overall, the baffle in position 3 should be preferred to get maximum isotropy and minimum temperature effects.

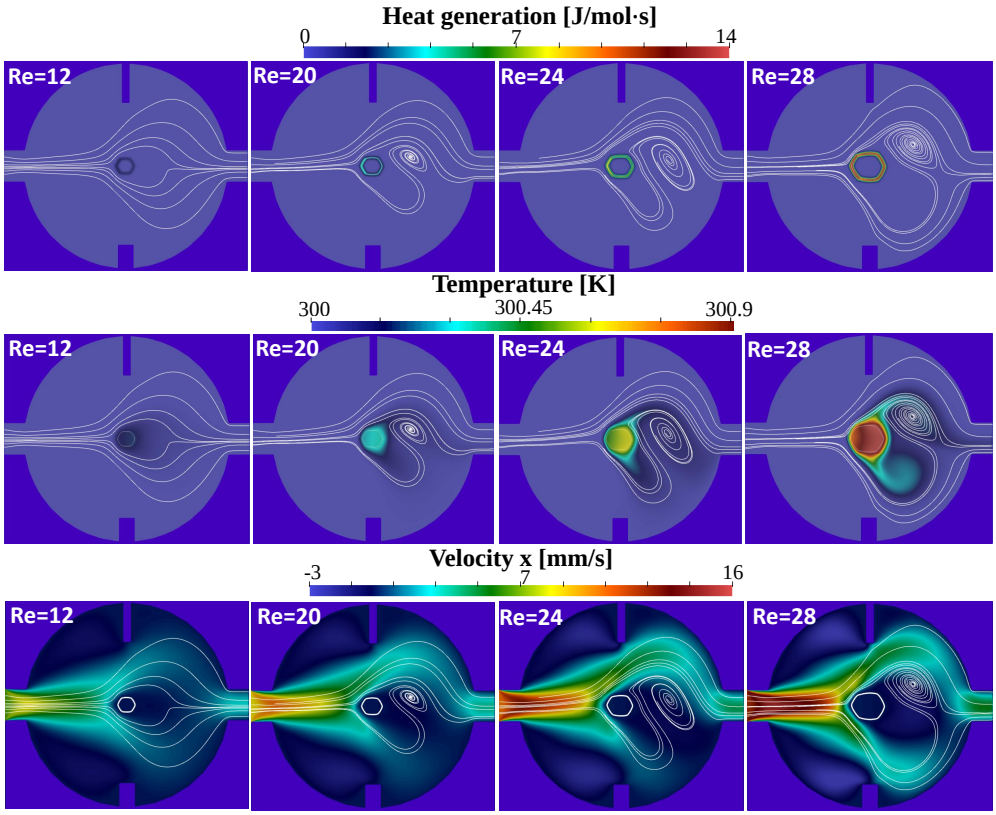

Figure 7.28: Instantaneous fields of heat generation (top), temperature (center), velocity field (bottom) within the growth cell at time t =16 hours for different Reynolds numbers Re = 12, 20, 24, and 28 (from left to right), respectively.

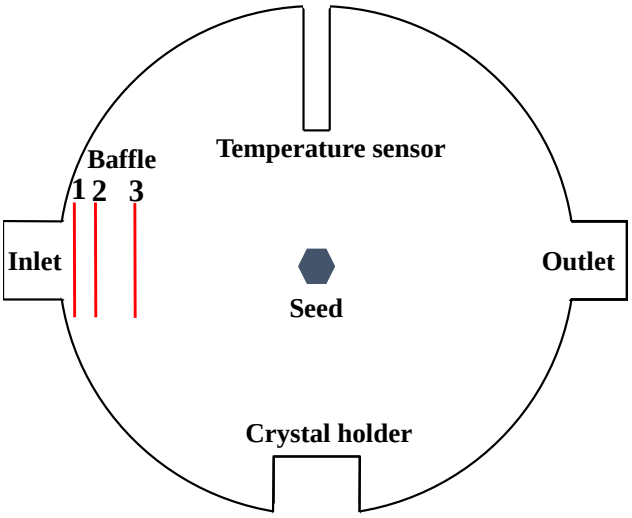

Figure 7.30: 2D growth-cell geometry including baffles at different positions.

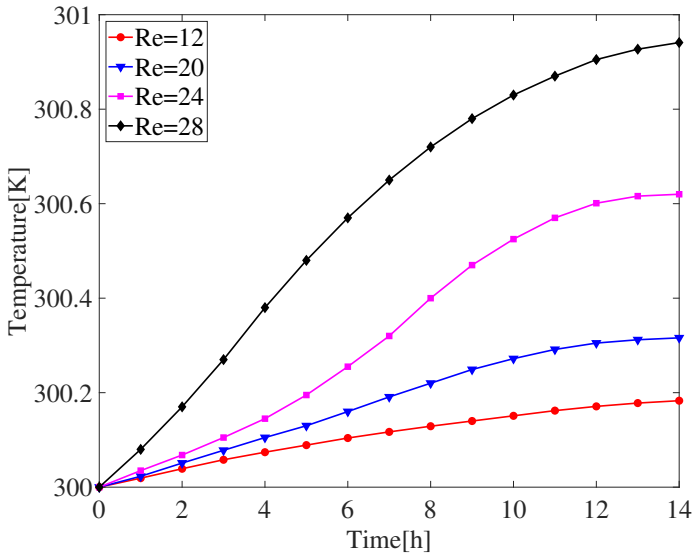

Figure 7.29: Evolution of peak temperature with time within the cell for different Reynolds numbers Re = 12, 20, 24, and 28, respectively.

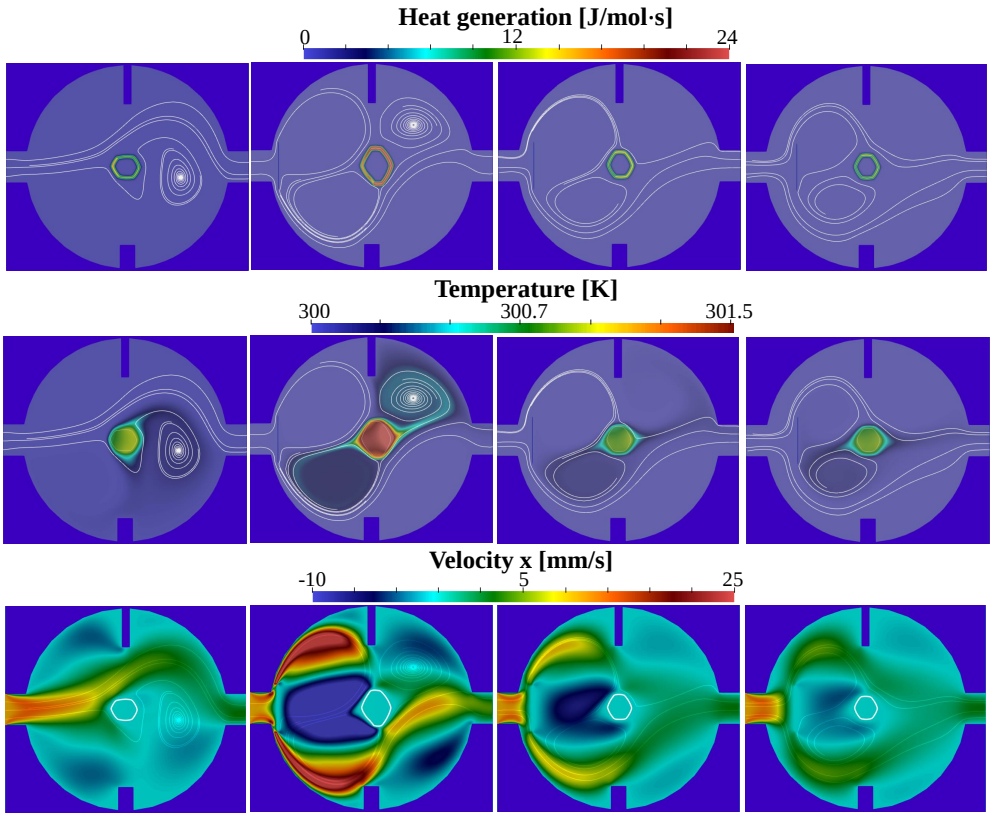

Figure 7.31: Instantaneous fields of heat generation (top), temperature (center), velocity (bottom) at time $t = 16$ hours in the growth cell with the baffle placed at different positions (from left to right): (1) without baffle; (2) with baffle at position 1; (3) with baffle at position 2; (4) with baffle at position 3.

Table 7.9: Impact of the different baffles (see Fig. 7.30) on the isotropy ratio

Position	No Baffle	Baffle 1	Baffle 2	Baffle 3
Q	1.29	1.73	1.16	1.12

Fig. 7.32 shows the peak temperature as function of time for the different baffles. Baffle 1 corresponds to the large ventilation effects visible in Fig. 7.31; then, the crystal side facing the high flow velocity in vertical direction leads to a much larger growth rate there, generating much heat at the crystal interface.

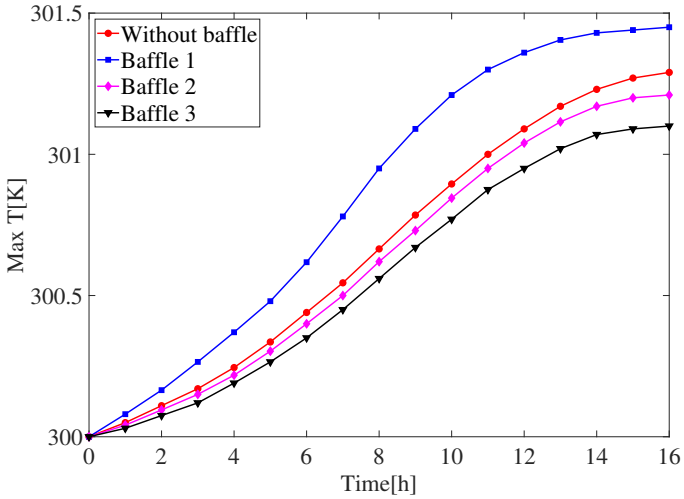

Figure 7.32: Evolution of peak temperature with time for the baffles placed at different positions, for an initial temperature T_0 = 300K.

7.5 Concluding remarks

In Sec. 7.3, a numerical model based on LB has been developed and validated to describe crystal growth. It has been shown to correctly capture the dynamics of (S)-mandelic acid crystal growth. The numerical simulations were compared to experimental data from a single-crystal growth reactor and are in very good agreement. The model was then used to investigate the effects of important parameters such as supersaturation and initial seed size on growth dynamics. It was depicted that higher supersaturation levels lead to much faster growth rates; the impact of a larger initial seed crystal is by far not as strong, but increases slightly the growth rate as well.

It was also demonstrated that hydrodynamics can have pronounced effects on both average growth rate and habit, and may lead to a clear rupture of symmetry. The evolution of the crystal

habit was shown to change significantly with the Reynolds number, but also with the initial orientation of the seed with respect to the incoming flow. Finally, a simple modification of the reactor geometry was proposed to minimize non-symmetrical growth.

In Sec. 7.4, a hybrid LBM/FD method has been used to model the growth of a single crystal of (S)-mandelic acid. LBM is used for the PF equation, while the FD method is applied for the species and energy equations due to the high ratio between thermal and species diffusivity. Selected test-cases show that numerical stability can be achieved with the hybrid solver thanks to the FD method. Successful verification and validation steps are documented. The results provide detailed information regarding the magnitude and dynamics of the temperature fields developing in the measuring cell during the growth process. The heat generation during phase change at the interface of the crystal leads overall to only small changes in temperature over the whole cell. These local changes in temperature lead to noticeable temperature gradients around the crystal interface. For all cases considered, a maximum temperature increase of almost 1.5°C has been observed at the moving crystal interface; the temperature sensor is unable to measure it in the experiments. In this particular case the molar heat generation at the interface can be probably neglected to address most questions of interest. However, convection can amplify temperature differences. Using a baffle located at a suitable position, ventilation and temperature effects can be minimized.

Chapter 8

Conclusions and Outlook

Contents

8.1 Conclusion

In this dissertation, we have developed advanced tools for LB simulations, with the primary aim of exploring crystal growth phenomena in both aqueous and gaseous environments.Our in-house solver, ALBORZ, served as the computational backbone for all simulations conducted throughout the research work. To extend the capabilities of ALBORZ to accommodate the PF model for crystal growth, we developed a coupled flow/species/phase/energy solver based on the LBM.

This research has significantly contributed to our understanding of crystal growth processes through the development and validation of the PF model coupled with the LBM. First, the PF model was introduced from the classical Gibbs–Thomson equation for LB, whereby the incorporation of an anisotropy function facilitated crystal growth direction setting in both 2D and 3D dimensions. Delving into the pivotal role of fluid flow in crystal growth, we introduced modifications to the heat and momentum equations while maintaining the PF equation unaltered. The model excels in practicality, converging to classical equations in the limit of a thin interface, avoiding explicit interface tracking, and enabling computations with approaching zero interface kinetic effects.

Moreover, the adapted LB scheme for the ADE within the PF model was thoroughly developed and validated. This paved the way for a comprehensive simulation of the growth habits of snowflakes and (S)-mandelic acid, respectively. While these models find broad applicability in generic systems, their utilization in simulating realistic systems has been limited. Before delving into the investigation of these crystals in real-world scenarios, we conducted an exploration of the influence of key physical parameters on crystal morphologies and growth rates within the PF model.

Subsequently, our focus shifted to modeling ice crystal growth, introducing a modified PF model coupled with LBM. Rigorous validation against test cases and experimental data underscored the model's ability to capture diverse crystal habits in the plate growth regime. Importantly, the model's predictions aligned well with experimental data and Nakaya diagram predictions [89]. Taking a step further, the model was also used to look at the possible effects of forced convection on the growth dynamics and resulting asymmetrical shapes.

The culmination of our research led us into the intricate realm of modeling mandelic acid crystallization, where we successfully captured the dynamics of (S)-mandelic acid crystal growth. Our growth dynamic analysis, categorized into two parts—without/with temperature effects. In the absence of temperature effects, the model, based solely on the LBM, underwent validation against experimental data, verifying its accuracy.This comprehensive approach provided insights into temperature fields during crystal growth due to the high value of the Lewis number in the energy and species equations.

Our investigations into the influence of parameters such as supersaturation, initial seed size,

and hydrodynamics unveiled subtle yet discernible impacts on growth dynamics and crystal habits. To delve deeper into the thermal aspects of crystal growth, we employed a hybrid LB/FD method due to high value of the Lewis number in the energy and species equations. The results offered detailed insights into the magnitude and dynamics of temperature fields during the crystal growth process, revealing noticeable temperature gradients around the crystal interface.

While the molar heat generation at the interface may be negligible for many questions of interest, the identified factor of convection could potentially amplify temperature differences. To address this, we proposed the strategic placement of a baffle to minimize ventilation and temperature effects, offering a practical mitigation strategy for potential issues.

In conclusion, this dissertation not only signifies a significant advancement in the development of computational tools but also presents a robust framework for comprehensively understanding and simulating crystal growth across various scenarios. The PF models, their validations, and the insights gained lay the groundwork for future advancements in crystal growth modeling and simulations, opening avenues for further exploration and innovation.

8.2 Outlook

In future works, there exists a scope for expanding the applications of this study to encompass more realistic and intricate systems. Regarding snowflakes, an avenue for exploration involves extending simulations to the long-prismatic growth regime, thereby covering the entire spectrum of snowflake habits. This expansion would involve incorporating the influence of local variations in temperature into the model, aiming to provide a more comprehensive understanding of the underlying mechanisms governing snowflake growth [109].

In the context of (S)-mandelic acid, a promising direction for future investigation lies in exploring the impact of impurities, such as enantiomers and carriers present in the aqueous solution, on the growth rate and morphologies of a single mandelic acid crystal. Understanding how impurities influence crystal growth can offer valuable insights into the real-world processes of crystallization, particularly in pharmaceutical and chemical applications.

Moreover, upcoming research endeavors will concentrate on extending the current study to more complex scenarios, delving into three-dimensional cases to better emulate the complexities of actual crystallization environments. The incorporation of additional physical phenomena, such as dynamic fluid flow patterns and intricate heat transfer mechanisms, will be pursued to enhance the model's accuracy and broaden its applicability.

The findings presented in this study not only contribute to the understanding of crystal growth in specific systems but also lay the foundation for advancements in the broader field of crystal growth modeling and simulations. The identified future directions aim to push the boundaries of

our comprehension, enabling the development of more robust and versatile models for predicting and understanding crystal growth in diverse and realistic settings.

Bibliography

[1] A. Younsi and A. Cartalade. On anisotropy function in crystal growth simulations using lattice Boltzmann equation. *Journal of Computational Physics*, 325:1–21, 2016.

[2] A. Younsi, A. Cartalade, and M. Quintard. Lattice Boltzmann simulations for anisotropic crystal growth of a binary mixture. In *International Heat Transfer Conference Digital Library*. Begel House Inc., 2014.

[3] J. A. Sethian and J. Straint. Crystal growth and dendritic solidification. *Journal of Computational Physics*, 98(2):231–253, 1992.

[4] Robert A. Variational algorithms and pattern formation in dendritic solidification. *Journal of Computational Physics*, 106(2):337–354, 1993.

[5] A. R. Roosen and J. E. Taylor. Modeling crystal growth in a diffusion field using fully faceted interfaces. *Journal of Computational physics*, 114(1):113–128, 1994.

[6] J. W. Cahn and J. E. Hilliard. Free energy of a nonuniform system. iii. nucleation in a two-component incompressible fluid. *Journal of Chemical Physics*, 31(3):688–699, 1959.

[7] Y. Sun and C. Beckermann. Sharp interface tracking using the phase-field equation. *Journal of Computational Physics*, 220(2):626–653, 2007.

[8] L. Zheng, T. Lee, Z. Guo, and D. Rumschitzki. Shrinkage of bubbles and drops in the lattice Boltzmann equation method for nonideal gases. *Physical Review E*, 89(3):033302, 2014.

[9] A. Karma and W. J. Rappel. Phase-field method for computationally efficient modeling of solidification with arbitrary interface kinetics. *Physical Review E*, 53(4):R3017, 1996.

[10] A. Karma and W. J. Rappel. Quantitative phase-field modeling of dendritic growth in two and three dimensions. *Physical Review E*, 57(4):4323, 1998.

[11] J. C. Ramirez, C. Beckermann, A. Karma, and H. J. Diepers. Phase-field modeling of binary alloy solidification with coupled heat and solute diffusion. *Physical Review E*, 69(5):051607, 2004.

[12] A. Cartalade, A. Younsi, É. Régnier, and S. Schuller. Simulations of phase-field models for crystal growth and phase separation. *Procedia Materials Science*, 7:72–78, 2014.

[13] G. Demange, H. Zapolsky, R. Patte, and M. Brunel. Snowflake growth in three dimensions using phase field modelling. *NPJ Computational Materials*, 3:2057–3960, 2017.

[14] G. Demange, H. Zapolsky, R. Patte, and M. Brunel. A phase field model for snow crystal growth in three dimensions. *NPJ Computational Materials*, 3(1):1–7, 2017.

[15] G. Demange, H. Zapolsky, R. Patte, and M. Brunel. Growth kinetics and morphology of snowflakes in supersaturated atmosphere using a three-dimensional phase-field model. *Physical Review E*, 96(2):022803, 2017.

[16] C. Beckermann, H. J. Diepers, I. Steinbach, A. Karma, and X. Tong. Modeling melt convection in phase-field simulations of solidification. *Journal of Computational Physics*, 154(2):468–496, 1999.

[17] J. H. Jeong, N. Goldenfeld, and J. A. Dantzig. Phase field model for three-dimensional dendritic growth with fluid flow. *Physical Review E*, 64(4):041602, 2001.

[18] D. Medvedev and K. Kassner. Lattice Boltzmann scheme for crystal growth in external flows. *Physical Review E*, 72(5):056703, 2005.

[19] A. Wheeler, B. Murray, and R. Schaefer. Computation of dendrites using a phase field model. *Physica D: Nonlinear Phenomena*, 66(1-2):243–262, 1993.

[20] R. Kobayashi. Modeling and numerical simulations of dendritic crystal growth. *Physica D: Nonlinear Phenomena*, 63(3-4):410–423, 1993.

[21] J. Debierre, A. Karma, F. Celestini, and R. Guérin. Phase-field approach for faceted solidification. *Physical Review E*, 68(4):041604, 2003.

[22] H. Miura. Anisotropy function of kinetic coefficient for phase-field simulations: reproduction of kinetic wulff shape with arbitrary face angles. *Journal of Crystal Growth*, 367:8–17, 2013.

[23] H Puff. Contribution to the theory of cubic harmonics. *Physica Status Solidi (b)*, 41(1):11–22, 1970.

[24] J. Hoyt, M. Asta, and A. Karma. Atomistic and continuum modeling of dendritic solidification. *Materials Science and Engineering: R: Reports*, 41(6):121–163, 2003.

[25] F. Podmaniczky, G. I. Toth, T. Pusztai, and L. Granasy. Free energy of the bcc–liquid interface and the wulff shape as predicted by the phase-field crystal model. *Journal of Crystal Growth*, 385:148–153, 2014.

[26] A. Rosis, G. Falcucci, S. Ubertini, F. Ubertini, and S. Succi. Lattice Boltzmann analysis of fluid-structure interaction with moving boundaries. *Communications in Computational Physics*, 13(3):823–834, 2013.

[27] Z. Guo and C. Shu. *Lattice Boltzmann method and its application in engineering*, volume 3. World Scientific, 2013.

[28] S. Chen and G. Doolen. Lattice Boltzmann method for fluid flows. *Annual Review of Fluid Mechanics*, 30(1):329–364, 1998.

[29] C. Magono and C. Lee. Meteorological classification of natural snow crystals. *Journal of the Faculty of Science*, 2(4):321–335, 1966.

[30] F. Varnik, J. Baschnagel, and K. Binder. Reduction of the glass transition temperature in polymer films: A molecular-dynamics study. *Physical Review E*, 65(2):021507, 2002.

[31] F. Varnik, J. Baschnagel, and K. Binder. Molecular dynamics results on the pressure tensor of polymer films. *The Journal of Chemical Physics*, 113(10):4444–4453, 2000.

[32] F. Varnik and K. Binder. Shear viscosity of a supercooled polymer melt via nonequilibrium molecular dynamics simulations. *The Journal of Chemical Physics*, 117(13):6336–6349, 2002.

[33] F. Varnik, L. Bocquet, J. Barrat, and L. Berthier. Shear localization in a model glass. *Physical Review Letters*, 90(9):095702, 2003.

[34] U. Frisch, B. Hasslacher, and Y. Pomeau. Lattice-gas automata for the Navier-Stokes equation. In *Lattice Gas Methods for Partial Differential Equations*, pages 11–18. CRC Press, 2019.

[35] J. Hardy, Y. Pomeau, and O. Pazzis. Time evolution of a two-dimensional model system. i. invariant states and time correlation functions. *Journal of Mathematical Physics*, 14(12):1746–1759, 1973.

[36] Sauro Succi. *The lattice Boltzmann equation: for fluid dynamics and beyond*. Oxford University Press, 2001.

[37] G. McNamara and G. Zanetti. Use of the Boltzmann equation to simulate lattice-gas automata. In *Lattice Gas Methods For Partial Differential Equations*, pages 289–296. CRC Press, 2019.

[38] X. He and L. Luo. Theory of the lattice Boltzmann method: From the Boltzmann equation to the lattice Boltzmann equation. *Physical Review E*, 56(6):6811, 1997.

[39] J. Koelman. A simple lattice Boltzmann scheme for Navier-Stokes fluid flow. *Europhysics Letters*, 15(6):603, 1991.

[40] S. Chen, H. Chen, D. Martnez, and W. Matthaeus. Lattice Boltzmann model for simulation of magnetohydrodynamics. *Physical Review Letters*, 67(27):3776, 1991.

[41] F. J. Higuera and J. Jiménez. Boltzmann approach to lattice gas simulations. *Europhysics Letters*, 9(7):663, 1989.

[42] P. Bhathnagor, E. Gross, and M. Krook. A model for collision processes in gases. *Physical Review*, 94(3):511, 1954.

[43] D. d'Humieres. Generalized lattice-Boltzmann equations. *Rarefied Gas Dynamics*, 1992.

[44] D. d'Humières. Multiple–relaxation–time lattice Boltzmann models in three dimensions. *Philosophical Transactions of the Royal Society of London. Series A: Mathematical, Physical and Engineering Sciences*, 360(1792):437–451, 2002.

[45] G. D. Doolen. Lattice Boltzmann methods for fluid flows. *Annual Review of Fluid Mechanics*, 30(1):329–364, 1998.

[46] H. W. Zheng, C. Shu, and Y. T. Chew. A lattice Boltzmann model for multiphase flows with large density ratio. *Journal of Computational Physics*, 218(1):353–371, 2006.

[47] S. A. Hosseini, N. Darabiha, and D. Thévenin. Mass-conserving advection–diffusion lattice Boltzmann model for multi-species reacting flows. *Physica A: Statistical Mechanics and its Applications*, 499:40–57, 2018.

[48] S. A. Hosseini, H. Safari, N. Darabiha, D. Thévenin, and M. Krafczyk. Hybrid lattice Boltzmann-finite difference model for low Mach number combustion simulation. *Combustion and Flame*, 209:394–404, 2019.

[49] S. A. Hosseini, A. Abdelsamie, N. Darabiha, and D. Thévenin. Low-Mach hybrid lattice Boltzmann-finite difference solver for combustion in complex flows. *Physics of Fluids*, 32(7):077105, 2020.

[50] D. Chatterjee and S. Chakraborty. A hybrid lattice Boltzmann model for solid–liquid phase transition in presence of fluid flow. *Physics Letters A*, 351(4-5):359–367, 2006.

[51] I. Rasin, W. Miller, and S. Succi. Phase-field lattice kinetic scheme for the numerical simulation of dendritic growth. *Physical Review E*, 72(6):066705, 2005.

[52] W. Miller, I. Rasin, and S. Succi. Lattice Boltzmann phase-field modelling of binary-alloy solidification. *Physica A: Statistical Mechanics and its Applications*, 362(1):78–83, 2006.

[53] D. Medvedev, T. Fischaleck, and K. Kassner. Influence of external flows on crystal growth: Numerical investigation. *Physical Review E*, 74(3):031606, 2006.

[54] C. Huber, A. Parmigiani, B. Chopard, M. Manga, and O. Bachmann. Lattice Boltzmann model for melting with natural convection. *International Journal of Heat and Fluid Flow*, 29(5):1469–1480, 2008.

[55] D. Sun, M. Zhu, S. Pan, and D. Raabe. Lattice Boltzmann modeling of dendritic growth in a forced melt convection. *Acta Materialia*, 57(6):1755–1767, 2009.

[56] G. Lin, J. Bao, and Z. Xu. A three-dimensional phase field model coupled with a lattice kinetics solver for modeling crystal growth in furnaces with accelerated crucible rotation and traveling magnetic field. *Computers & Fluids*, 103:204–214, 2014.

[57] T. Abe. Derivation of the lattice Boltzmann method by means of the discrete ordinate method for the Boltzmann equation. *Journal of Computational Physics*, 131(1), 1997.

[58] G. De Marsily. Quantitative hydrogeology. Technical report, Paris School of Mines, Fontainebleau, 1986.

[59] N. Provatas and K. Elder. *Phase-field methods in materials science and engineering*. John Wiley & Sons, 2011.

[60] B. Echebarria, R. Folch, A. Karma, and M. Plapp. Quantitative phase-field model of alloy solidification. *Physical Review E*, 70(6):061604, 2004.

[61] S. D. Walsh and M. O. Saar. Macroscale lattice-Boltzmann methods for low Peclet number solute and heat transport in heterogeneous porous media. *Water Resources Research*, 46(7), 2010.

[62] K. Timm, H. Kusumaatmaja, A. Kuzmin, O. Shardt, G. Silva, and E. Viggen. The lattice Boltzmann method: principles and practice. *Springer International Publishing AG*, 2016.

[63] T. Krüger, H. Kusumaatmaja, A. Kuzmin, O. Shardt, G. Silva, and E. M. Viggen. *The lattice Boltzmann method*. Springer, 2017.

[64] I. Ginzburg. Equilibrium-type and link-type lattice Boltzmann models for generic advection and anisotropic-dispersion equation. *Advances in Water Resources*, 28(11):1171–1195, 2005.

[65] A Fedi, M Massabò, O Paladino, and R Cianci. A new analytical solution for the 2d advection–dispersion equation in semi-infinite and laterally bounded domain. *Applied Mathematical Sciences*, 4(75):3733–3747, 2010.

[66] S. Ponce D., S. Chen, and G. D. Doolen. Lattice Boltzmann computations for reaction-diffusion equations. *The Journal of Chemical Physics*, 98(2):1514–1523, 1993.

[67] A. Cartalade, A. Younsi, and M. Plapp. Lattice Boltzmann simulations of 3d crystal growth: Numerical schemes for a phase-field model with anti-trapping current. *Computers & Mathematics with Applications*, 71(9):1784–1798, 2016.

[68] Z. Guo, C. Zheng, and B. Shi. Discrete lattice effects on the forcing term in the lattice Boltzmann method. *Physical Review E*, 65(4):046308, 2002.

[69] S. A. Hosseini, N. Darabiha, and D. Thévenin. Compressibility in lattice Boltzmann on standard stencils: effects of deviation from reference temperature. *Philosophical Transactions of the Royal Society A*, 378(2175):20190399, 2020.

[70] L. Chen, Q. Kang, Y. Mu, Y. He, and W. Tao. A critical review of the pseudopotential multiphase lattice Boltzmann model: Methods and applications. *International Journal of Heat and Mass Transfer*, 76:210–236, 2014.

[71] X. Shan. Analysis and reduction of the spurious current in a class of multiphase lattice Boltzmann models. *Physical Review E*, 73(4):047701, 2006.

[72] M. Sbragaglia, R. Benzi, L. Biferale, S. Succi, K. Sugiyama, and F. Toschi. Generalized lattice Boltzmann method with multirange pseudopotential. *Physical Review E*, 75(2):026702, 2007.

[73] J. J. Eggleston, G. B. McFadden, and P. W. Voorhees. A phase-field model for highly anisotropic interfacial energy. *Physica D: Nonlinear Phenomena*, 150(1-2):91–103, 2001.

[74] F. Frank. Metal surfaces. *ASM, Cleveland, OH*, 1963.

[75] S. Dennis and G. Chang. Numerical solutions for steady flow past a circular cylinder at Reynolds numbers up to 100. *Journal of Fluid Mechanics*, 42(3):471–489, 1970.

[76] B. Fornberg. A numerical study of steady viscous flow past a circular cylinder. *Journal of Fluid Mechanics*, 98(4):819–855, 1980.

[77] X. He and G. Doolen. Lattice Boltzmann method on curvilinear coordinates system: flow around a circular cylinder. *Journal of Computational Physics*, 134(2):306–315, 1997.

[78] X. Wang, C. Shu, J. Wu, and L. Yang. A boundary condition-implemented immersed boundary-lattice Boltzmann method and its application for simulation of flows around a circular cylinder. *Advances in Applied Mathematics and Mechanics*, 6(6):811–829, 2014.

[79] F. Nieuwstadt and H.B. Keller. Viscous flow past circular cylinders. *Computers & Fluids*, 1(1):59–71, 1973.

[80] T. Lei, K. H. Luo, and D. Wu. Generalized lattice Boltzmann model for frosting. *Physical Review E*, 99(5):053301, 2019.

[81] F. Frank. Snow crystals. *Contemporary Physics*, 23(1):3–22, 1982.

[82] B. J. Mason. Snow crystals, natural and man made. *Contemporary Physics*, 33(4):227–243, 1992.

[83] P. K. Wang. Shape and microdynamics of ice particles and their effects in cirrus clouds. *Advances in Geophysics*, 45:1–258, 2002.

[84] I. Shafranovskii. Kepler's Crystallographic ideas and his tract "the six-cornered snowflake". *Vistas in Astronomy*, 18:861–876, 1975.

[85] F. E. Chickering. *Cloud Crystals: A Snow-flake Album*. Appleton, 1864.

[86] W. Bentley and W. Humphreys. Snow Crystals. *Journal of Interdisciplinary History*, 1931.

[87] U. Nakaya. *Snow crystals: Natural and Artificial*. Harvard University Press, 2013.

[88] T. Gonda and S. Nakahara. Dendritic ice crystals with faceted tip growing from the vapor phase. *Journal of Crystal Growth*, 173(1-2):189–193, 1997.

[89] U. Nakaya. The formation of ice crystals. *Compendium of Meteorology*, pages 207–220, 1951.

[90] K. G. Libbrecht. Snowcrystals.com, 1999.

[91] U. Nakaya. Snow crystals, natural and artificial. *Harvard University Press*, page 510, 1954.

[92] K. G. Libbrecht. The physics of snow crystals. *Reports on Progress in Physics*, 68(4):855, 2005.

[93] K. G. Libbrecht. Morphogenesis on ice: The physics of snow crystals. *Engineering and Science*, 64(1):10–19, 2001.

[94] K. G. Libbrecht. Physical dynamics of ice crystal growth. *Annual Review of Materials Research*, 47:271–295, 2017.

[95] G. Ross. The snowflake: Winter's Secret Beauty. *American Scientist*, 92(2):181–182, 2004.

[96] B. Mason. The growth of ice crystals from the vapour and the melt. *Advances in Physics*, 7(26):235–253, 1958.

[97] J. Nelson and C. Knight. Snow crystal habit changes explained by layer nucleation. *Journal of the Atmospheric Sciences*, 55(8):1452–1465, 1998.

[98] J. Nelson. Growth mechanisms to explain the primary and secondary habits of snow crystals. *Philosophical Magazine A*, 81(10):2337–2373, 2001.

[99] K. G. Libbrecht and M. E. Rickerby. Measurements of surface attachment kinetics for faceted ice crystal growth. *Journal of Crystal Growth*, 377:1–8, 2013.

[100] J. Gravner and D. Griffeath. Modeling snow-crystal growth: A three-dimensional mesoscopic approach. *Physical Review E*, 79(1):011601, 2009.

[101] J. G. Kelly and E. C. Boyer. Physical improvements to a mesoscopic cellular automaton model for three-dimensional snow crystal growth. *Crystal Growth & Design*, 14(3):1392–1405, 2014.

[102] J. W. Barrett, H. Garcke, and R. Nürnberg. Numerical computations of faceted pattern formation in snow crystal growth. *Physical Review E*, 86(1):011604, 2012.

[103] I. Singer-Loginova and H. M. Singer. The phase field technique for modeling multiphase materials. *Reports on Progress in Physics*, 71(10):106501, 2008.

[104] J.S. Marshall and M. P. Langleben. A theory of snow-crystal habit and growth. *Journal of Atmospheric Sciences*, 11(2):104–120, 1954.

[105] I. Yoshizaki, T. Ishikawa, S. Adachi, E. Yokoyama, and Y. Furukawa. Precise measurements of dendrite growth of ice crystals in microgravity. *Microgravity Science and Technology*, 24(4):245–253, 2012.

[106] T. Takahashi, T. Endoh, G. Wakahama, and N. Fukuta. Vapor diffusional growth of free-falling snow crystals between -3 and-23°C. *Journal of the Meteorological Society of Japan. Ser. II*, 69(1):15–30, 1991.

[107] K. G. Libbrecht. Physically derived rules for simulating faceted crystal growth using cellular automata. *Materials Science*, 2008.

[108] K. G. Libbrecht and H. M. Arnold. Aerodynamic stability and the growth of triangular snow crystals. *Materials Science*, 2009.

[109] S. A. Hosseini, N. Darabiha, and D. Thévenin. Lattice Boltzmann advection-diffusion model for conjugate heat transfer in heterogeneous media. *International Journal of Heat and Mass Transfer*, 132:906–919, 2019.

[110] M. B. Taylor. Summary of mandelic acid for the improvement of skin conditions. *Cosmet. Dermatol.*, 12:26–8, 1999.

[111] H. G. Brittain. Mandelic acid. In *Analytical Profiles of Drug Substances and Excipients*, volume 29, pages 179–211. Elsevier, 2002.

[112] V. K. Garg, S. Sinha, and R. Sarkar. Glycolic acid peels versus salicylic–mandelic acid peels in active acne vulgaris and post-acne scarring and hyperpigmentation: a comparative study. *Dermatologic Surgery*, 35(1):59–65, 2009.

[113] H. Lorenz and A. Seidel-Morgenstern. Processes to separate enantiomers. *Angewandte Chemie International Edition*, 53(5):1218–1250, 2014.

[114] M. D. Higgins. Numerical modeling of crystal shapes in thin sections: estimation of crystal habit and true size. *American Mineralogist*, 79(1-2):113–119, 1994.

[115] S. Srisanga, A. E. Flood, S. C. Galbraith, S. Rugmai, S. Soontaranon, and J. Ulrich. Crystal growth rate dispersion versus size-dependent crystal growth: Appropriate modeling for crystallization processes. *Crystal Growth & Design*, 15(5):2330–2336, 2015.

[116] C. Y. Ma and X. Z. Wang. Crystal growth rate dispersion modeling using morphological population balance. *AIChE Journal*, 54(9):2321–2334, 2008.

[117] G. Hofmann. *Kristallisation in der industriellen Praxis*. John Wiley & Sons, 2004.

[118] A. Alvarez Rodrigo, H. Lorenz, and A. Seidel-Morgenstern. Online monitoring of preferential crystallization of enantiomers. *Chirality: The Pharmacological, Biological, and Chemical Consequences of Molecular Asymmetry*, 16(8):499–508, 2004.

[119] G. Coquerel. Preferential crystallization. *Novel Optical Resolution Technologies*, pages 1–51, 2006.

[120] J. Gänsch, N. Huskova, K. Kerst, E. Temmel, H. Lorenz, M. Mangold, G. Janiga, and A. Seidel-Morgenstern. Continuous enantioselective crystallization of chiral compounds in coupled fluidized beds. *Chemical Engineering Journal*, page 129627, 2021.

[121] L. Gou, H. Lorenz, and A. Seidel-Morgenstern. Investigation of a chiral additive used in preferential crystallization. *Crystal Growth & Design*, 12(11):5197–5202, 2012.

[122] A. Perlberg, H. Lorenz, and A. Seidel-Morgenstern. Crystal growth kinetics via isothermal seeded batch crystallization: Evaluation of measurement techniques and application to mandelic acid in water. *Industrial & Engineering Chemistry Research*, 44(4):1012–1020, 2005.

[123] L. Codan, C. F. Eckstein, and M. Mazzotti. Growth kinetics of S-mandelic acid in aqueous solutions in the presence of R-mandelic acid. *Crystal Growth & Design*, 13(2):652–663, 2013.

[124] W. J. Boettinger, J. A. Warren, C. Beckermann, and A. Karma. Phase-field simulation of solidification. *Annual Review of Materials Research*, 32(1):163–194, 2002.

[125] B. Nestler and A. Wheeler. Phase-field modeling of multi-phase solidification. *Computer Physics Communications*, 147(1-2):230–233, 2002.

[126] L. Q. Chen and W. Yang. Computer simulation of the domain dynamics of a quenched system with a large number of nonconserved order parameters: The grain-growth kinetics. *Physical Review B*, 50(21):15752, 1994.

[127] T. Takaki, M. Ohno, Y. Shibuta, S. Sakane, T. Shimokawabe, and T. Aoki. Two-dimensional phase-field study of competitive grain growth during directional solidification of polycrystalline binary alloy. *Journal of Crystal Growth*, 442:14–24, 2016.

[128] D. Tourret, Y. Song, A. J. Clarke, and A. Karma. Grain growth competition during thin-sample directional solidification of dendritic microstructures: A phase-field study. *Acta Materialia*, 122:220–235, 2017.

[129] H. Wang, X. Yuan, H. Liang, Z. Chai, and B. Shi. A brief review of the phase-field-based lattice Boltzmann method for multiphase flows. *Capillarity*, 2(3):33–52, 2019.

[130] R. Rojas, T. Takaki, and M. Ohno. A phase-field-lattice Boltzmann method for modeling motion and growth of a dendrite for binary alloy solidification in the presence of melt convection. *Journal of Computational Physics*, 298:29–40, 2015.

[131] R. Schiedung, M. Tegeler, D. Medvedev, and F. Varnik. Simulation of capillary-driven kinetics with multi-phase-field and lattice Boltzmann method. *Modelling and Simulation in Materials Science and Engineering*, 28(6):065008, 2020.

[132] S. Vakili, I. Steinbach, and F. Varnik. Multi-phase-field simulation of microstructure evolution in metallic foams. *Scientific Reports*, 10(1):1–12, 2020.

[133] E. M. Zirdehi and F. Varnik. Non-monotonic effect of additive particle size on the glass transition in polymers. *Journal of Chemical Physics*, 150(2):024903, 2019.

[134] M. Henniges, S.A. Hosseini, D. Thévenin, A. Seidel-Morgenstern, and H. Lorenz. Towards predictive numerical models for single crystal growth: validation of the velocity field. In *Proc. 24th International Workshop on Industrial Crystallization BIWIC2017*, 2017.

[135] S. Sakane, T. Takaki, M. Ohno, Y. Shibuta, T. Shimokawabe, and T. Aoki. Three-dimensional morphologies of inclined equiaxed dendrites growing under forced convection by phase-field-lattice Boltzmann method. *Journal of Crystal Growth*, 483:147–155, 2018.

[136] S. Chakraborty and D. Chatterjee. An enthalpy-based hybrid lattice-Boltzmann method for modelling solid–liquid phase transition in the presence of convective transport. *Journal of Fluid Mechanics*, 592:155–175, 2007.

[137] Q. Tan, S.A. Hosseini, A. Seidel-Morgenstern, D. Thévenin, and H. Lorenz. Modeling ice crystal growth using the lattice Boltzmann method. *Physics of Fluids*, 34(1):013311, 2022.

[138] S. A. Hosseini. *Development of a lattice Boltzmann-based numerical method for the simulation of reacting flows*. PhD thesis, Université Paris-Saclay & Otto-von-Guericke University, 2020.

[139] J. Bianco. Single-crystal growth kinetics in a chiral system. Master Thesis. *Otto von Guericke University Magdeburg*, 2009.

[140] J. W. Mullin. *Crystallization*. Elsevier, 2001.

[141] Y. Chenyakin, D. A Ullmann, E. Evoy, L. Renbaum-Wolff, S. Kamal, and A. K. Bertram. Diffusion coefficients of organic molecules in sucrose–water solutions and comparison with Stokes–Einstein predictions. *Atmospheric Chemistry and Physics*, 17(3):2423–2435, 2017.

[142] L. Klukas. Einzelkornuntersuchungen zum Kristallwachstum in chiralen Systemen. *Internal Report Magdeburg-Stendal University of Applied Sciences, Magdeburg*, 2006.

[143] H. Briesen. Simulation of crystal size and shape by means of a reduced two-dimensional population balance model. *Chemical Engineering Science*, 61(1):104–112, 2006.

[144] Q. Tan, S. A. Hosseini, A. Seidel-Morgenstern, D. Thevenin, and H. Lorenz. Mandelic acid single-crystal growth: Experiments vs. numerical simulations. *Communication Computational Physics*, 33(1):77–100, 2023.

[145] A. Subhedar, K. Galenko, and F. Varnik. Diffuse interface models of solidification with convection: The choice of a finite interface thickness. *The European Physical Journal Special Topics*, 229:447–452, 2020.

[146] S. A. Hosseini, Nasser Darabiha, and Dominique Thévenin. Low Mach number lattice Boltzmann model for turbulent combustion: flow in confined geometries. *Proceedings of the Combustion Institute*, 2022.

[147] V. N Emelýanenko, V. V Turovtsev, and Y. A Fedina. Experimental and theoretical thermodynamic properties of R-(-)-and S-(+)-mandelic acids. *Thermochimica Acta*, 665:37–42, 2018.

[148] D. Sapoundjiev, H. Lorenz, and A. Seidel-Morgenstern. Determination of solubility data by means of calorimetry. *Thermochimica Acta*, 436(1-2):1–9, 2005.

[149] G. A Slack. The thermal conductivity of nonmetallic crystals. *Solid State Physics*, 34:1–71, 1979.

[150] R. J. Speedy. Stability-limit conjecture. an interpretation of the properties of water. *The Journal of Physical Chemistry*, 86(6):982–991, 1982.

[151] J. Tanner. Intracellular diffusion of water. *Archives of Biochemistry and Biophysics*, 224(2):416–428, 1983.

[152] Y. Zhang, S. Mao, A. Ray, and S. Rohani. Nucleation and growth kinetics of (R)-mandelic acid from aqueous solution in the presence of the opposite enantiomer. *Crystal Growth & Design*, 10(7):2879–2887, 2010.

[153] https://www.chemicalbook.com/ChemicalProductProperty_EN_CB7428618.htm.

[154] J. Patterson and E. Morris. Measurement of absolute water density, 1°C to 40°C. *Metrologia*, 31(4):277, 1994.

[155] H. Lorenz, D. Sapoundjiev, and A. Seidel-Morgenstern. Enantiomeric mandelic acid system melting point phase diagram and solubility in water. *Journal of Chemical & Engineering Data*, 47(5):1280–1284, 2002.

Appendix A

Chapman-Enskog expansions for phase-field equation

We present in this appendix the Chapman–Enskog expansions for the PF equation. Firstly, the continuous equation for the moments of the equilibrium distribution function $h_i^{(0)}$ is established. In the second part, we focus on the derivation of a specific form of the equilibrium distribution $h_i^{(0)}$. For more concision, dependencies in $\boldsymbol{x}$ and t are canceled in functions h_i, η_ϕ and Q. The PF Eq. (2.16) is modeled using a modified LB scheme defined as [61, 67]:

$$\begin{aligned} a_s^2(\boldsymbol{n})h_i(\boldsymbol{x}+1,t+1) &= h_i(\boldsymbol{x},t) - \left(1-a_s^2(\boldsymbol{n})\right)h_i(\boldsymbol{x}+1,t) \\ &\quad -\frac{1}{\eta_\phi(\boldsymbol{x},t)}\left[h_i(\boldsymbol{x},t)-h_i^{eq}(\boldsymbol{x},t)\right] \\ &\quad +\omega_i Q_\phi(\boldsymbol{x},t)\frac{\delta t}{\tau_0}, \end{aligned} \tag{A.1}$$

with the equilibrium distribution function given as:

$$h_i^{eq} = \omega_i\left(\phi - \frac{1}{c_s^2}\boldsymbol{c}_i\cdot\mathscr{N}(\boldsymbol{x},t)\frac{W_0^2}{\tau_0}\frac{\delta t}{\delta x}\right). \tag{A.2}$$

$\mathscr{N}(\boldsymbol{x},t)$ is defined by:

$$\mathscr{N}(\boldsymbol{x},t) = |\nabla\phi|^2 a_s(\boldsymbol{n})\left(\frac{\partial a_s(\boldsymbol{n})}{\partial(\partial_x\phi)},\frac{\partial a_s(\boldsymbol{n})}{\partial(\partial_y\phi)},\frac{\partial a_s(\boldsymbol{n})}{\partial(\partial_z\phi)}\right)^T, \tag{A.3}$$

The LHS of Eq. (A.1) can be expanded by a second-order Taylor series (omitting the factor $a_s^2(\boldsymbol{n})$) as follows:

$$h_i(\boldsymbol{x}+1,t+1) = h_i(\boldsymbol{x},t) + (\partial_t + \nabla\cdot\boldsymbol{c}_i)\,h_i + \frac{1}{2}\left(\partial_t^2 + 2\partial_t\nabla\cdot\boldsymbol{c}_i + \nabla\nabla:\boldsymbol{c}_i\boldsymbol{c}_i\right)h_i, \tag{A.4}$$

The second term on the RHS of Eq. (A.1) can be expanded by a second-order Taylor series as follows:

$$h_i(\boldsymbol{x}+1,t) = h_i(\boldsymbol{x},t) + \left(\nabla\cdot\boldsymbol{c}_i + \frac{1}{2}(\nabla\nabla:\boldsymbol{c}_i\boldsymbol{c}_i)\right)h_i, \tag{A.5}$$

The updated distribution function can be written using Taylor series:

$$\begin{aligned}\frac{1}{\eta_\phi(\boldsymbol{x},t)}\left(h_i^0(\boldsymbol{x},t) - h_i(\boldsymbol{x},t)\right) &= a_s^2(\boldsymbol{n})\left(\partial_t + \frac{1}{2}\partial_t^2 + \partial_t\nabla\cdot\boldsymbol{c}_i\right)h_i \\ &\quad + \left(\nabla\cdot\boldsymbol{c}_i + \frac{1}{2}\nabla\nabla:\boldsymbol{c}_i\boldsymbol{c}_i\right)h_i \\ &\quad - \omega_i Q_\phi(\boldsymbol{x},t)\frac{\delta t}{\tau_0},\end{aligned} \tag{A.6}$$

where h_i^0 is the equilibrium distribution function. In the next step, the time scale of different physical phenomena should be separated.

$$\partial_t = \varepsilon\partial_{t_1} + \varepsilon^2\partial_{t_2} + O(\varepsilon^3), \tag{A.7}$$

The space derivative is expanded in the same manner:

$$\nabla = \varepsilon\nabla_1 + \varepsilon^2\nabla_2 + O(\varepsilon^3), \tag{A.8}$$

The distribution functions are also expanded, starting with a zeroth order. It means that the non-equilibrium part of the distribution function is considered as small perturbation from equilibrium state, with the scale of Knudsen number $O(\varepsilon)$.

$$h_i = h_i^{(0)} + \varepsilon h_i^{(1)} + \varepsilon^2 h_i^{(2)} + O(\varepsilon^3), \tag{A.9}$$

where $h_i^{(0)}$ is the equilibrium distribution function. By replacing Eqs. (A.7)-(A.9) into Eq. (A.1) we would have

$$\begin{aligned}
-\frac{1}{\eta_\phi(\boldsymbol{x},t)}\left(\varepsilon h_i^{(1)}+\varepsilon^2 h_i^{(2)}\right) &= a_s^2(\boldsymbol{n})(\varepsilon\partial_{t_1}+\varepsilon^2\partial_{t_2})(h_i^{(0)}+\varepsilon h_i^{(1)}+\varepsilon^2 h_i^{(2)}) \\
&+a_s^2(\boldsymbol{n})\frac{1}{2}(\varepsilon\partial_{t_1}+\varepsilon^2\partial_{t_2})(\varepsilon\partial_{t_1}+\varepsilon^2\partial_{t_2})(h_i^{(0)}+\varepsilon h_i^{(1)}+\varepsilon^2 h_i^{(2)}) \\
&+a_s^2(\boldsymbol{n})(\varepsilon\partial_{t_1}+\varepsilon^2\partial_{t_2})(\varepsilon\nabla_1\cdot\boldsymbol{c}_i+\varepsilon^2\nabla_2\cdot\boldsymbol{c}_i)(h_i^{(0)}+\varepsilon h_i^{(1)}+\varepsilon^2 h_i^{(2)}) \\
&+(\varepsilon\nabla_1\cdot\boldsymbol{c}_i+\varepsilon^2\nabla_2\cdot\boldsymbol{c}_i)(h_i^{(0)}+\varepsilon h_i^{(1)}+\varepsilon^2 h_i^{(2)}) \\
&+\frac{1}{2}(\varepsilon\nabla_1\cdot\boldsymbol{c}_i+\varepsilon^2\nabla_2\cdot\boldsymbol{c}_i)(\varepsilon\nabla_1\cdot\boldsymbol{c}_i+\varepsilon^2\nabla_2\cdot\boldsymbol{c}_i)(h_i^{(0)}+\varepsilon h_i^{(1)}+\varepsilon^2 h_i^{(2)}) \\
&-\omega_i Q_\phi(\boldsymbol{x},t)\frac{\delta t}{\tau_0}, \qquad \text{(A.10)}
\end{aligned}$$

Keeping only the terms up to second order and collecting the terms of order of ε from both sides of the above equations, one obtains:

$$-\varepsilon\frac{1}{\eta_\phi}h_i^{(1)}=\varepsilon\left(a_s^2(\boldsymbol{n})\partial_{t_1}+\nabla_1\cdot\boldsymbol{c}_i\right)h_i^{(0)}, \qquad \text{(A.11)}$$

A similar approach for the terms with ε^2 coefficient leads to:

$$\begin{aligned}
-\frac{1}{\eta_\phi}\varepsilon^2 h_i^{(2)} &= \varepsilon^2\left(a_s^2(\boldsymbol{n})\partial_{t_2}+\nabla_2\cdot\boldsymbol{c}_i\right)h_i^{(0)} \\
&+\varepsilon^2\left(\frac{1}{2}a_s^2(\boldsymbol{n})\partial_{t_1}^2+a_s^2(\boldsymbol{n})(\partial_{t_1}\nabla_1\cdot\boldsymbol{c}_i)+\frac{1}{2}(\nabla_1\cdot\boldsymbol{c}_i)(\nabla_1\cdot\boldsymbol{c}_i)\right)h_i^{(0)} \\
&+\varepsilon^2\left(a_s^2(\boldsymbol{n})\partial_{t_1}+(\nabla_1\cdot\boldsymbol{c}_i)\right)h_i^{(1)}, \qquad \text{(A.12)}
\end{aligned}$$

based on the selected equilibrium distribution of Eq. (A.2):

$$\sum_i h_i^{(0)}=\phi, \qquad \text{(A.13)}$$

$$\sum_i h_i^{(0)}\boldsymbol{c}_i=-\mathscr{N}\frac{W_0^2}{\tau_0}\frac{\delta t}{\delta x}, \qquad \text{(A.14)}$$

$$\sum_i h_i^{(0)}\boldsymbol{c}_i\boldsymbol{c}_i=c_s^2\phi\boldsymbol{I}, \qquad \text{(A.15)}$$

$$\sum_i h_i^{(m)}=0, \qquad for \quad m\neq 0, \qquad \text{(A.16)}$$

$$\sum_i h_i^{(m)} \boldsymbol{c}_i = 0 \qquad for \quad m \neq 0. \tag{A.17}$$

Now, computing the zeroth moment of Eq. (A.11):

$$-\frac{1}{\eta_\phi}\sum_i h_i^{(1)} = a_s^2(\boldsymbol{n})\partial_{t_1}\sum_i h_i^{(0)} + \nabla_1 \cdot \sum_i h_i^{(0)} \boldsymbol{c}_i, \tag{A.18}$$

$$a_s^2(\boldsymbol{n})\partial_{t_1}\phi = \nabla_1 \cdot \left(\mathscr{N}\frac{W_0^2}{\tau_0}\frac{\delta t}{\delta x} \right), \tag{A.19}$$

Then, we compute the moment of first-order for Eq. (A.11).

$$-\frac{1}{\eta_\phi}\sum_i h_i^{(1)} \boldsymbol{c}_i = \left(a_s^2(\boldsymbol{n})\partial_{t_1} + \nabla_1 \cdot \boldsymbol{c}_i\right)\sum_i h_i^{(0)} \boldsymbol{c}_i, \tag{A.20}$$

Then, we compute the zeroth moment of Eq. (A.12).

$$\begin{aligned} -\frac{1}{\eta_\phi}\sum_i h_i^{(2)} \quad = \quad & a_s^2(\boldsymbol{n})\partial_{t_2}\sum_i h_i^{(0)} + \nabla_2 \cdot \sum_i h_i^{(0)} \boldsymbol{c}_i \\ & + a_s^2(\boldsymbol{n})\partial_{t_1}\sum_i h_i^{(1)} + \nabla_1 \cdot \sum_i h_i^{(1)} \boldsymbol{c}_i \\ & + \frac{1}{2}a_s^2(\boldsymbol{n})\partial_{t_1}^2\sum_i h_i^{(0)} + \frac{1}{2}a_s^2(\boldsymbol{n})\partial_{t_1}\nabla_1 \cdot \sum_i h_i^{(0)} \boldsymbol{c}_i \\ & + \frac{1}{2}a_s^2(\boldsymbol{n})\partial_{t_1}\nabla_1 \cdot \sum_i h_i^{(0)} \boldsymbol{c}_i + \frac{1}{2}(\nabla_1 \cdot \boldsymbol{c}_i)(\nabla_1 \cdot \boldsymbol{c}_i)\sum_i h_i^{(0)}, \end{aligned} \tag{A.21}$$

By using Eq. (A.20), the last term on the RHS of Eq. (A.21) is calculated to be:

$$\begin{aligned} \frac{1}{2}a_s^2(\boldsymbol{n})\partial_{t_1}\nabla_1 \cdot \sum_i h_i^{(0)} \boldsymbol{c}_i + \frac{1}{2}(\nabla_1 \cdot \boldsymbol{c}_i)(\nabla_1 \cdot \boldsymbol{c}_i)\sum_i h_i^{(0)} \quad &= \\ \frac{1}{2}\nabla_1\left(a_s^2(\boldsymbol{n})\partial_{t_1} + \nabla_1 \cdot \boldsymbol{c}_i\right)\sum_i h_i^{(0)} \boldsymbol{c}_i \quad &= \\ -\frac{1}{2\eta_\phi}\nabla_1\sum_i h_i^{(1)} \boldsymbol{c}_i & \end{aligned} \tag{A.22}$$

Based on Eq. (A.16) and (A.17), the first term on the LHS of Eq. (A.21) is calculated,

$$-\frac{1}{\eta_\phi}\sum_i h_i^{(2)} = 0, \tag{A.23}$$

The third term on the RHS of Eq. (A.21) is assumed negligible because it can be removed by modifying the collision stage (see BGK-collision model [46]).

Then Eq. (A.21) is simplified as:

$$\begin{aligned} 0 &= a_s^2(\boldsymbol{n})\partial_{t_2}\sum_i h_i^{(0)} + \nabla_2\cdot\sum_i h_i^{(0)}\boldsymbol{c}_i \\ &\quad + a_s^2(\boldsymbol{n})\partial_{t_1}\sum_i h_i^{(1)} + \nabla_1\cdot\sum_i h_i^{(1)}\boldsymbol{c}_i \\ &\quad + 0 + 0 \\ &\quad - \frac{1}{2\eta_\phi}\nabla_1\sum_i h_i^{(1)}\boldsymbol{c}_i, \end{aligned} \tag{A.24}$$

$$\begin{aligned} 0 &= a_s^2(\boldsymbol{n})\partial_{t_2}\sum_i h_i^{(0)} + \nabla_2\cdot\sum_i h_i^{(0)}\boldsymbol{c}_i \\ &\quad + a_s^2(\boldsymbol{n})\partial_{t_1}\sum_i h_i^{(1)} \\ &\quad + \left(1 - \frac{1}{2\eta_\phi}\right)\nabla_1\sum_i h_i^{(1)}\boldsymbol{c}_i. \end{aligned} \tag{A.25}$$

Based on Eq. (A.16) and (A.20), the second term on the RHS of Eq. (A.21) is calculated, leading to:

$$a_s^2(\boldsymbol{n})\partial_{t_1}\sum_i h_i^{(1)} = 0, \tag{A.26}$$

$$a_s^2(\boldsymbol{n})\partial_{t_2}\sum_i h_i^{(0)} + \nabla_2\cdot\sum_i h_i^{(0)}\boldsymbol{c}_i = \left(\eta_\phi - \frac{1}{2}\right)\nabla_1\nabla_1\cdot\sum_i h_i^{(0)}\boldsymbol{c}_i\boldsymbol{c}_i, \tag{A.27}$$

Using Eq. (A.15), (A.13) and (A.14), Eq. (A.27) is simplified as:

$$a_s^2(\boldsymbol{n})\partial_{t_2}\phi - \nabla_2\cdot\left(\mathcal{N}\frac{W_0^2}{\tau_0}\frac{\delta t}{\delta x}\right) = c_s^2\left(\eta_\phi - \frac{1}{2}\right)\nabla_1\cdot\nabla_1\phi, \tag{A.28}$$

In the final step, here three parts of the equation are summed up:

- $\varepsilon^0 \times \sum_i \omega_i Q_\phi \delta t/\tau_0$.
- $\varepsilon^1 \times$ Eq. (A.19).
- $\varepsilon^2 \times$ Eq. (A.28).

In this moment, we recover:

$$a_s^2(\boldsymbol{n})\partial_t\phi - \nabla\cdot\left(\mathscr{N}\frac{W_0^2}{\tau_0}\frac{\delta t}{\delta x}\right) = c_s^2\left(\eta_\phi - \frac{1}{2}\right)\nabla^2\phi + Q_\phi(\boldsymbol{x},t)\frac{\delta t}{\tau_0}, \tag{A.29}$$

Combining the above equation with Eq. 2.16 in Sec. 2.3, the relaxation coefficient is derived to be:

$$\eta_\phi = \frac{1}{c_s^2}\frac{W_0^2}{\tau_0}\frac{\delta t}{\delta x^2}a_s^2(\mathbf{n}) + \frac{1}{2}. \tag{A.30}$$

Appendix B

List of Relevant Publications

[1] **Q. Tan**, S.A. Hosseini, A. Seidel-Morgenstern, D. Thévenin, and H. Lorenz. Thermal effects connected to crystallization dynamics: a lattice Boltzmann study. *International Journal of Multiphase Flow*, 171:104669 (2024).

[2] **Q. Tan**, S.A. Hosseini, A. Seidel-Morgenstern, D. Thévenin, and H. Lorenz. Mandelic acid single-crystal growth: Experiments vs numerical simulations. *Communications in Computational Physics*, 33, 77-100 (2023).

[3] **Q. Tan**, S.A. Hosseini, A. Seidel-Morgenstern, D. Thévenin, and H. Lorenz. Modeling ice crystal growth using the lattice Boltzmann method. *Physics of Fluids*, 34(1):013311 (2022).